Pulsed-DC sputtered TIC/DLC nanocomposite coatings

Shaha, Kalpak Prakash

RIJKSUNIVERSITEIT GRONINGEN

PULSED-DC SPUTTERED TiC/DLC NANOCOMPOSITE COATINGS

GROWTH, MICROSTRUCTURE AND PERFORMANCE

Proefschrift

ter verkrijging van het doctoraat in de
Wiskunde en Natuurwetenschappen
aan de Rijksuniversiteit Groningen
op gezag van de
Rector Magnificus, dr. F. Zwarts,
in het openbaar te verdedigen op
vrijdag 21 januari 2011
om 14.45 uur

door

Kalpak Prakash Shaha

geboren op 7 juli 1980
te Kurduwadi, India

Promotor:	Prof. dr. J. Th. M. de Hosson
Copromotor:	Dr. Y.T. Pei

Beoordelingscommissie:	Prof. dr. A. Cavaleiro
	Prof. dr. P. Rudolf
	Prof. dr. H. A. De Raedt

PULSED-DC SPUTTERED TiC/DLC NANOCOMPOSITE COATINGS
GROWTH, MICROSTRUCTURE AND PERFORMANCE

Kalpak Prakash Shaha

Dedicated to my Parents

ISBN (book): 978-90-77172-68-1
ISBN (digital): 978-90-77172-69-8
Zernike Institue PhD thesis series 2011-04
ISSN 1570-1530

Print: Groningen University Press

Cover: Dynamic growth behavior of 100 and 350 kHz p-DC sputtered TiC/a-C nanocomposite coatings.

The work described in this thesis was carried out as part of the innovation program of the Materials innovation institute (M2i) (formerly, the Netherlands Institute for Metals Research) on *Design of microstructure for optimum performance of DLC based nanocomposite coatings* under the project number MC7.06246.

CONTENTS

Chapter 1
INTRODUCTION

1.1 Introduction

A large variety of structural and functional properties can be optimized separately for the bulk material and the surface by applying an appropriate coating. Therefore, coated parts usually show a superior performance compared to uncoated work pieces. In the second half of the 20th century, surface coatings have emerged as an important industrial branch. In the beginning, coatings have been mainly deposited electrochemically. However, coatings exceeding the hardness of hard chrome (HV about 1000) like transition metal nitrides and carbides cannot be deposited from solution.[1] In the late 1960s, TiC coatings deposited by CVD (chemical vapor deposition) on hard metal cutting tools have been introduced to the market. The beginning of the eighties saw the first PVD (physical vapor deposition) hard coatings appearing on the market. The ever-expanding need for superior coatings to withstand various operating conditions, to have low friction, to last longer is the driving force for further development of new hard coatings. One of the areas of applications for new hard coatings is the use of coated tools for dry machining. Moreover, new coatings have to show improved wear resistance to extend their lifetime. Coatings with increased hardness are expected to fulfill this demand. High load bearing and rolling applications do not necessarily need extremely hard surfaces, but toughness and low friction are key requirements, which may be matched by nanocomposites or multilayers with lubricating solid phases. A composite coating usually consists of two or more phases combined either as different layers (multilayer) or as a homogeneous isotropic mixture of different phases (multiphase). The aim of a multicomponent coating is to combine desired properties from different components as well as the creation of new properties generated by the combination of suitable materials.

In many tribological applications adequate liquids are used as lubricants. However, in some applications, such as food processing, chemical pumps, biological applications, space technology, hard disks, etc. the use of liquid lubricants is not possible. In these cases self-lubricating coatings such as diamond-like-carbon (DLC) coatings are used. A tribological system is usually described by the external parameters such as contact load,

apparent macroscopic contact area, friction partners, surface textures, lubricant used and the environmental parameters. The coefficient of friction (CoF) and the wear are the main parameters used to describe the performance of a tribological system. Whereas from the CoF the energy consumption of the movement of the two counter bodies can be obtained, the wear describes the lifetime of the materials and the amount of wear products produced.

Amorphous DLC consists of strongly cross-linked carbon atoms with mainly sp^2 (graphitic-like) and sp^3 (diamond-like) bonds.[2] In the sp^3 configurations, as in diamond, a carbon atom's four valance electrons are each assigned to a tetrahedrally directed sp^3 orbital, which makes a strong σ bond to an adjacent atom. In the three-fold coordinated sp^2 configuration as in graphite, three of the four valence electrons enter trigonally directed sp^2 orbitals, which form σ bonds in a plane. The fourth electron of the sp^2 atom lies in a π orbital, which lies normal to the σ bonding plane. This π orbital forms a weaker π bond with a π orbital on one or more neighboring atoms. The DLC can be roughly divided in amorphous carbon (a-C) and amorphous hydrocarbon (a-C:H). Basically, a-C:H is an amorphous network composed of carbon and hydrogen. The coating structure is metastable as all methods for deposition are non-equilibrium processes based on thermal quenching of energetic ions impinging on a cold surface.[2] The properties of these coatings depend strongly on the sp^3/ sp^2 ratio, which in turn, depend on the deposition process and its parameters. The most prominent advantages of DLC coatings are their high hardness, their low CoF and their low wear rates. Under tribological conditions, usually the softer of the two materials will be worn. In the case of DLC, a different behavior is often observed. Wear products from the DLC coatings, which have a graphitic nature,[3,4] are transferred to the partner surface forming a so-called transfer film on the partner surface. The DLC then slides on this transfer film that protects the softer partner surface from wear and the harder DLC coated surface wears off at an extremely low rate. The transfer film is believed to be formed by a friction-induced phase transformation of surface layer of DLC[5], and is mainly composed of amorphous graphite-like carbon that isolates the counterface material. As a result, sliding occurs mainly between the transfer film and the DLC coating, yielding low friction.[6] The transfer film formation is affected by the environment, contact pressure and sliding velocity.[7-,9] DLC has been studied extensively as a tribological coating as described in the review articles by Grill,[23-25] Donnet,[10] Gangopadhyay[11] and Erdemir and Donnet.[12]

Because of their increasing popularity and diverse potential applications, DLC coatings have gone through numerous modifications in their microstructure and chemistry during the past decade. Using advanced deposition techniques, researchers have developed nanocomposite or alloyed DLC coatings to provide much improved physical, mechanical and tribological properties. In particular, doping DLC with certain

metals, metalloids and gaseous species (such as Ti, B, S, Si, Cr, F, W and N) has become popular for various applications.[12] Introducing nanocrystalline ceramic particles into an amorphous matrix generate a high density of interphase interfaces that assist in crack deflection and termination of crack growth.[13] DLC based nanocomposites incorporating nanosized particles, like carbides, nitrides or diamond reinforcements are expected to further improve the structural and functional properties of pure amorphous DLC materials[14-17.] The addition of metallic elements such as Ti, W or non-metallic elements such as N and Si are observed to decrease the compressive stresses of the coatings, improving their adhesion to the substrate. The tribological behavior of DLC coating can additionally be influenced by alloying DLC with different elements.

Various deposition techniques such as chemical vapor deposition[18], DC reactive magnetron sputtering[19], cathodic arc deposition[20,21] and pulsed laser deposition[22] have been employed for the synthesis of TiC/a-C or TiC/a-C:H coatings. The deposition method to grow these coatings and their properties are described in the review articles by Robertson[2] and Grill.[23-25]. Pulsed DC (p-DC) magnetron sputtering has become a major technique for deposition of advanced coatings during the last decade.[26-28] It was originally developed for the reactive deposition of insulating coatings to suppress arc events at the target and to stabilize the process. In addition, it has been observed that pulsing magnetrons influences the plasma density and electron temperatures in the plasma, which often result in improved coating microstructure and properties[29-32]. The crucial parameters determining the intensity of ion impingement are the energy distribution of the impinging ions and the flux ratio of impinging ions. It has been observed that pulsing magnetrons in the mid frequency regime (up to 350 kHz) leads to a much extended energy distribution of impinging ions and higher ion current density towards the substrate.[33,34] As a result, dense and well-structured coatings can be grown in pulsed mode.[35,36] A thorough understanding of the mechanism of plasma controlling and microstructure manipulation with pulsed DC magnetron sputtering is still under development and will definitely promote its strength in the production of advanced coatings.

Recently, it has been reported that the columnar boundaries (CBs) of DLC nanocomposite coatings are a potential source of failure under loading and contact sliding.[37, 38] The CBs are harmful as initiation site of cracks and preferential cracking path, attributed to the fact that the homogeneity of nanocomposite is interrupted by the CBs that are enriched in carbon and voids. The columnar boundaries originate at the deep groove networks formed on the growing interfaces. Also, self-assembling has been realized and utilized in the growth of thin coatings with nanoscale ordered structures, like superlattices or multilayers in metal-metal[39,40] and metal-carbon systems.[41-45] Despite the experimental accomplishments, understanding of the physical mechanism and the driving

force is still rather limited, partially due to the fact that a high spatial resolution examination of the structures were not performed. Also, despite the importance and extensive study on amorphous and nanocomposite carbon systems, several aspects regarding the deformation and fracture behavior at the nanoscale, and the underpinning physical mechanisms are not yet understood. Recently several molecular dynamics (MD) simulations have been reported on the deformation and fracture mechanism of DLC and DLC-based nanocomposite at atomic scale[46-49.] However, direct experimental validations of the theoretical models are not available. High resolution transmission electron microscopy experiences a practical difficulty in the examination of DLC or DLC based nanocomposites due to the amorphous nature of DLC. In crystalline materials, HRTEM makes use of the fact that defects create local discontinuity in the otherwise perfect periodicity of the crystalline structure. Thus, it is the presence of a lattice, which acts as an intrinsic reference, that allows the detailed characterization of various defects like line defects (dislocations), and planar defects (homophase and heterophase interfaces), and to investigate their evolution during or after deformation. However, in pure DLC or a homogeneous DLC-based nanocomposite the amorphousness and homogenous state at various length scales make tracing of defects, and evolution of nanostructure, during and after deformation quite elusive. However, by controlling the distribution of nanocrystallites (NCs), so that they form nanoscale multilayers, the NCs can serve as perfect markers for distinguishing various deformation patterns.

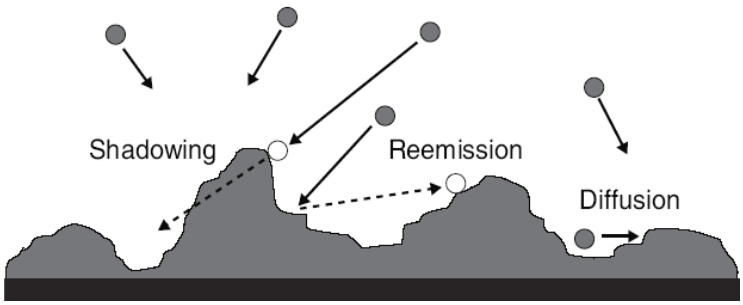

Figure 1.1 Schematic showing growth effects including diffusion, shadowing, reemission that may affect surface morphology during coating growth. The incident particle flux may arrive at the surface with a wide angular distribution depending on the deposition methods and parameters[50].

The growth dynamics of the coatings determines the microstructure (columnar/ column-free) of the coatings. Many growth effects are operating during the growth of a coating and contribute to the surface roughness evolution. A summary of common growth effects is illustrated in Figure 1.1.[50] First, there is always random noise that exists naturally during the deposition process. The origin of randomness is the non uniform nature of incoming flux i.e. atoms reach the surface at random positions, with random time intervals between them. This randomness is generally referred as noise. These random fluctuations, which are inherent in the deposition process, can create growth front roughness. Noise competes with surface smoothing processes, such as surface diffusion,

to form a rough morphology if the experiment is performed at either a sufficiently low temperature and/or at a high growth rate. In addition, growth front roughness can also be enhanced by growth processes such as geometrical shadowing. Shadowing is a result of deposition by a nonnormal incident flux. In many commonly employed deposition techniques such as sputter deposition, atoms do not always approach the surface in parallel; very often they arrive at the surface with a distribution of trajectories. The non-normal incident fluxes can lead to a shadowing effect during growth, as some of the incident atoms will be captured at high points on a corrugated surface at the expense of lower valleys on the surface, resulting in a dramatic enhancement of the growth front roughness. Another important effect to consider is the value of the sticking coefficient. The sticking coefficient is defined as the probability that a particle will stick to the surface when it strikes. In both sputter deposition and chemical vapor deposition, the sticking coefficient may not be equal to unity. A non-unity sticking coefficient would allow the particle to be reemitted from the surface upon impact. The particle may then deposit on the surface at a different location, or it may bounce around the surface more before it settles, which leads to a smoothing effect. Both shadowing and reemission effects are inherently nonlocal because an event that occurs at one place on the surface can affect the surface profile a far distance away.

As with most other materials and coatings, the factors that influence the frictional behavior of DLC coatings are many and may vary from one type of DLC to another. Intrinsically, the degree of sp^2 versus sp^3 bonding as well as the relative amounts of alloying elements in the structure or on the sliding surfaces of DLC coatings can have a strong effect on their friction and wear behaviors. Extrinsically, the frictional behavior of these coatings can be affected by the extent of chemical, physical and mechanical interactions between the rubbing surfaces of DLC coatings and their surroundings. The frictional behavior of DLC based coatings is known to be affected by the humidity, load and sliding velocity.[51,52] Rough surfaces can certainly cause high friction and severe wear losses in most sliding contacts. Specifically, if the sliding surfaces of DLC are very rough, a high level of mechanical interlocking can take place between surface asperities and lead to high frictional losses.[12] For metals, in most cases, initial surface textures are rapidly destroyed as soon as wear starts. However, under low loading conditions and/or for materials with a high hardness, wear rate is low and thus the initial surface roughness may play an important role in tribology. This is usually the case of hard protective coatings like DLC.[53] In general, it is believed that a high surface roughness yields major frictional and wear losses mainly during the running-in period.[12] However, the surface roughness may also influence the overall frictional behavior of these coatings. Moreover, the hardness of the mating materials also influences the tribological properties of DLC coatings.[54] As a consequence, it is important to understand the influence of roughness on

the formation of the transfer film and CoF of these coatings sliding against different counterface materials in order to underpin their tribological properties. Apart from the adverse effects of surface roughness on friction and wear, the extent of chemical and/or adhesive interactions between sliding DLC surfaces may also strongly influence their friction. In these coatings, the adhesive interactions can primarily result from several types of bonding. Among others, covalent bond interactions between unoccupied or dangling σ-bonds of sliding carbon coating interfaces can account for a significant source of adhesion. Covalent bonding is the strongest type in carbon-based materials, and if it is not taken care of then very strong adhesion and hence friction may result between such sliding surfaces. It is known that hydrogen has a strong chemical affinity towards carbon; it bonds strongly to some of the carbon atoms and thus effectively passivates their unoccupied or free σ-bonds. Once passivated, such carbon atoms become chemically inert and cause very little adhesive interactions during sliding and lead to low friction.[12]

1.2 Scope of the thesis

This research was carried out under the project number MC7.06246 in the framework of the research programme of the Materials innovation institute (M2i), Delft, the Netherlands. With the spirit of teamwork, I have worked in close cooperation with Changqiang Chen, Anatoly Turkin, Diego Martinez-Martinez, and my supervisors Yutao Pei and Jeff De Hosson to get the results presented in this thesis. In chapter 2, the deposition and characterization methodologies used for TiC/a-C and TiC/a-C:H nanocomposite coatings studied in this work are described. Chapter 3 is based on [55-61] and concentrates on understanding the growth dynamics of p-DC sputtered TiC/a-C nanocomposite coatings at various pulse frequencies. From detailed analyses of surface morphology and growth conditions, it is concluded that a transition in growth mechanisms occurs, i.e. a mechanism dominated by geometric shadowing at lower pulse frequency evolving to a surface diffusion mechanism driven by impact-induced atomistic downhill flow process by Ar^+ ions at higher pulse frequency which leads to transition from a strong columnar to a columnar-free microstructure. The models describing surface roughness evolution are briefly discussed and it was found that the model is in good agreement with atomic force microscopy measurements of roughness evolution. Chapter 4 is based on [62,63] and focuses on the microstructure and deformation behavior of TiC/a-C nanocomposite coatings deposited by pulse DC magnetron sputtering. The evolution in microstructure from homogeneous to multilayered structure with increasing pulse frequency was observed where the modulation of multilayer was controlled by the self-organization of nanocrystallites due to ion impingement. It is shown that by controlling the distribution of nanocrystallites forming nanoscale multilayers, the system can be used as a "microstructural ruler" that enables distinguishing various deformation patterns

which can be hardly detected otherwise in a homogenous structure. Chapter 5 is based on [64,65,66] and deals with the tribological performance of TiC/a-C and TiC/a-C:H nanocomposite coatings. The effect of roughness of TiC/a-C coatings on tribological behavior while sliding against different counterface materials having different hardness is described. Detailed analyses of the transfer film, sliding surfaces of the ball counterparts, and wear surfaces of the coatings are presented. Furthermore, in order to obtain ultra-low friction, mechanical, structural, chemical bonding (sp^3/sp^2) and tribological properties of TiC/a-C:H coatings are studied as a function of substrate bias voltage, Ti-target current, C_2H_2 flow rate and pulse frequency. Dense, column-free, smooth and ultra-low friction TiC/a-C:H coatings are discussed.

References

1 R. Hauert and J. Patscheider, Adv. Engg. Mater. 2 (2000) 247
2 J. Robertson, Mat. Sci. Eng. R37 (2002) 129.
3 A. Erdemir, C. Bindal, G.R. Fenske, C. Zuiker, P. Wilbur Surf Coat Technol 86 (1996) 692.
4 A.A. Voevodin, A.W. Phelps, J.S. Zabinski, M.S. Donley, Diamond Relat. Mater. 5 (1996) 1264.
5. A.A. Voevodin, A.W. Phelps, J.S. Zabinski, M.S. Donley, Diamond Relat. Mater. 5 (1996) 1264.
6. A.Erdemir, C. Bindal, G.R. Fenske, C. Zuiker, P. Wilbur, Surf. Coat. Tech. 86 (1996) 692.
7. Y.T. Pei, D. Galvan, J.Th.M. De Hosson, Acta Mater., 53 (2005) 4505
8. Y.T. Pei, P. Huizenga, D. Galvan, J.Th.M. De Hosson, J. Appl. Phys. 100 (2006) 114309
9. A. Grill, Surf. Coat. Tech. 94 (1997) 507.
10 C. Donnet. Surf Coat Technol 100 (1998) 180.
11 A. Gangopadhyay Tribol Lett 5 (1998) 25.
12 A. Erdemir, C. Donnet, J. Phys. D: Appl. Phys. 39 (2006) R311.
13 S. Veprek. J Vac Sci Technol A 17 (1999) 2401.
14 Y.T. Pei, D. Galvan, and J.T.M. De Hosson, Acta Mater. 53 (2005) 4505.
15 A. Cavaleiro and J.T.M De Hosson, Nanostructured Coatings. New York: Springer-Verlag; (2006).
16 A.A. Voevodin and J.S. Zabinski, Thin Solid Films 370 (2000) 223.
17 S. Veprek and S. Reiprich. Thin Solid Films 268 (1995) 64.
18 H. Liepack, K. Bartsch, B. Arnold, H.-D. Bauer, X. Liu, M. Knupfer, A. Leonhardt, Diamond Relat. Mater. 13 (2004) 106.
19 U. Jansson, E. Lewin, M. Rasander, O. Eriksson, B. Andre, U. Wiklund Surf. Coat. Technol. 2010 doi:10.1016/j.surfcoat.2010.06.017.
20 B. Yang, Z.H. Huang, H.T. Gao, X.J. Fan, D.J. Fu, Surf. Coat. Technol. 201 (2007) 6808.
21 Y. Wang, X. Zhang, X. Wu, H. Zhang, X. Zhang, Appl. Surf. Sci. 254 (2008) 5085.
22 A.A. Voevodin, J.S. Zabinski, J. Mater. Sci. 33 (1998) 319.
23 A. Grill Surf Coat Technol 94 (1997) 507.
24 A. Grill IBM J Res Develop 43 (1999)147.
25 A. Grill Diamond Relat Mater 8 (1999) 428.
26. S. Schiller , K. Goedicke, J. Reschke, V. Kirchhoff, S. Schneider, F. Milde, Surf. Coat. Technol. 61 (1993) 331.
27. P.J. Kelly, R.D. Arnell, Vacuum 56 (2000) 159.
28. R.D. Arnell, P.J. Kelly, J.W. Bradley, Surf. Coat. Technol. 188 (2004) 158.
29 Y.T. Pei, C.Q. Chen, K.P. Shaha, J.Th.M. De Hosson, J.W. Bradley, S.A. Voronin, and M. Cada, Acta. Mater. 56 (2008) 696.
30 P. J. Kelly, C. F. Beevers, P. S. Henderson, R. D. Arnell, J. W.Bradley and H. Backer: Surf. Coat. Technol., 174–175 (2003) 795.
31 C. Muratore, J. J. Moore and J. A. Rees: Surf. Coat. Technol.163–164 (2003) 12.
32 J.W. Bradley, H. Backer, P.J. Kelly, R.D. Arnell, Surf. Coat. Technol. 135 (2001) 221.

33. J.W. Bradley, H. Bäcker, Y. Aranda-Gonzalvo, P.J. Kelly, R.D. Arnell, Plasma Source Sci. Technol. 11 (2002) 165.
34. H. Bartzsch, P. Frach, K. Goedicke. Surf. Coat. Technol. 132 (2000) 244.
35. P.J. Kelly, R.D. Arnell, J. Vac. Sci. Technol. A17 (1999) 945.
36. M. Audronis, P.J. Kelly, A. Leyland, A. Mattews. Thin Solid Films 515 (2006) 1511
37. Y.T. Pei, D. Galvan, J.Th.M. De Hosson. Acta. Mater. 53 (2005) 4505.
38. D. Galvan, Y.T. Pei, J.Th.M. De Hosson. Surf. Coat. Technol. 200 (2006) 6718.
39. I. Daruka and J. Tersoff, Phys. Rev. Lett. 95 (2005) 076102.
40. J. H. He, C. A. Carosella, G. K. Hubler, S.B. Qadri, and J. A. Sprague, Phys. Rev. Lett. 96 (2006) 056105.
41. W. Y. Wu and Y. M. Ting, Chem. Phys. Lett. 388 (2004) 312.
42. I. Gerhards, H. Stillrich, C. Ronning, H. Hofsäss, and M. Seibt, Phys. Rev. B. 70 (2004) 245418.
43. C. Corbella, B. Echebarria, L. Ramírez-Piscina, E. Pascual, J. L. Andújar, and E. Bertran, Appl. Phys. Lett. 87 (2005) 213117.
44. P. E. Hovsepian, Y. N. Kok, A. P. Ehiasarian, R. Haasch, J. G. Wen, and I. Petrov, Surf. Coat. Tech. 200 (2005) 1572.
45. G. Abrasonis, G. J. Kovács, L. Ryves, M. Krause, A. Mücklich, F. Munnik, T. W. H. Oates, M. M. M. Bilek, and W. Möller, J. Appl. Phys. 105 (2009) 083518.
46 M.G. Fyta, I.N. Remediakis, P.C. Kelires, and D.A. Papaconstantopoulos. Phys. Rev. Lett. 96 (2006) 185503.
47 S. Namilae, B. Radhakrishnan, and G.B. Sarma, Comp. Sci. Tech. 67 (2007) 1302.
48 I.N. Remediakis, M.G. Fyta, C. Mathioudakis, G. Kopidakis, and P.C. Kelires. Diamond Relat. Mater. 16 (2007) 1835.
49 Q. Lu, N. Marks, G.C. Schatz, and T. Belytschkol Phys. Rev. B 77 (2008) 014109.
50 M. Pelliccione, T.M.Lu, Evolution of thin film morphology: Modeling and simulation, Springer, 2008.
51 A. Grill, Surf. Coat. Tech. 94 (1997) 507.
52 J.Th.M. De Hosson, Y.T. Pei, C.Q. Chen, JOM 59-7 (2007) 45.
53. J. Jiang, R.D. Arnell, Wear 239 (2000) 1.
54. H. Liu, A. Tanaka and T. Kumagai, Thin Solid Films 352 (1999) 145.
55 K.P. Shaha, Y.T. Pei, C.Q. Chen, J.Th.M. De Hosson Thin Solid films (2010) doi:10.1016/j.tsf.2010.08.094
56 K.P. Shaha, Y.T. Pei, C.Q. Chen, J.Th.M. De Hosson. *Mater. Technol.* (2010) accepted.
57 K.P. Shaha, Y.T. Pei, C.Q. Chen, A.A. Turkin, D.I. Vainshtein, J.Th.M. De Hosson. Appl. Phys. Lett., 95 (2009) 223102.
58 Y.T. Pei, K.P. Shaha, C.Q. Chen, R. van der Hulst, A.A. Turkin, D.I. Vainshtein, J.Th.M. De Hosson. Acta Mater., 57 (2009) 5156.
59 Y.T. Pei, A.A. Turkin, C.Q. Chen, K.P. Shaha, D.I. Vainshtein, J.Th.M. De Hosson. Appl. Phys. Lett., 96 (2010) 151910.
60 A.A. Turkin, Y.T. Pei, K.P. Shaha, C.Q. Chen, D.I. Vainshtein, J.Th.M. De Hosson. J. Appl. Phys., 105 (2009) 013523.
61 A.A. Turkin, Y.T. Pei, K.P. Shaha, C.Q. Chen, D.I. Vainshtein, J.Th.M. De Hosson.. J. Appl. Phys., 108 (2010) 1.
62 C.Q. Chen, Y.T. Pei, K.P. Shaha, J.Th.M. De Hosson. Appl. Phys. Let., 96 (2010) 073103.
63 C.Q. Chen, Y.T. Pei, K.P. Shaha, J.Th.M. De Hosson J.App. Phys. 105 (2009) 114314
64 K.P. Shaha, Y.T. Pei, D. Martinez-Martinez, J.Th.M. De Hosson Tribol. Lett. (2010) doi:10.1007/s11249-010-9691-4
65 K.P. Shaha, Y.T. Pei, D. Martinez-Martinez, J.Th.M. De Hosson Surf. Coat. Technol. (2010) doi:10.1016/j.surfcoat.2010.10.021.
66 K.P. Shaha, Y.T. Pei, D. Martinez-Martinez, J.C. Sanchez-Lopez, J.Th.M. De Hosson, Surf. Coat. Technol. (2010) doi:10.1016/j.surfcoat.2010.10.020

Chapter 2
DEPOSITION AND CHARACTERIZATION TECHNIQUES

2.1 Introduction

In this chapter, firstly, the PVD setup employed to deposit the nanocomposite coatings is described with a brief introduction to magnetron sputtering. Furthermore the characterization techniques viz. mass energy spectrometry (plasma characterization), Grazing incidence X-ray diffraction (nanostructure characterization), Atomic force microscopy (surface morphological characterization), Tribological testing (frictional and wear behavior), Confocal microscopy (characterization of wear and transfer film) and Raman microscopy (structural characterization) are briefly described. The microstructure of these coatings was scrutinized by high resolution scanning electron microscopy (SEM) and transmission electron microscopy (TEM). For description of SEM and TEM, the reader is referred to the previous PhD theses from our group.

2.2 PVD deposition setup

Physical vapor deposition and plasma enhanced chemical vapor deposition techniques were employed in this study to deposit the coatings. Magnetron sputtering has developed rapidly over the last decade to the point where it has become established as the process of choice for the deposition of a wide range of industrially important coatings.[1,2] The driving force behind this development has been the increasing demand for high-quality functional coatings in many diverse market sectors.

In the basic sputtering process, a target (or cathode) plate is bombarded by energetic ions generated in a glow discharge plasma, situated in front of the target. The bombardment process causes the removal (i.e. sputtering) of target atoms, which may then condense on a substrate as a thin film.[2] Secondary electrons are also emitted from the target surface as a result of the ion bombardment, and these electrons play an important role in maintaining the plasma. Magnetrons make use of the fact that a magnetic field can constrain secondary electron motion to the vicinity of the target.

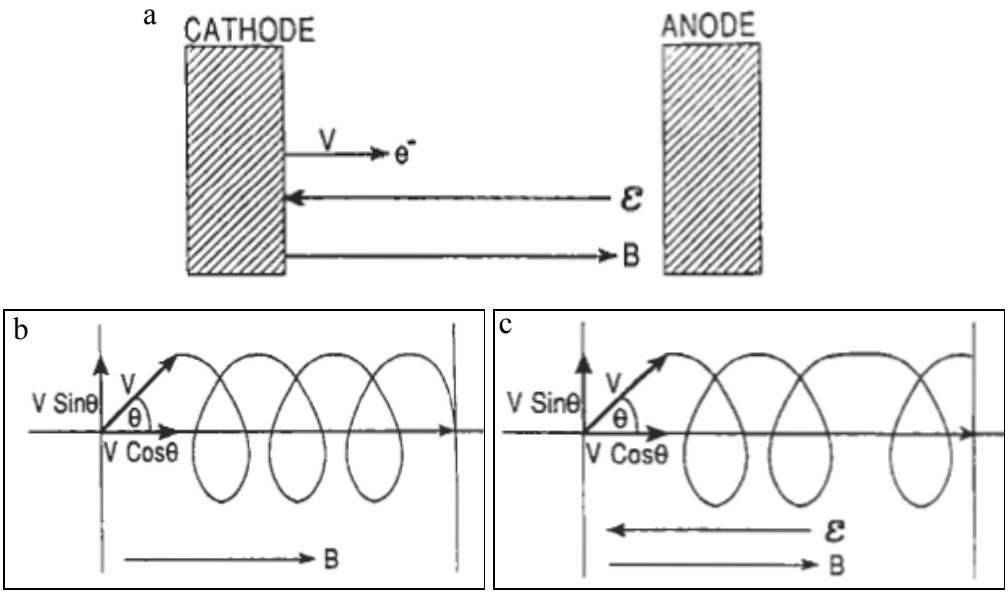

Figure 2.1 Effect of ε and B on electron motion. (a) Linear electron trajectory when ε // B (θ = 0); (b) helical orbit of constant pitch when B ≠ 0, ε = 0,(θ ≠ 0);(c) helical orbit of variable pitch when ε // B (θ ≠ 0)[2]

When a magnetic field of strength B is superimposed on the electric field ε between the target and substrate, electrons within the dual field environment experience the well-known Lorentz force in addition to electric field force[2], i.e.,

$$F = \frac{mdv}{dt} = -q(\varepsilon + v \times B) \qquad (2.1)$$

where q, m and v are the electron charge, mass, and velocity, respectively. In the case where B and ε are parallel as shown in Figure 2.1a. When electrons are emitted exactly normal to the target surface and parallel to both fields, then $v \times B$ vanishes; electrons are only influenced by the ε field, which accelerates them toward the anode. Next consider the case where the ε field is neglected but B is still applied as shown in Figure 2.1b. If an electron is launched from the cathode with velocity v at angle θ with respect to B, it experiences a force $qvBsin\theta$ in a direction perpendicular to B. The electron now orbits in a circular motion with a radius r that is determined by a balance of the centrifugal $(m(v\,sin\theta)^2/r)$ and Lorentz forces involved, i.e., $r=mv\,sin\theta/qB$.[2] The electron motion is helical; in corkscrew fashion and it spirals down the axis of the discharge with constant velocity $v\,cos\theta$. If the magnetic field were not present, such off-axis electrons would tend to migrate out of the discharge and be lost at the walls. The case where electrons are launched at an angle to parallel, uniform ε and B fields is somewhat more complex. Corkscrew motion with constant radius occurs, but because of electron acceleration in the ε field, the pitch of the helix lengthens with time[2] (Figure 2.1c). Time varying ε fields complicate matters further and electron spirals of variable

radius can occur. Clearly, magnetic fields prolong the electron residence time in the plasma and thus enhance the probability of ion collisions. This leads to larger discharge currents and increased sputter deposition rates. Comparable discharges in a simple diode-sputtering configuration operate at higher currents and pressures, therefore, applied magnetic fields have the desirable effect of reducing electron bombardment of substrates and extending the operating vacuum range.

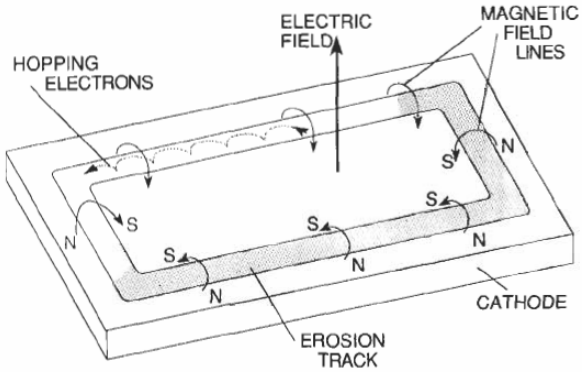

Figure 2.2 Applied fields and electron motion in a planar magnetron.[2]

In magnetrons, electrons ideally do not even reach the anode but are trapped near the target, enhancing the ionizing efficiency there. This is accomplished by employing a magnetic field oriented parallel to the target and perpendicular to the electric field, as shown schematically in Figure 2.2. Practically, this is achieved by placing bar or horseshoe magnets behind the target. Therefore, the magnetic field lines first emanate normal to the target, then bend with a component parallel to the target surface (this is the magnetron component) and finally return, completing the magnetic circuit. Electrons emitted from the cathode are initially accelerated toward the anode, executing a helical motion in the process; but when they encounter the region of the parallel magnetic field, they are bent in an orbit back to the target in very much the same way that electrons are deflected toward the hearth in an e-gun evaporator. By solving the coupled differential equations resulting from the three components of Eq. 2.1, we readily see that the parametric equations of motion are[2]

$$y = \frac{q\varepsilon}{m\omega_c^2}(1 - \cos\omega_c t) \qquad (2.2)$$

$$x = \frac{\varepsilon t}{B}(1 - \frac{\sin\omega_c t}{\omega_c t}) \qquad (2.3)$$

where y and x are the distances above and along the target, and $\omega_c = qB/m$. These equations describe a cycloidal motion that the electrons execute within the cathode dark space where both fields are present. If, however, electrons stray into the negative glow

region where the ε field is small, the electrons describe a circular motion before collisions may drive them back into the dark space or forward toward the anode. By suitable orientation of target magnets, a "race track" can be defined where the electrons hop around at high speed. Target erosion by sputtering occurs within this track because ionization of the working gas is most intense above it.

Magnetron sputtering is presently the most widely commercially practiced sputtering method. The chief reason for its success is the high deposition rates achieved. These are typically an order of magnitude higher than rates attained by conventional sputtering techniques. [1] In an unbalanced magnetron the outer ring of magnets is strengthened relative to the central pole. In this case, not all the field lines are closed between the central and outer poles in the magnetron, but some are directed towards the substrate, and some secondary electrons are able to follow these field lines. Consequently, the plasma is no longer strongly confined to the target region, but is also allowed to flow out towards the substrate.[1] Thus, high ion currents can be extracted from the plasma to the substrate. In a multiple magnetron system, as the one used in this study, the magnetic arrays in adjacent magnetrons can be configured with opposite magnetic polarities. In this case the configuration is described as closed field. In closed field configuration, the field lines are linked between the magnetrons. Losses of the secondary electrons to the chamber walls are low and the substrate lies in a high density plasma region.[1,3]

Figure 2.3 Teer UDP-400/4 deposition system.

In this research, a TEER UDP400/4 sputtering system (Figure 2.3) was used to deposit coatings. The vacuum chamber is made up of stainless steel, and is double-walled to allow water cooling. Its internal diameter and height are 400 mm.

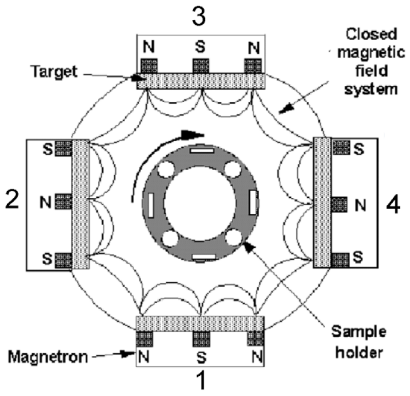

Figure 2.4 Schematic of the deposition setup indicating the configuration of targets. The number of the magnetrons are indicated.

The system consists of four magnetrons, in a closed field unbalanced configuration, coupled to four targets with the geometry shown in Figure 2.4. The size of all the targets was 200×100 mm². The magnetrons 2 and 4 are powered by a Pinnacle Plus 5/5 kW double channel p-DC power supply (Advanced Energy) and the magnetrons 1 and 3 are powered by a Pinnacle 6/6 kW double channel DC power supply. Magnetron 1 and 3 were coupled with Ti and Cr targets, respectively. Magnetron 2 and 4 were coupled with two graphite targets each, for the deposition of TiC/a-C nanocomposite coatings (Ar environment), whereas these magnetrons were coupled to two Ti-targets each for the deposition of TiC/a-C:H nanocomposite coatings (in $Ar+C_2H_2$ environment). All the power units for sputtering were operated in current-control mode. The substrates were biased by a Pinnacle Plus 5 kW single channel p-DC power supply (Advanced Energy). The pumping system consists of a oil-free turbomolecular pump backed by a rotary pump. The base pressure of the chamber before deposition was $3\text{-}4\times10^{-6}$ mbar. The substrates were first ultrasonically cleaned in acetone followed by Ar plasma etching for 15 minutes at p-DC -400 V bias voltage at 250 kHz and 87.5 % duty cycle. The substrate holder was rotated by 3 rpm. No external heating was applied to the substrates.

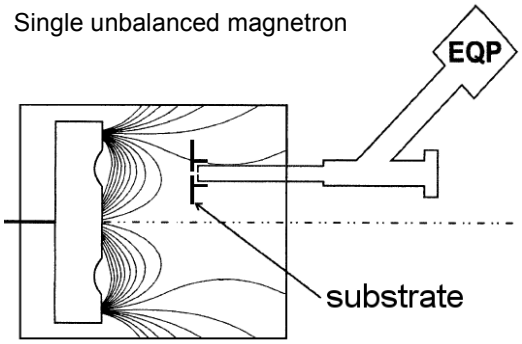

Figure 2.5 Schematic diagram showing the relative positions of the magnetron, mass energy spectrometer.[4]

A Hiden EQP 300 mass and energy analyzer was used to study the Ar^+ ion energy distribution function (IEDF) function at the substrate. The experimental setup includes a single unbalanced magnetron sputtering system, GEN*LAB* (GENCOA Ltd), installed with a ø150 mm circular magnetron, with the mass energy spectrometer attached. Figure 2.5 shows the schematic showing the relative positions of the target and the probe of the mass energy spectrometer. It had a typical unbalanced configuration of adjustable magnetic field strength, which was set to resemble the field strength of the magnetrons installed in the TEER UDP400/4 rig. The single magnetron was powered with a 5kW Pinnacle Plus unit and operated at comparable sputtering parameters used for coating deposition. The extractor head of the EQP300 instrument was pointed to the racetrack of the target and fixed directly behind a metallic substrate at 100 mm distance to the target, which had a large opening hole that was covered with a fine nickel grid and aligned with the entrance orifice (ø100 μm) of the extractor. The instrument is commercially available, and has been described in detail elsewhere.[5] The ion energies were effectively measured with reference to ground potential of the chamber wall. The counts of Ar^+ ions in each energy bin <E, E+*d*E>, where *d*E = 0.1 eV was the energy resolution of the instrument, were accumulated for 10 ms time period and one scan of the whole energy spectra took 20 seconds. Therefore, the ion counts of different energies were a direct measure of the ion flux and it can be confidently compared among the measurements, provided the instrument settings remained unchanged.

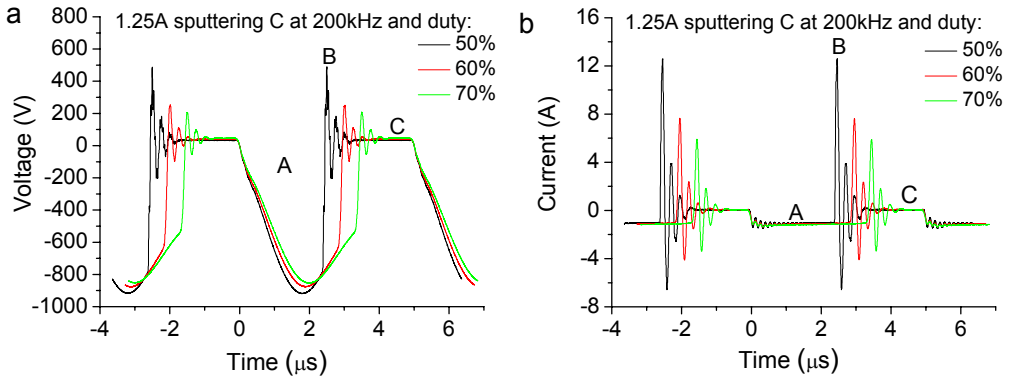

Figure 2.6 Waveforms of 1.25A p-DC sputtering graphite target at 200 kHz and different duty cycles: (a) voltage and (b) current.

The mass energy spectrometry results presented here are based on Ref. 7. Figure 2.6 presents the *p*-DC voltage and current waveforms applied to the graphite target at 1.25A of sputtering current. The voltage waveform of the asymmetric bipolar pulsed DC exhibited three characteristic periods: the pulse on period A of negative voltage, the transition period B and the pulse off or reverse period C (see Figure 2.6a), which are well documented in literature.[6]

The duty cycle of DC pulses was defined as the percentage of the pulse-on period to the whole pulse cycle. The significant features of the asymmetric bipolar *p*-DC power supplies used in this research include the overshoot peak of high positive voltage (around 500 V in this case) in the transition period B and the adjacent oscillating peaks as well as the small positive voltage remaining during the reverse period C. During this transition and onset of the reverse period, correspondingly, the current waveform possessed several current peaks of amplitude strongly depending on the duty cycles used (Figure 2.6b). For instance, the current peaks at 50% duty cycle were of 13 A, 6.5 A, 4 A, 1.5A, etc., and the strongest peak was one order of magnitude as high as the nominal current (1.25 A).

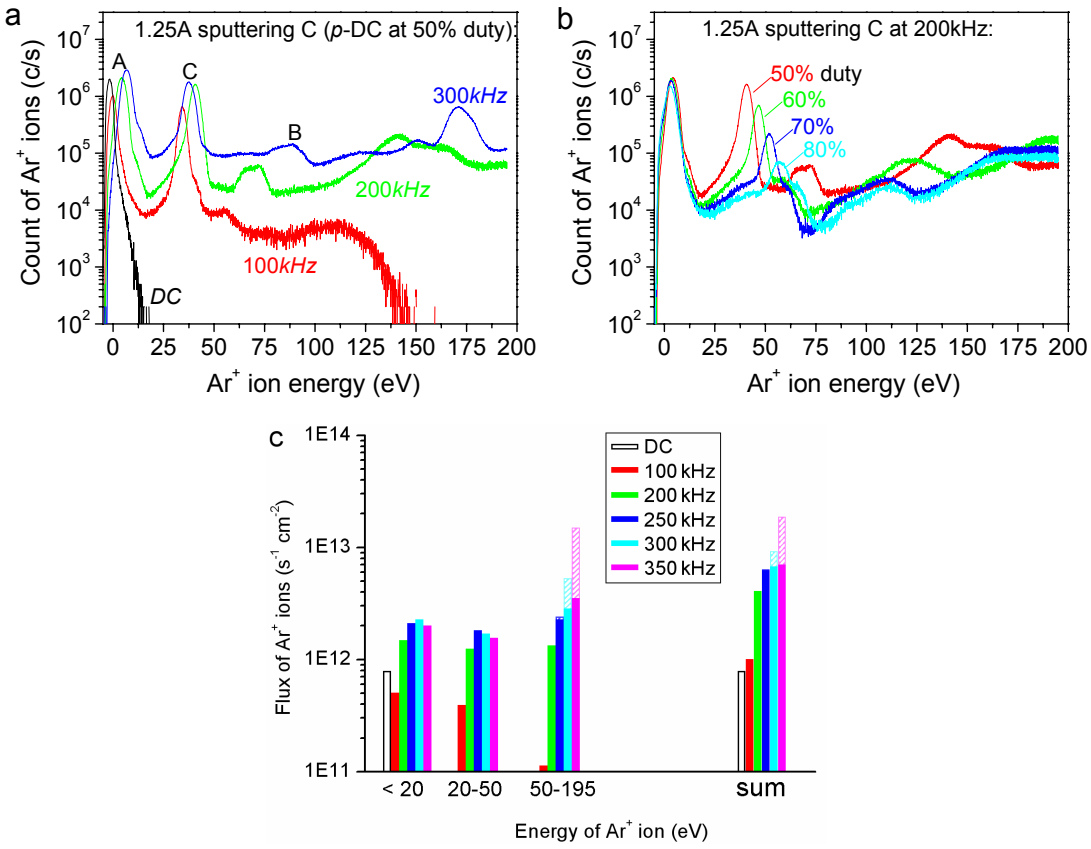

Figure 2.7 Energy distribution of impinging Ar^+ ions incident on the growing coatings during sputtering graphite target with DC or pulsed DC at different frequencies (a) and at 200 kHz of different duty cycles (b); (c) flux of impinging Ar^+ ions in three energy ranges as well as the sum at different p-DC frequencies of 50% duty cycle (substrate grounded). The hatched part of the columns is the missed flux due to the cutoff of the energy spectrometer beyond 195 eV, estimated according to the fraction of the reversing period in a pulse for different frequencies.

The time averaged energy distribution and the flux of the impinging Ar^+ ions during sputtering graphite are shown in Figure 2.7. The IED curves of the impinging Ar^+ ions under *p*-DC magnetron sputtering showed three distinct populations of the ions that reflect the target voltage waveforms. That is to say, impingements of Ar^+ ions of low

energy (< 20 eV, peak A in Figure 2.7a) occurred during the pulse-on period, supported by the fact that DC magnetron sputtering produced only the low energy ions of the same category. The ions of intermediate energy (20-50 eV, peak C in Figure 2.7a) were generated during the reverse period, which was evident because the population of this category ions diminished with decreasing reverse period (i.e. increasing the duty cycle at a chosen *p*-DC frequency), as shown in Figure 2.7b. Those ions of high energy extending over 200 eV were created during the transition period, accelerated by the high potential fall (positive voltage peaks) towards the grounded substrate. Because of the detection limit of the energy spectrometer, the energy distribution function curves at a *p*-DC frequency above 200 kHz were partly cut off beyond 195 eV. As shown in Figure 2.7c, the flux of the total impinging Ar^+ ions at *p*-DC sputtering mode of low frequencies (e.g. 100 kHz) was comparable with that of DC magnetron sputtering. However, the total ion flux dramatically increased with increasing the frequency beyond 100 kHz. The flux of total impinging ions differed by one order of magnitude between DC sputtering and *p*-DC sputtering at high frequencies. It is clear that the energy distribution function of the impinging Ar^+ ions was governed by the sputtering mode: *p*-DC frequency and the duty cycle.

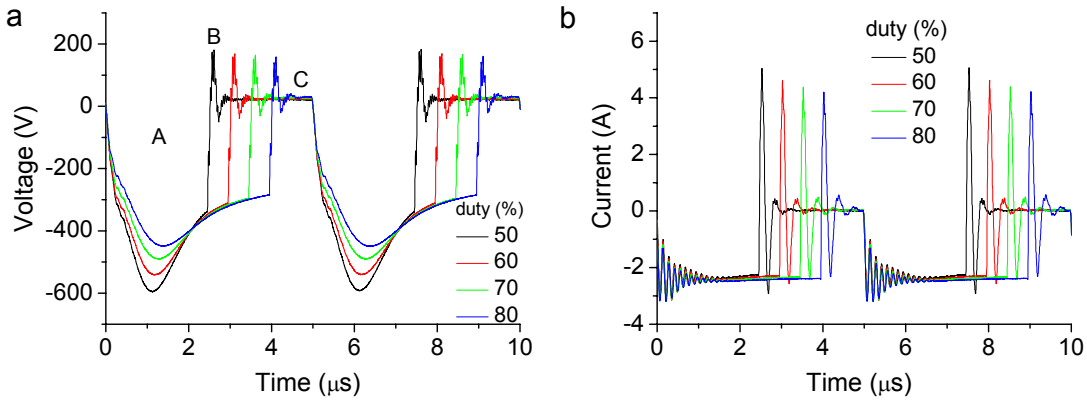

Figure 2.8 Waveforms of 2.5A p-DC sputtering titanium target at 200 kHz and different duty cycles: (a) voltage and (b) current.

In comparison with sputtering of graphite target, the voltage in the pulse on period was lower, with about 500 V in sputtering Ti versus 900 V in sputtering C. Especially, the overshoot peaks of voltage and current measured during sputtering titanium were much lower (see Figure 2.8a), only about one third of the amplitudes of those peaks observed in the former case. As a result, the energy spread of the high energy Ar^+ ions was reduced (Figure 2.9a). This led to a lower ion flux at each *p*-DC frequency (Figure 2.9b), even though the sputtering current of 2.5 A is doubled on Ti target of the same size. Similar results of impinging Ar^+ ion energy distribution as a function of p-DC frequency were observed during sputtering Ti target, as shown in Figure 2.9.

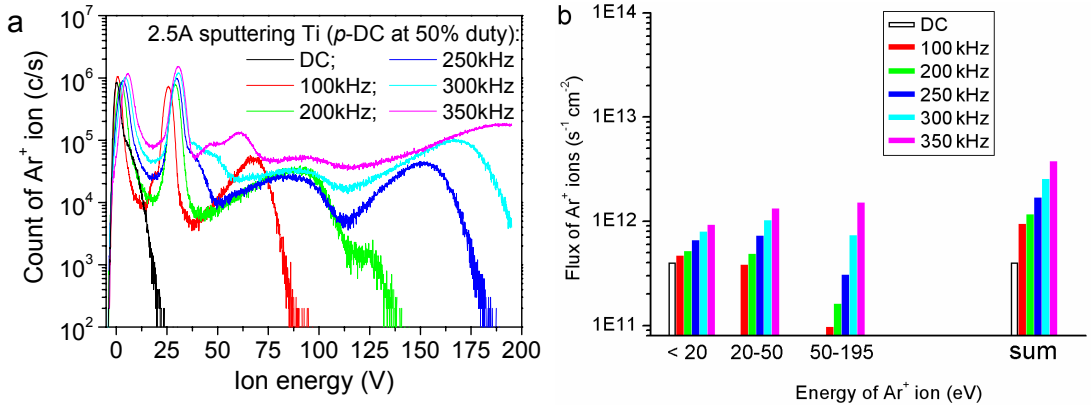

Figure 2.9 (a) Energy distribution of impinging Ar^+ ions incident on the growing coatings during sputtering Ti target with DC or pulsed DC of different frequencies and (b) flux of the Ar+ ions in three energy ranges as well as the sum at different p-DC frequencies (substrate grounded).

In particular, the impinging ions in the intermediate and high energy bands became more and more dominant with increasing *p*-DC frequency, delivering much higher energy for impingement to the growing coatings. To confirm this point, the product of the time-averaged ion count in each energy bin and the energy scale under the IED curves in Figure 2.7a and Figure 2.9a was integrated over the measured energy range and the results are shown as energy flux in Figure 2.10.

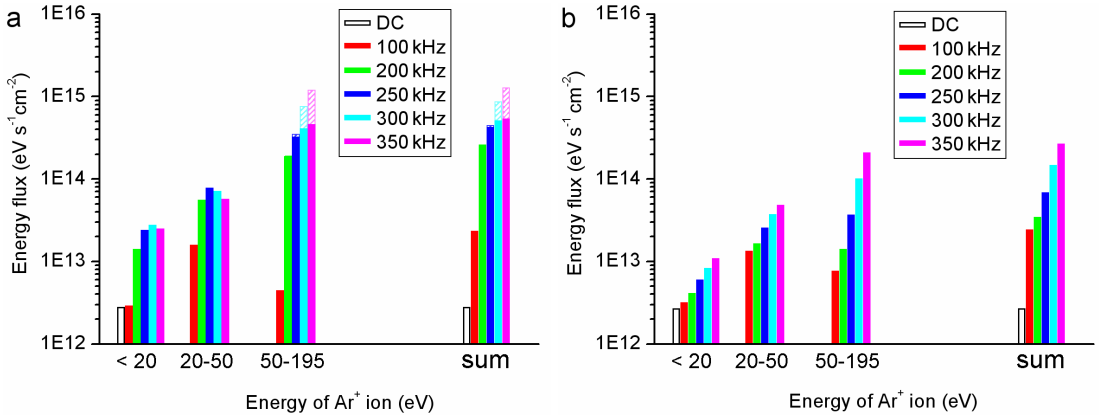

Figure 2.10 Energy flux delivered to the growing interface by impinging Ar^+ ions: (a) during sputtering C with 1.25A current and (b) during sputtering Ti with 2.5A current DC or p-DC at different frequencies. The hatched part of the columns is the missed flux due to cutoff of the high energy ions beyond the limit of the energy spectrometer.

It is clear that the energy flux of impinging Ar^+ ions under high frequencies *p*-DC sputtering was two orders of magnitude larger than that delivered at DC sputtering. Due to different electrical characteristics conductivity and sputtering behavior of different target materials, in particular, *p*-DC sputtering graphite target delivers even higher energy flux of impinging ions than sputtering titanium target (e.g. 1.26×10^{15} versus 2.69×10^{14} $eVs^{-1}cm^{-2}$ at 350 kHz), although the nominal sputtering current was half of the latter case

(1.25 A versus 2.5 A). However, the energy flux dropped significantly at low p-DC frequencies, for instance at 100 kHz or lower. The key parameters of concurrent ion impingement are the flux of the impinging ions and energy delivered. The enhanced total ion flux measured in Figure 2.7c and Figure 2.9b can be ascribed to the higher average plasma density under *p*-DC sputtering. In view of this, *p*-DC discharge is able to transform more electrical energy into the average plasma density and electron temperature than compared to the DC discharge, even if the average power delivered to both the discharges is the same. In other words, *p*-DC discharge more efficiently transfers plasma energy to the growing thin coating. The Ar^+ ion energy distribution spectra clearly demonstrated that the ion counts in the high energy bins were lower than those in the low energy bins. However, due to the wide energy spread, the total flux of the high energy ions delivered in the period B increases with increasing pulse frequency and it becomes comparable to the flux of those low energy ions delivered during the period A and C at high pulse frequencies (see Figure 2.7c and Figure 2.9b).

In the pulsing regime of the asymmetric bipolar pulsed DC power supplies, the duration of the pulse transition period B is a system constant of approximately 200 ns independent of the pulse frequency and duty cycle. As pulse frequency increases, the proportion of the transition period B in a pulse cycle increased and the overshoot voltage increases. Therefore, its contribution to the delivery of impinging Ar^+ ions of high energy must increase as well. Furthermore, cathode current waveforms reveal that the discharge electron current during the cathode overshoot period B noticeably increases with pulse frequency[7], besides the reversal of the flow direction. The lack of bulk electrons during this period causes the plasma sheath adjacent to the grounded substrate/orifice to expand more with increasing pulse frequency. As a result, the volume of ion sheath in the front of the orifice is getting larger with pulse frequency and consequently the number of ions attracted onto the growing coating or into the energy spectrometer during the pulse transition period B increases as shown in Figure 2.7c and Figure 2.9b. These effects result in a much higher total energy flux to the substrate.

In comparison with the high flux of impinging Ar^+ ions, the flux of ions of sputtered material was rather low even under p-DC sputtering.[7] The energy distribution of Ti^+ ion was very similar to the IED curves of Ar^+ ions presented in but the counts were nearly two orders of magnitude lower in all the energy bins. Similarly, the counts of C^+ ions were three orders of magnitude lower than that of the Ar^+ ions for all the p-DC frequencies.

Besides the enhancement of the flux and energy distribution of impinging ions, another significant feature of p-DC magnetron sputtering is the expansion of the plasma.[7] At higher pulse frequency, the plasma covers the entire substrate and also fills in the whole chamber. It is this expanded plasma that keeps the growing coating under intensive

and in particular continuous impingement when passing from one target to another in a closed-field configuration of multi-targets sputtering system. At 350 kHz, the enhanced flux and impinging energy of argon ions to the growing coatings and the grounded walls bring about increased generation of secondary electrons. These electrons are accelerated back to the plasma and gain kinetic energy through the plasma sheath which enables them to excite or ionize atoms and molecules of working gas. As a result of this processes, glow discharge was observed not only between the target and substrate but also in the whole chamber.[7]

Thus, Ar^+ ion energy flux delivered to the substrate strongly depends on the shape and magnitude of the cathode voltage overshoot (pulse transition period B) and also on the material of which the target is made. A difference between magnitudes of ionization potential, sputtering yield and secondary electron emission coefficient of carbon and titanium can affect plasma parameters, cathode voltage and current waveforms. These parameters are then crucial in determining the plasma intensity and ion energy flux onto the growing coating.

2.3 Characterization techniques:

2.3.1 Grazing incidence X ray diffraction:

The principle of this technique is based on the detection of a diffracted beam when the Bragg diffraction condition $2d_{hkl}\sin\theta = n\lambda$ is fulfilled, where d is the space between the planes, θ is the diffraction angle, n is the order of the diffraction peak and λ is the wavelength of the x-rays.

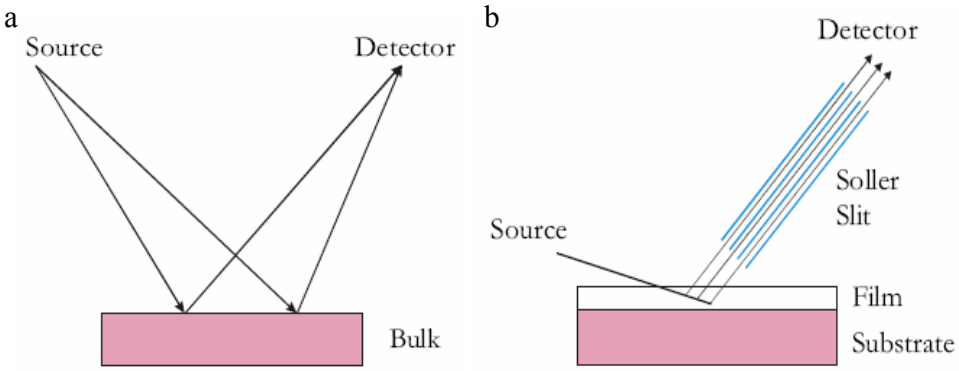

Figure 2.11 Geometries for a) bulk analysis and b) thin coating analysis showing differences in the beam path lengths.

It is sometimes very difficult to analyze thin coatings due to their small diffracting volumes, which result in low diffracted intensities compared to the substrate and background. This combination of low diffracted signal and high background make it very difficult to identify the phases present. Accordingly, special techniques must be used

when analyzing thin coatings. The most common technique for analyzing thin coatings as thin as 100 Å is to use a grazing incidence angle arrangement combined with a parallel beam geometry. By increasing the path length of the incident X-ray beam through the film, the intensity from the film can be increased so that conventional phase identification analysis can be run. Figure 2.11 compares the grazing incidence angle geometry used for thin coating with the more common, *θ/2θ* geometry used for bulk analysis. In the conventional *θ/2θ* geometry, a parafocusing arrangement is used where the X-ray source and the detector slit are at the focal points of the incident and diffracted beams, respectively. For the thin coating arrangement, on the other hand, the incident and diffracted beams are made nearly parallel by means of a narrow slit on the incident beam and a long soller slit on the detector side. In addition, the stationary incident beam makes a very small angle with the sample surface (typically 1° to 3°), which increases the path length of the X-ray beam through the coating. This helps to increase the diffracted intensity, while the same time, reduces the diffracted intensity from the substrate. Overall, there is a dramatic increase in the film signal to the background ratio. Since the path length increases when the grazing incidence angle is used, the diffracting volume increases proportionally. This is the reason for the increased signal strength. During the collection of the diffraction spectrum, only the detector rotates through the angular range, thus keeping the incident angle, the beam path length, and the irradiated area constant. The long soller slit on the receiving side allows only those beams that are nearly parallel to arrive at the detector. This has an added advantage of reducing the sensitivity to sample displacement from the rotation axis.

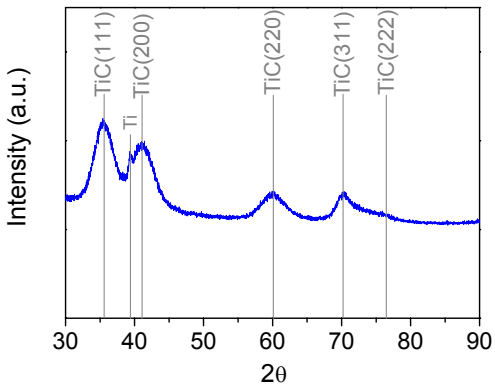

Figure 2.12 Grazing incidence XRD spectra of about 1μm thick TiC/a-C:H nanocomposite cioating deposited on Si with a TiCr interlayer inbetween.

A single circle diffractometer (Bruker D8 ADVANCE) was used with an grazing angle of 1.5°, with a CuKα radiation (λ=1.540 Å) generator operated at 40kV and 40mA. Figure 2.12 is a typical grazing incidence XRD spectra of TiC/a-C:H nanocomposite coating, where the nanometer range size of the diffracting TiC crystals causes broadening of the peaks. The average size (d) of the nanocrystallites can be estimated from the full

width at half maximum (FWHM) of the peaks and its diffraction angle by using Scherrer equation:

$$d = 0.9\frac{\lambda}{\cos\theta \cdot FWHM_{peak}} \qquad (2.4)$$

where the FWHM should be introduced in radians to maintain the unit of λ for d.

2.3.2 AFM

Figure 2.13 Picture of AFM (Veeco NanoScope IIIa and Dimension 3100 AFM).

In this work, the surface morphology of the nanocomposite coatings, and the surface roughness evolution of the coatings with sliding distance were investigated by a Digital Instrument NanoScope IIIa and Dimension 3100 atomic force microscope (Figure 2.13) with a Si tip of nominal 10 nm radius in tapping mode. The atomic force microscope (AFM) was invented by Binning et al. in 1986.[8] The AFM measures the forces acting between a fine tip and a sample. The tip is attached to the free end of a cantilever and is brought very close to a surface. Attractive or repulsive forces resulting from interactions between the tip and the surface will cause a positive or negative bending of the cantilever. The bending is detected by means of a laser beam, which is reflected from the back side of the cantilever. Figure 2.14a shows the basic concept of AFM. The AFM is mainly based on probe, which represents a micromachined cantilever with a sharp tip at one end, which is brought into interaction with the sample surface. Each probe has different specifications and shape. V-shaped cantilevers are the most popular (but also there are rectangular), providing low mechanical resistance to vertical deflection, and high resistance to lateral torsion. Cantilevers typically range from 100 to 200 μm in length, 10 to 40 μm in width, and 0.3 to 2μm in thickness.

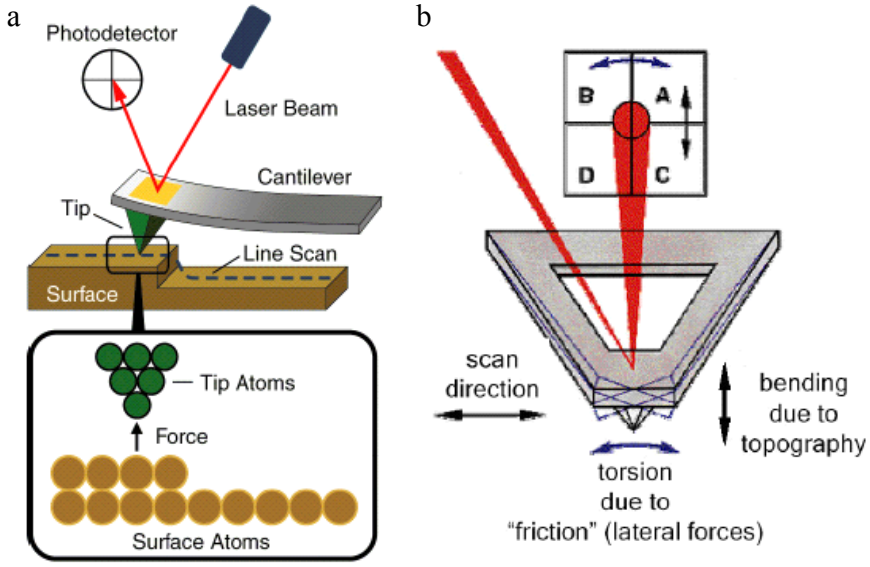

Figure 2.14 (a) Principle of AFM; (b) The beam deflection photodetector consisting of 4 photodiodes.[9]

Integrated cantilevers are usually made from silicon (Si) or silicon nitride (Si_3N_4). They are characterized by their force constant and resonant frequency. An optical detection system and electronics for the management of scanning procedures and data acquisition are necessary. To detect the displacement of the cantilever, a laser is reflected off the back of the cantilever and collected in a photodiode. The diode is divided into four parts, as seen in Figure 2.14b. When the laser is displaced vertically along the positions top (B-A) and bottom (D-C), there exists a bending due to topography, while if this movement is horizontal left (B-D) and right (A-C), it produces a torsion due to "friction" (lateral force). The differential signal between the top two elements and the two bottom elements provides a measure of the vertical deflection of the cantilever. Similarly, the differential signal between the sum of the two left elements and the sum of the two right elements provides a measure of the torsion in the cantilever.

The AFM can be used in different modes of operations. In the so-called contact-AFM mode, the tip makes soft "physical contact" with the surface of the sample. The deflection of the cantilever Δx is proportional to the force acting on the tip, via Hook's law, $F=-k\times\Delta x$, where k is the spring constant of the cantilever. In contact-mode, the tip either scans at a constant small height above the surface or under the conditions of a constant force. In the constant height mode, the height of the tip is fixed, whereas in the constant-force mode the deflection of the cantilever is fixed and the motion of the scanner in z-direction is recorded. By using contact-mode AFM, even "atomic resolution" images are obtained. For contact mode AFM imaging, it is necessary to have a cantilever which is soft enough to be deflected by very small forces and has a high enough resonant frequency to not be susceptible to vibrational instabilities. Silicon Nitride tips are used for

contact mode. In these tips, there are 4 cantilever with different geometries attached to each substrate, resulting in 4 different spring constants. To avoid problems caused by capillary forces which are generated by a liquid contamination layer usually present on surfaces in air, the sample can be studied while immersed in a liquid. This procedure is especially beneficial for biological samples.

In non-Contact Mode, the probe operates in the attractive force region and the tip-sample interaction is minimized. The use of non-contact mode allowed scanning without influencing the shape of the sample by the tip-sample forces. In most cases, the cantilever of choice for this mode is the one having high spring constant of 20-100 N/m so that it does not stick to the sample surface at small amplitudes. The tips mainly used for this mode are silicon probes.

Another mode of operation is Tapping mode (intermittent contact mode). The force measured by AFM can be classified into long-range forces and short range forces. The first class dominates when we scan at large distances from the surface and they can be Van der Waals force, capillary forces (due to the water layer often present in an ambient environment). When the scanning is in contact with the surface the short range forces are very important, in particular the quantum mechanical forces (Pauli Exclusion Principle forces). In tapping mode-AFM the cantilever is oscillating close to its resonance frequency. An electronic feedback loop ensures that the oscillation amplitude remains constant, such that a constant tip-sample interaction is maintained during scanning. Forces that act between the sample and the tip will not only cause a change in the oscillation amplitude, but also change in the resonant frequency and phase of the cantilever. The amplitude is used for the feedback and the vertical adjustments of the piezoscanner are recorded as a height image. Simultaneously, the phase changes are presented in the phase image. The advantages of the tapping mode are the elimination of a large part of permanent shearing forces and the causing of less damage to the sample surface, even with stiffer probes. Different components of the sample which exhibit difference adhesive and mechanical properties will show a phase contrast and therefore even allow a compositional analysis. Silicon probes are used primarily for Tapping Mode applications.

In summary, in these modes we can work in different environments: air, liquid and vacuum. In contact mode the tip touches the sample surface, which leads to a high force and allows manipulation of the sample. The disadvantage is that the AFM tip may be contaminated by the sample. The opposite happens in the noncontact mode, where the tip stays at a distance above the sample. In tapping mode the tip touches the surface periodically therefore manipulation of the sample, as well as contamination of the tip is possible.

2.3.3 Tribological testing:

Friction is the dissipation of energy between sliding bodies. The coefficient of friction is calculated from the ratio of frictional force to applied normal force. There are many designs of friction measuring setups: these can be classified in terms of range of load, range of speed, atmosphere in which they function, reciprocating vs. continuous motion, rotating vs. linear motion, spherical or cylindrical or flat shapes of sliding members, etc. Many setup configurations are available for purchase but all are variants of the basic motion-producing and force-measuring components.

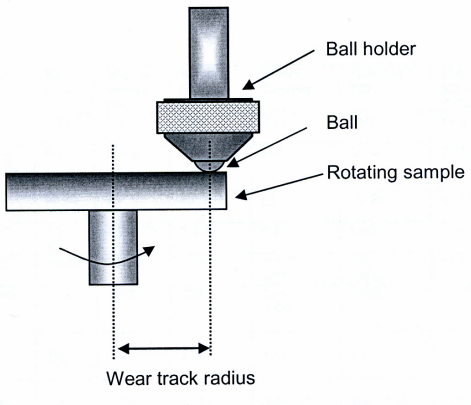

Figure 2.15 Schematic of ball on disk configuration (CSM High temperature tribometer).

A ball-on-disk configuration (Figure 2.15) is used in this study and described here. A flat or a sphere indenter is loaded onto the test samples with a precisely known weight. The pin or ball in mounted on a stiff lever, designed as a frictionless force transducer. As the disc rotates, the resulting frictional forces acting between the pin and the disc are measured by very small deflections of the lever using a LVDT sensor. Wear behavior for both the pin and the samples can be analyzed by measuring the respective volume loss during a specific friction run. This simple method facilitates the determination and study of friction and wear behavior of almost every solid state material combination, with varying time, contact pressure, sliding velocity, temperature, humidity, lubricants, etc.

The coatings were deposited on Si wafer, which were glued on steel disks and Φ6 mm 100Cr6 steel and Si_3N_4 ball counterparts were used to study the tribological performance of the coatings. The tests were performed for 10000 laps at a sliding speed of 10 cm/s, normal load of 5 N, at room temperature (20-23 °C), and constant relative humidity of 50%. The wear track radius in the range of 8-10 mm was used. 3D confocal micrographs of the wear tracks on the coatings were captured to measure the wear volume for calculation of the wear rates of the coatings. In the ball-on-disk configuration an area of the ball is continuously in contact with the coating, whereas the corresponding areas on the coated sample are in contact only once during a lap. The wear rate of the

coatings is defined as the volume of wear per unit track length, per Newton of normal load and per lap. Although the calculated value of the wear rate according to this definition is exactly the same as calculated from the total sliding distance of the ball (equal to the product of laps and perimeter of the wear track), its physical meaning is different from the commonly used dimension "mm^3/Nm" of wear rate. The latter is valid only for the configuration of a coated ball sample sliding against a disk. The wear volume of the steel ball, after the tribotest, was calculated by approximating the worn volume to a spherical cap. Since the height of the cap is much smaller than the ball radius R (3 mm), the wear volume can be approximated to $(\pi d^4)/(64 \cdot R)$ where d is the wear scar diameter. Optical and confocal microscopy was used to characterize the transfer film formed on the steel ball after the tribotest. The thickness of the transfer film was measured on three-dimensional images (512×512 pixels) of the wear scar on the steel ball, captured by confocal microscope after ultrasonically removing the wear debris. The WSxM® 4.0 Develop10.2 free software was used to select the pixels having transfer film on the confocal micrograph. The average and maximum thickness of the transfer film was then calculated by considering the z values all these pixels.

2.3.4 Confocal microscope:

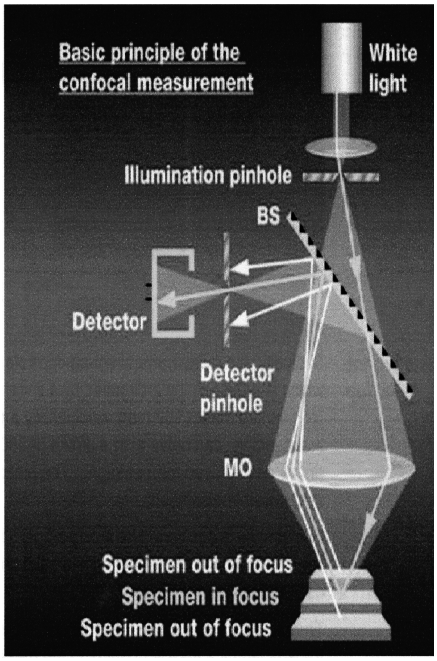

Figure 2.16 Operating principle of Confocal microscope, where BS is beam splitter, MO is multiple pinhole disc. Only the light reflected from the surface which is in focus is transmitted to the CCD camera.(Nanofocus® µsurf confocal microscope).

A confocal microscope is typically used to capture topographic height images over micrometer scales.[10] A Nanofocus® confocal microscope was used to capture 3D images

of wear tracks on the coatings, in order to calculate the wear rate, and also was used to characterize the transfer film formed on the ball counterparts after sliding against the coatings. The schematic of the confocal microscope is shown in Figure 2.16. The whole sensing head of the confocal microscope moves vertically by a stepper motor and/or only the objective moves in the vertical direction (z axis) by means of piezo drive. The unit scans a batch of various height levels of the surface to be measured. As whole areas are usually measured, the sample is not moved laterally during a measurement. The size of the measurement area depends on the applied objective and is listed in Table 2.1.

Table 2.1 Measurement field values, working distance, resolution and other optical parameters for different objectives used for confocal imaging:

Objective	20X	50X
Mesurement field (μm x μm)	700x660	290x280
Numerical Aperture	0.46	0.8
Working distance (mm)	3.1	0.66
Vertical resolution (nm)	40	15

The surface to be measured is illuminated through the microscope by an external xenon light source. Only those light beams which are focused on the detector (CCD chip) reach it. All unfocused light beams; i.e. all which are not at the same height are displayed by a pinhole. In such a way, a single point can be measured. The pinhole of the measurement head consists of a rotating Nipkow disk with approximately 120000 pinholes, which acts as multiple point sources scanning the surface. Surface areas which are at the same height level are mapped on the CCD chip. These height level records can then be joined to form a 2 or 3 dimensional image.

2.3.5 Raman spectroscopy

The chemical structure of the coatings was studied by Raman spectroscopy. Raman spectroscopy is a standard nondestructive tool for the characterization of crystalline, nanocrystalline, and amorphous carbons. Raman is light scattering by the change in polarisability χ due to lattice vibration[11].

$$\chi^{(k)} = \chi_0 + \frac{d\chi}{dq} Q(k,q) \qquad (2.5)$$

where χ is the polarisability at wavevector k, and Q is the amplitude of phonon of wavevector q. This change in polarisability causes an inelastic scattering of an incident photon (ω,k) into the scattered photon (ω',k'). (ω is the phonon frequency). In amorphous materials, Raman spectrum corresponds to vibrational density of states (VDOS) $G(\omega)$ weighted by the appropriate matrix element $G(\omega)$ according to the Shuker-Gammon formula

$$I(\omega) = \frac{n(\omega)+1}{\omega} C(\omega) G(\omega) \qquad (2.6)$$

The above equation describes quite well the Raman spectra of a-Si and a-Ge, which are sp^3 bonded only, by using a broadened version of the crystalline VDOS as $G(\omega)$. The visible Raman spectra of disordered carbons are in marked contrast. The Raman spectra of all disordered carbons are dominated by the relatively sharp G and D features of the sp^2 sites. This is because the π states are much more polarisable due to much greater cross section than that of σ states. The Raman spectra of DLC mainly show one or two prominent features, the G peak around 1580–1600 cm^{-1} and the D peak around 1350 cm^{-1}. The Raman spectrum is considered to depend on[11]: (1) clustering of the sp2 phases, (2) bond disorder, (3) presence of sp^2 rings or chains, and (4) the sp^2/sp^3 ratio. These factors act as competing forces on the shape of the Raman spectra, as shown schematically in Figure 2.17.

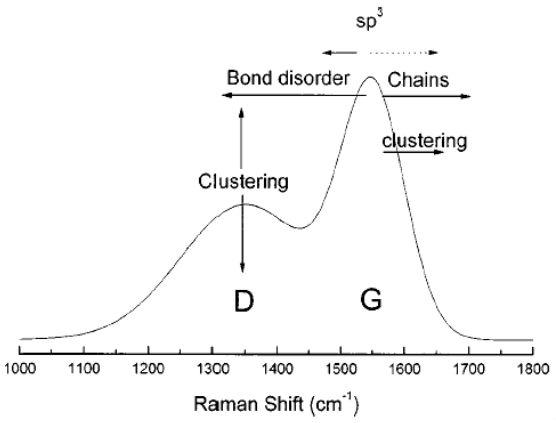

Figure 2.17 Schematic diagram of influences on the Raman spectra. A dotted arrow marks the indirect influence of the sp^3 content on increasing G position.[12]

The key property of interest in DLC is the sp^3 content. Raman spectroscopy is widely used on DLC's, and for a given restricted range of conditions, it is possible to indirectly derive the sp^3 content. The spectra are fitted by a Breit-Wigner-Fano (BWF) line for the G peak and a Lorentzian for the D peak. The BWF line shape is given by [12]

$$I(\omega) = \frac{I_0[1+2(\omega-\omega_0)/Q\varsigma]^2}{1+[2(\omega-\omega_0)/\varsigma]^2} \qquad (2.7)$$

where I_0 is the peak intensity, ω_0 is the peak position, ς is assumed as the full width at half maximum (FWHM) and Q^{-1} is the coupling or skewness coefficient.

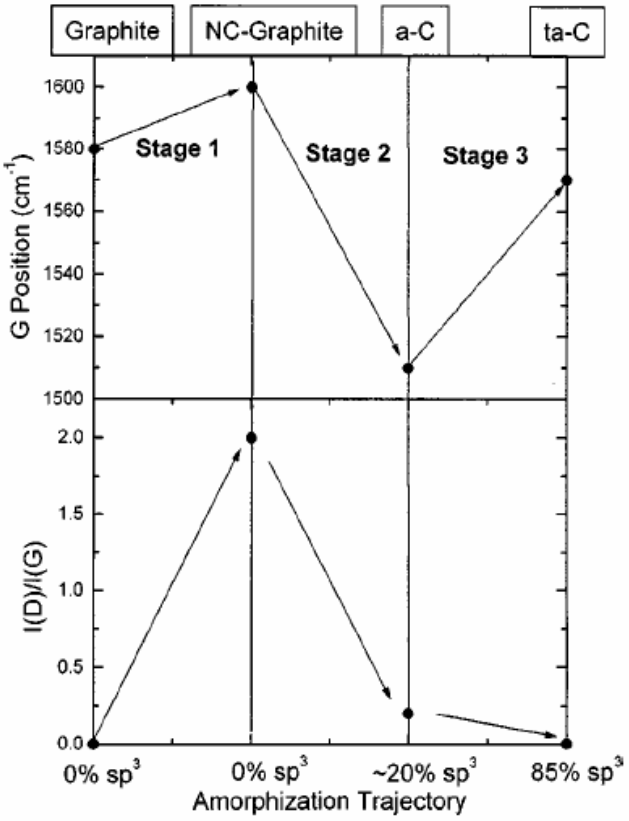

Figure 2.18 Three stage model, showing a schematic variation of the G *position and* I*(*D*)/*I*(*G*) ratio.*[12]

The Lorentzian line shape is recovered in the limit $Q^{-1} \rightarrow 0$. Note that because of skewness, the maximum of BWF occurs at

$$\omega_{\max} = \omega_0 + \frac{\varsigma}{2Q} \qquad (2.8).$$

Ferrari and Robertson[12] have shown that it is possible to classify the Raman spectra of amorphosn carbon with a three stage model, ranging from graphite to ta-C, as shown in Figure 2.18. The DLC based coatings studied in this work fall in stage 2 and hence it is described here. For the other stages, a reference is made to Ref. 12. In stage 2, defects are progressively introduced into the graphite layer, causing its phonon modes to soften, particularly the G peak. The Shuker-Gammon formula applies, and the VDOS is no longer that of graphite. The end of stage 2 corresponds to a completely disordered, almost fully sp^2-bonded a-C consisting of distorted sixfold rings or rings of other orders (~maximum 20% sp^3). The G peak decreases from 1600 to ;1510 cm^{-1} and I(D)/I(G) → 0. This indicates an introduction of sp^3 sites into a structure composed only of sixfold rings.[12]

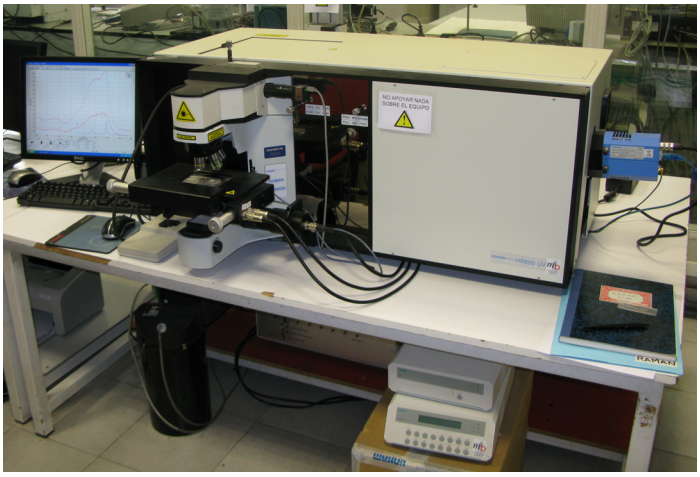

Figure 2.19 Photograph of LabRAM Horiba Jobin Yvon spectrometer (Photo courtesy Prof. J.C. Sanchez-Lopez, Instituto de Ciencia de Materiales de Sevilla - CSIC-Universidad de Sevilla, Spain).

All measurements were recorded under the same conditions (10 s of integration time and 10 accumulations) using a 100x magnification objective and a 100 μm pinhole. The spectra were analyzed by the fitting procedure described above.

References

1 P.J. Kelly, R.D. Arnell, Vacuum 56 (2000) 159
2 M. Ohring, The materials science of thin films, Academic press (1992).
3 D. Galvan, PhD thesis., University of Groningen. (ISBN 978-90-77172-28-5)
4 J. W. Bradley and T. Welzel, J. Phys. D: Appl. Phys. 42 (2009) 093001.
55 D. Barton, D.J. Heason, R.D. Short and J.W. Bradley Meas.Sci. Technol. 11 (2000) 1726.
6 J.W. Bradley, H. Bäcker, Y. Aranda-Gonzalvo, P.J. Kelly, R.D. Arnell, Plasma Source Sci. Technol. 11 (2002) 165.
7 Y.T. Pei, C.Q. Chen, K.P. Shaha, J.Th.M. De Hosson. Acta Mater., 56 (2008) 696-709.
8 G. Binning, C. F. Quate, Ch. Gerber. Atomic force microscope. Phys. Rev. Lett. 56, (1986) 930.
9 Arantxa Vilalta-Clemente and Kathrin Gloystein Principles of AFM, Physics of Advanced Materials Winter School 2008
10 H.J. Jordan, M. Wegner and H. Tiziani, Measurement Science and Technology 9 (1998) 1142.
11 J. Robertson, Mat. Sci. Engg R37 (2002) 129.
12 A. C. Ferrari and J. Robertson Phys. Rev. B 15 61 (2000) 14095

Chapter 3
GROWTH DYNAMICS OF NANOCOMPOSITE COATINGS*

In this chapter, surface roughness, dynamic growth behavior and microstructural evolution of TiC/a-C nanocomposite coatings deposited by pulsed-DC magnetron sputtering are described. From detailed analyses of surface morphology and growth conditions it is concluded that a transition in growth mechanisms occurs, i.e. a mechanism dominated by geometric shadowing at lower p-DC frequency evolving to a surface diffusion mechanism driven by impact-induced atomistic downhill flow process by Ar^+ ions at higher pulse frequency which leads to transition from a strong columnar to a columnar-free microstructure. Moreover, it is shown that rapid smoothing of initially rough surfaces with RMS roughness ~ 6 nm to < 1 nm can be effectively achieved with p-DC sputtering at 350 kHz pulse frequency. In order to analyze the smoothing mechanism the roughness evolution is described by a model; a linear stochastic differential equation with the second- and fourth-order gradient relaxation terms, which account for diffusion along the coating surface. Furthermore, the nonlocal shadowing effects in three spatial dimensions alongwith the angular distribution of depositing particles were included to explain the steep increase of roughness at 100 kHz p-DC sputtering. Simulation results

---

* This chapter is published in the following papers:

1. K.P. Shaha, Y.T. Pei, C.Q. Chen, J.Th.M. De Hosson. Pulsed-DC sputtered DLC based nanocomposite films: Controlling growth dynamics, microstructure and frictional properties. Mater. Technol. (2010) accepted.
2. K.P. Shaha, Y.T. Pei, C.Q. Chen, J.Th.M. De Hosson. Synthesis of ultra-smooth and ultra-low friction DLC based nanocomposite films on rough substrates. Thin Solid Films, (2010), in press, doi:10.1016/j.tsf.2010.08.094
3. K.P. Shaha, Y.T. Pei, C.Q. Chen, A.A. Turkin, D.I. Vainshtein, J.Th.M. De Hosson. On the dynamic roughening transition in nanocomposite film growth. Appl. Phys. Lett. 95 (2009), 223102.
4. Y.T. Pei, K.P. Shaha, C.Q. Chen, R. van der Hulst, A.A. Turkin, D.I. Vainshtein, J.Th.M. De Hosson. Growth of nanocomposite films: From dynamic roughening to dynamic smoothening. Acta Mater., 57 (2009), 5156.
5. A.A. Turkin, Y.T. Pei, K.P. Shaha, C.Q. Chen, D.I. Vainshtein, J.Th.M. De Hosson. On the evolution of film roughness during magnetron sputtering deposition. J. Appl. Phys., 108 (2010) 1.
6. A.A. Turkin, Y.T. Pei, K.P. Shaha, C.Q. Chen, D.I. Vainshtein, J.Th.M. De Hosson. Surface roughness evolution of nanocomposite thin films. J. Appl. Phys., 105 (2009), 013523.
7. Y.T. Pei, A.A. Turkin, C.Q. Chen, K.P. Shaha, D.I. Vainshtein, J.Th.M. De Hosson. Dynamic smoothing of nanocomposite films. Appl. Phys. Lett., 96 (2010) 151910.

are compared with the experimental data for 100 kHz and 350 kHz p-DC deposition. The model is in good agreement with AFM measurements of roughness evolution.

3.1 Introduction

During sputtering deposition there is an interplay between interface roughening generated by noise, smoothing driven by surface diffusion due to concurrent ion impingement and nonlocal effects generated by shadowing. Geometrical shadowing enhances growth front roughness. Without additional lateral relaxation processes, this would inevitably cause dynamic roughening i.e. increase of surface roughness as a function of deposition time.[1] As a result a rough surface will lead to columnar growth such that the column boundaries (CBs) originate at the networks of grooves on the growing surface and the hills become the spearheads of the columns. Such a columnar structure is undesired because the CBs are the potential source of failure, e.g. mechanical (cracking), chemical (corrosion) and thermal (oxidation). In contrast, ultra-smooth surfaces produce pinhole-free coatings which are of considerable technological importance, e.g. in magnetic disk storage systems.[2] In view of this, during the last two decades considerable effort has been devoted to the experimental investigation and theoretical understanding of roughness evolution of growth front roughness. [3-7]

Several models have been proposed for describing the dynamic behavior of growing surfaces. Shadowing and kinetic roughening are the primary mechanisms of surface roughening.[8-10] On the other hand, sputter re-deposition (or re-emission)[11,12], atomistic impact-induced downhill flow[3] and local melting by thermal spike[4], surface diffusion and relaxation at high homologous temperatures[13-15] are the proposed mechanisms that may smooth the growth front. In order to avoid Erhlich-Schwoebel barrier effects (the additional barrier for an adatom to diffuse down a surface step) and roughening due to crystallization, common practice is to employ an amorphous system for the study of dynamic scaling behavior of coating growth. In fact, amorphousness has been considered as the prerequisite for obtaining ultrasmoothness of thin coatings.[3,4]

Dynamic growth behavior of p-DC sputtered TiC/a-C nanocomposite coatings as a function of different pulse frequencies was investigated with particular emphasis on understanding the predominant growth mechanism that controls the microstructure of the coatings. Furthermore, to reveal the parameters and processes that control the growth front roughness, roughness evolution is described by the linear stochastic differential equation with the second- and fourth-order gradient relaxation terms, which accounts for diffusion along the coating surface.[16] The second-order term is attributed to ballistic effects resulting from continuous bombardment of the growing coating by Ar^+ ions. This model explains the experimentally observed dynamic smoothing for p-DC sputtered coatings at higher pulse frequency. The shadowing effect and the angular distribution of

depositing particles were included in the model to explain the dynamic roughening observed at lower pulse frequency.[17] A concept of the exposure angle, according to which the local growth rate at a point is roughly proportional to the exposure angle of this point[14,15] was considered. The model also takes into account the angular distribution of depositing particles. Both these models are briefly discussed. The simulation results are compared with the experimental observations for 100 and 350 kHz p-DC sputtered coatings.

3.2 Experimental

The TiC/a-C nanocomposite coatings were deposited with non-reactive magnetron sputtering of simultaneous DC sputtering of Ti and p-DC sputtering of graphite targets operating at different frequencies and 50% duty cycle. The substrates were pulsed biased at -40 V at 250 kHz and 50% duty cycle. The substrates were fixed at 80 mm distance to the targets and the rotational speed of the sample carrousel was 3 rpm during the deposition of coating. Prior to deposition, the acetone-washed Si substrates were further cleaned with Ar plasma etching for 15 minutes at -400 V bias voltage. A ductile CrTi interlayer of 170 nm thickness was first deposited to enhance the interfacial adhesion between the top coating and Si substrate. Thereafter, the TiC/a-C nanocomposite top coating was deposited under the condition of 1.5A sputtering current applied to each of the two graphite targets and 0.55A current to the single titanium target, for different deposition times from 7.5 minute up to 4 hour. The averaged growth rates were 8.5, 7.5 and 5.5 nm/min for p-DC sputtering at 100, 250 and 350 kHz, respectively. Moreover, intentionally rough coatings at 100 kHz were deposited to simulate a rough finishing of industrial substrates and dynamic growth behavior of coatings deposited at 350 kHz on such rough coatings were studied. A series of TiC/a-C top layers were deposited for various deposition times and at two p-DC frequencies, coded as xCyTi where x denotes pulse frequency applied to the graphite (C) targets in kHz and y denotes the current applied to Ti-target in ampere. The p-DC current applied to the graphite targets was always 1.5A each. The deposition rates were 8.0, 8.5 and 3.15 nm/min for 100C0.35Ti, 100C0.55Ti and 350C0.35Ti, respectively.

Atomic force microscopy (AFM) was used to probe the surface morphology of the coatings. Eight scans of size 2×2 μm² were captured for evaluating the surface roughness and height-difference correlation function. The captured AFM micrographs consisting of 512 lines were displayed and leveled by using a free software WSxM® 4.0 Develop10.2[18] and then exported to X-Y-Z ASCII files for calculating the height-difference correlation functions with a home-made code in MatLab software. The microstructural evolutions of the coatings were characterized by scanning electron microscopy (HR-SEM) and the nanostructure of the coatings was revealed by HR-TEM.

3.3 Results and discussion

In this section, the dynamic growth behavior and microstructure of TiC/a-C nanocomposite coatings deposited by p-DC sputtering at different pulse frequency, mainly 100 and 350 kHz are described.

3.3.1 Dynamic growth behavior and microstructure of p-DC sputtered TiC/a-C coatings

The typical evolution of the surface morphology of 100 kHz p-DC sputtered TiC/a-C nanocomposite with increasing deposition time is displayed in Figure 3.1.

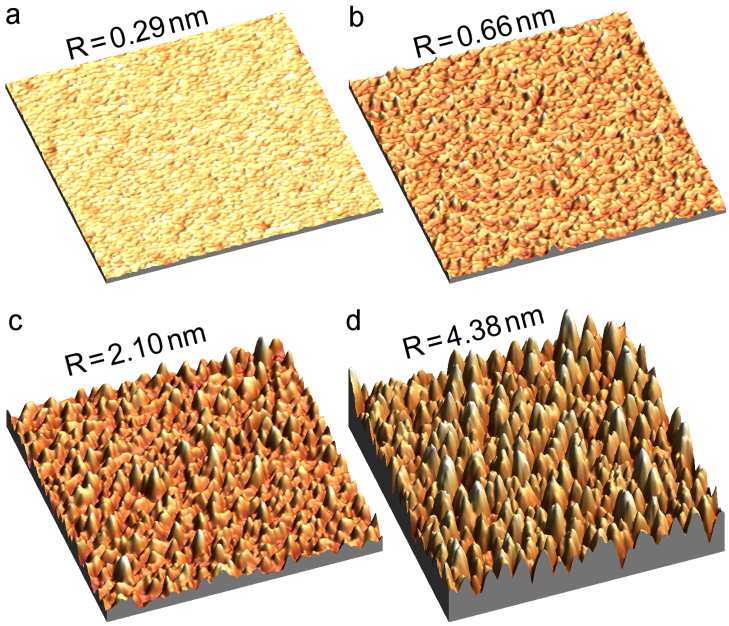

Figure 3.1 Surface topography images (2×2 μm²) showing evolution of the surface of 100 kHz p-DC sputtered TiC/a-C nanocomposite coatings at different deposition times: (a) 450 s, (b) 1800 s, (c) 7200 s and (d) 14400 s. The corresponding RMS roughness (R) is indicated.

The interlayer exhibited a grainy surface morphology with a "grain" size of around 50 nm (Figure 3.1a) and a roughness of 0.30 ± 0.01 nm. With increasing deposition time, the surfaces evolved gradually from a fine grainy structure to large hills surrounded by deep groove networks (Figure 3.1a-d), i.e. the features grew both vertically and laterally. As a result, the roughness increased rapidly from 0.30±0.01 nm to 4.24±0.06 nm after four hours of deposition time, indicating a dynamic roughening growth.

The 350 kHz p-DC sputtered coatings behave rather differently concerning their growth dynamics. The evolution of the surface morphology at different deposition time is demonstrated in Figure 3.2.

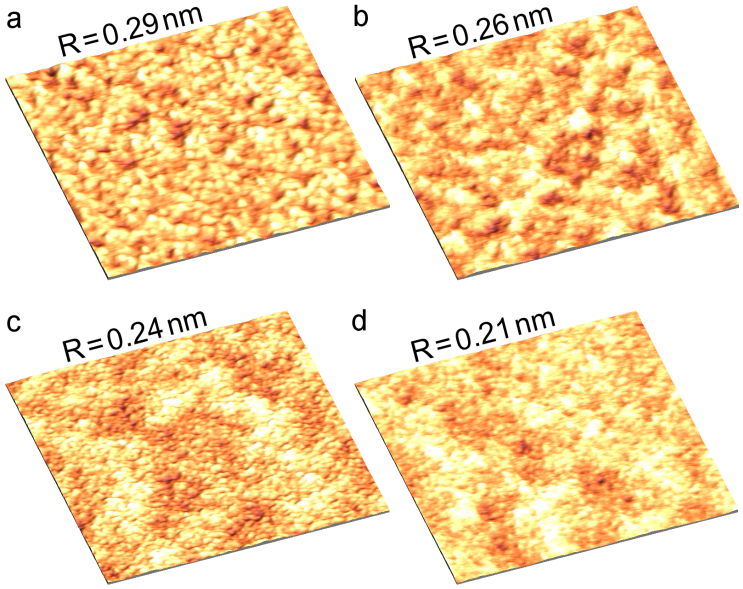

Figure 3.2. Surface topography images (1×1 μm²) showing the typical evolution of the surface morphology of 350 kHz p-DC sputtered TiC/a-C nanocomposite coatings at different deposition times: (a) 0 s (interlayer), (b) 900 s, (c) 3600 s and (d) 14400 s. The corresponding RMS roughness (R) is indicated.

During the onset of coating deposition, the grooves of the grainy surface (Figure 3.2a) gradually became less visible and the surface became smooth. After 15 minutes of deposition, as shown in Figure 3.2b, the neighboring grains merged to yield a smoother surface on one hand and on the other hand the growing bumps appeared even finer. At a deposition time of 60 minutes (Figure 3.2c), the growing surface became much smoother and exhibited tiny bumps of sizes almost one order of magnitude smaller than those observed on the interlayer. After 240 minutes of deposition time, the surface showed only weak contrast of nano-sized dots (Figure 3.2d) and appeared ever smoother with a roughness of 0.23±0.01 nm. It is clear that a dynamic smoothing process occurred due to intensified concurrent ion impingement (i.e. 350 kHz p-DC sputtering), as will be discussed in the following section.

The height-difference correlation function of the surfaces shown in Figure 3.3 provided statistical information about the morphology evolution of coatings versus deposition time. Here the height-difference correlation function was calculated from $H(r) = \left\langle [h(x) - h(x+r)]^2 \right\rangle$, where h is the height function at a position x on a scanned surface area and the angle brackets denote an average of the height-difference squared over the distance r along the fast scanning direction over an entire AFM micrograph. The height-difference correlation function takes the form $H(r) = 2w^2 f(r/\xi)$ with $H(r) = (mr)^{2\alpha}$ for $r << \xi$ and $H(r) = 2w^2$ for $r >> \xi$.[19,20]

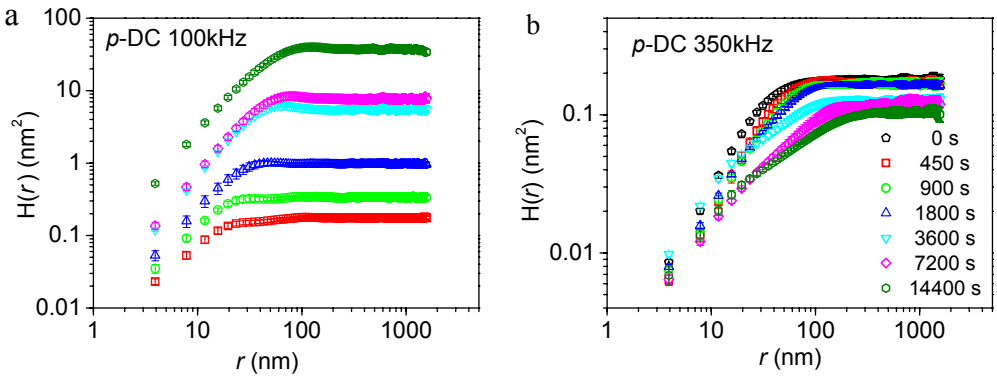

Figure 3.3 Height-difference correlation curve of the coatings grown for different times and p-DC sputtered at frequency of (a) 100 kHz and (b) 350 kHz. Note the error bars are within the thickness of the symbols.

The lateral correlation length ξ defines the lateral distance within which the surface heights of any two points are correlated and the width w is an equivalent of the RMS roughness measured by AFM The roughness exponent α describes the undulation, such that a larger value of α corresponds to a smoother surface structure whereas a smaller value of α corresponds to a locally more jagged morphology.

Table 3.1 Parameters of height-difference correlation function and RMS roughness of 100 kHz p-DC sputtered TiC/a-C nanocomposite coatings for different times.

Deposition time (s)	A	M	ξ (nm)	w (nm)	RMS (nm)
450	0.589	0.0105	21.66	0.30	0.30 ± 0.01
900	0.651	0.0200	21.68	0.41	0.41 ± 0.01
1800	0.734	0.0358	27.05	0.69	0.69 ± 0.02
3600	0.874	0.0775	36.14	1.70	1.71 ± 0.05
7200	0.869	0.0822	41.03	1.96	1.98 ± 0.09
14400	0.841	0.1779	52.13	4.30	4.24 ± 0.06

Table 3.2 Parameters of height-difference correlation function and RMS roughness of 350 kHz p-DC sputtered TiC/a-C nanocomposite coatings for different times.

Deposition time (s)	α	M	ξ (ξ2) (nm)	w (nm)	RMS (nm)
0	0.665	0.0070	42.3	0.30	0.30 ± 0.01
450	0.648	0.0049	52.7	0.29	0.29 ± 0.01
900	0.571	0.0034	62.3	0.29	0.29 ± 0.01
1800	0.562	0.0033	60.5	0.29	0.29 ± 0.01
3600	0.502	0.0022	59.0 (98.1)	0.25	0.25 ± 0.01
7200	0.471	0.0012	80.2 (119.6)	0.24	0.25 ± 0.01
14400	0.459	0.0011	73.0 (188.5)	0.23	0.23 ± 0.01

The calculated values of all the scaling parameters are listed in Table 3.1 and 3.2 for the coatings deposited at 100 and 350 kHz pulse frequency, respectively. The value of α

was derived from the slope of the initial linear part of the height-difference correlation curves. For the coatings deposited at 100 kHz, the roughness exponent α increased with increasing deposition time and saturated at 0.84~0.87. In contrast, for the coatings deposited at p-DC 350 kHz, the roughness exponent α decreased with increasing deposition time, ranging from 0.665 to 0.459. Moreover, the averaged local slope *m* showed a general decrease from 0.007 to 0.001 as the deposition time was prolonged from 0 to 4 hours, reflecting the dynamic smoothing governed by both the effects of reduced width and elongated lateral correlation length. The interface width (*w*) was consistent with the RMS roughness measured directly by AFM. It is noteworthy that a scaling behavior of different components was observed at one hour deposition time or longer, where the initial linear part of the height-difference correlation curves was spitted into two linear segments and the lateral correlation lengths were correspondingly defined (see Table 3.2).

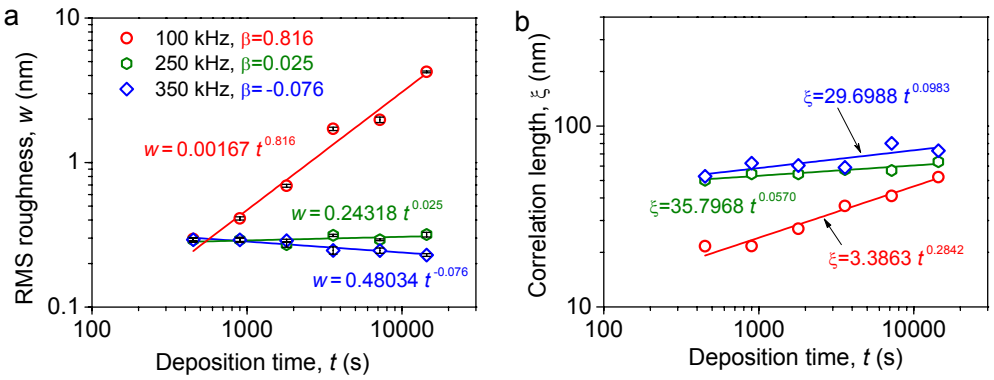

Figure 3.4 Dynamic scaling of the coatings: (a) surface roughness versus deposition time and the growth exponent β; (b) lateral correlation length versus deposition time.

In the hypothesis of dynamic scaling[19], both the width and the lateral correlation length evolve as power laws of the deposition time such that $w(t) \propto t^{\beta}$ and $\xi(t) \propto t^{1/z}$, where β is the growth exponent and z is the dynamic exponent that requires $z = \alpha / \beta$. The dynamic characteristic of the interface width and the lateral correlation length as a function of deposition time are depicted in Figure 3.4a and b, respectively. Since the deposition rate remained constant at a given frequency of p-DC sputtering, the exponents β and z of the power-law dynamic scaling functions are independent of whether the thickness of coatings or the deposition time is used along the horizontal axis in the graphs. From the log-log plot of the width versus deposition time (Figure 3.4a), the values of β are calculated as 0.816, 0.025 and -0.076 for the coatings sputtered at pulse frequency of 100, 250 and 350 kHz, respectively. Obviously, the growing surface of the nanocomposite coatings exhibited both dynamic roughening and smoothing behaviors that are correlated to the intensity of concurrent ion impingement. As discussed in chapter 2, the energy flux of the impinging Ar^+ ions onto the growing surfaces is 2.34×10^{17},

4.47×10^{18} and 1.26×10^{19} eV m^{-2} s^{-1} in the case of p-DC sputtering at frequency 100, 250 and 350 kHz, respectively. With a high enough intensity of concurrent ion impingement such as the situation at 250 kHz p-DC sputtering, dynamic roughening ceased and the evolution of the outer surface roughness became stable with a growth exponent close to zero. At even higher intensity of impingement at 350 kHz p-DC sputtering, a negative growth exponent was obtained indicating a dynamic smoothing process. Considering the values of the roughness exponent α and the exponent 1/z according to Figure 3.4b, β has been calculated, by using $z=\alpha/\beta$, as 0.031-0.040 and 0.045-0.065 for the coatings sputtered at p-DC frequency of 250 and 350 kHz, respectively. These values are in reasonable agreement with that derived from Figure 3.4a, i.e. β is close to zero. Thus, the scaling exponents for the TiC/a-C nanocomposite coatings deposited with 350 kHz p-DC sputtering are $\alpha \sim 0.55$ and $\beta \sim 0$. Similarly, for the 100 kHz p-DC sputtered coatings β was calculated as 0.167~0.248, which differs significantly from the growth exponent according to Figure 3.4a ($\beta = 0.816$). This indicated that the dynamic roughening was mainly attributed to the vertical growth of the surface features (hills) as shown in Figure 3.1, with only a slightly lateral growth. It should be kept in mind that the growing surface is non-stationary indicated by the time-dependent α and the AFM measurements at different growth time are performed on different areas.

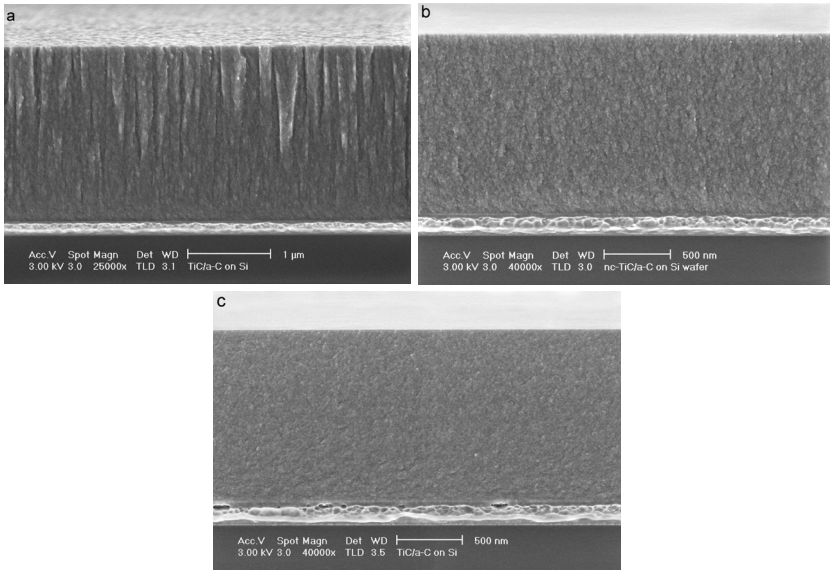

Figure 3.5 SEM micrograph showing the fracture cross-section of TiC/a-C nanocomposite coatings sputtered for four hours at different p-DC frequencies: (a) 100 kHz, (b) 250 kHz and (c) 350 kHz.

Cross sectional micrographs of the TiC/a-C coatings are shown in Figure 3.5. The 100 kHz p-DC sputtered coating in Figure 3.5a shows a rough surface which exhibits large hills as already observed in the AFM micrograph in Figure 3.1d. The most remarkable observation is the formation of a columnar structure, where the diameter of

the columns grows significantly with coating thickness. In contrary, the coating deposited at 250 kHz was column-free and exhibit smooth surface, but showed a slightly coarser microstructure (Figure 3.5b). Similarly, the 350 kHz p-DC sputtered coating in Figure 3.5c exhibited a very smooth surface, and fully dense and columnar-free microstructure.

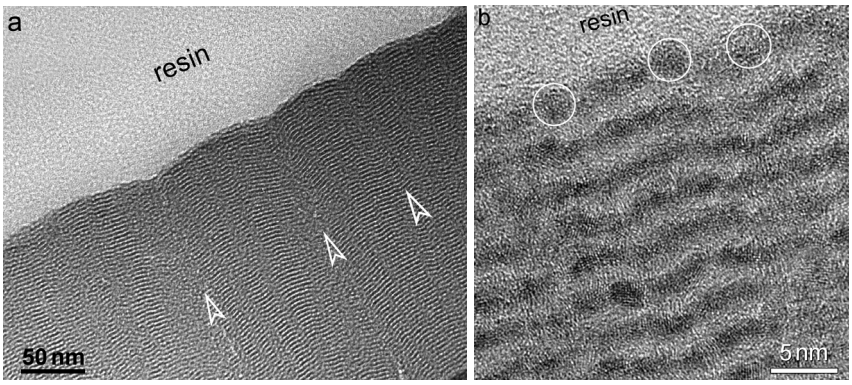

Figure 3.6 (a) XTEM overview of the 100 kHz p-DC sputtered TiC/a-C nanocomposite coating 100K240, with arrows indicating the boundaries of columns; (b) high resolution XTEM micrograph showing the details of the growing surface and the multilayers, with circles indicating the formation of TiC nanocrystallites already in the first sublayer.

Cross sectional TEM observations of the 100 kHz and 350 kHz p-DC sputtered coatings are presented in Figure 3.6 and Figure 3.7, respectively. The multilayers can be easily recognized in the coating deposited at 100 kHz (Figure 3.6a), where a wavy profile of the outer surface correlated to the columnar structure. HRTEM observations reveal that the multilayered structure consisted of TiC/a-C nanocomposite sublayers and a-C sublayers in alternation (Figure 3.6b).

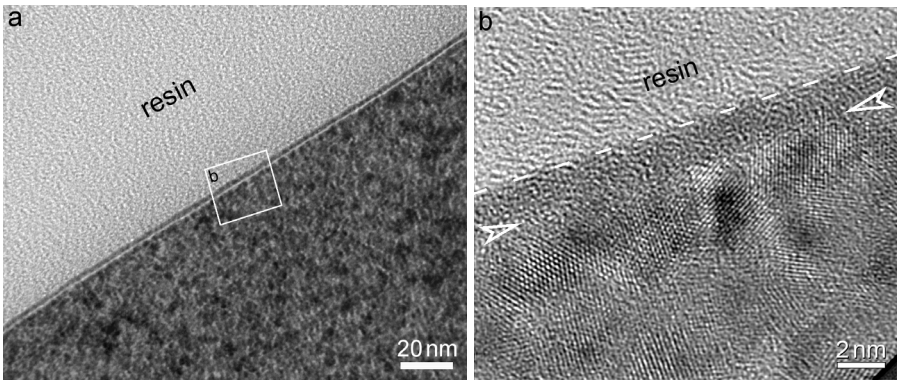

Figure 3.7 (a) Overview and (b) high resolution XTEM micrograph of the 350 kHz p-DC sputtered TiC/a-C nanocomposite coating, revealing that an amorphous front layer of about 2 nm thickness covers the bulk nanocomposite coating with its internal interface indicated by two arrows.

The most interesting observation in the case of 350 kHz p-DC sputtered films was the super flat outer surface and especially a sharp amorphous front layer of about 2 nm thickness that covered the bulk nanocomposite (Figure 3.7b). The TiC nanocrystallites

were formed only beneath this amorphous front layer and can be considered as the tracer of crystallization process under intensively concurrent ion impingement. In the subplantation model proposed for the formation of sp^3 carbon bonding and *ta*-C growth[21-23], a very thin surface layer of sp^2 bonded carbon is expected, with its thickness depending on the subplantation depth. The existence of such a sp^2 layer of low density has been confirmed only by the intensity contrast in XTEM and spatially resolved EELS in STEM[24,25], and reproduced by MD simulation[3]. Clearly, verification of the growth modes of DLC-based nanocomposite coatings is essential in the study of dynamic smoothing behavior of growing surfaces, in particular whether the nanocrystallites are formed directly at the surface or underneath in relation to the evolution of surface profile. The amorphous front layer in TiC/a-C nanocomposite coatings identified by high-resolution XTEM micrographs (Figure 3.9b) provides the evidence that ultra-smoothness can be achieved only in amorphous coatings or coatings grown via an amorphous front layer. By comparing the nanostructure of the coatings deposited at 100 and 350 kHz in Figure 3.6b and Figure 3.7b, respectively, it is confirmed that the concurrent Ar^+ ions impingement of high energy flux induces the formation of the amorphous front layer. This observation supports the subplantation model[21,-23] and the downhill flow model[3] where amorphousness is the prerequisite. The formation of such an amorphous front layer excludes any influence of nanocrystallites on the dynamic growth behavior and roughness evolution of the nanocomposite coatings.

3.3.2 Dynamic smoothing and microstructural evolution for coatings deposited on rough surfaces:

In the above section it is shown that dynamic growth behavior of thick TiC/a-C coatings grown by p-DC sputtering on smooth surface depends upon the applied pulse frequency. At higher pulse frequency dynamic roughening was completely suppressed and rather dynamic smoothing was revealed. For industrial applications, one of the major concerns is to obtain smooth coatings on rough substrates, i.e. how rough the finishing of substrates can be smoothed in coating deposition. In this section the question “Can dynamic smoothing be achieved for these coatings grown on initially rough surfaces?” is addressed. Rough TiC/a-C coatings were grown on Si substrates at 100 kHz pulse frequency on purpose to simulate a rough finishing of industrial substrates and then deposition was continued at 350 kHz to check the feasibility of smoothing of such rough surfaces.

In order to study the dynamic growth behavior, series of TiC/a-C top layers were deposited for various deposition times and at two p-DC frequencies, coded as xCyTi where x denotes p-DC frequency powering the graphite (C) targets in kHz and y the sputtering current applied to Ti-target in ampere. The p-DC current applied to the

graphite targets was always 1.5A each. The deposition rates were 8.0, 8.5 and 3.15 nm/min for 100C0.35Ti, 100C0.55Ti and 350C0.35Ti, respectively.

The evolution of the surface morphology of 100C0.35Ti layers with increasing deposition time is shown in Figure 3.8a-c. The surface exhibited hills surrounded by network of valleys. The features grew laterally and the peak-to-valley distance extended with increasing deposition time. Consequently, the RMS roughness increased from 1.65±0.03 nm at 30 min to 5.93±0.15 nm at 90 min indicating dynamic roughening, similar to that observed in the above section. However, with the onset of deposition with 350 kHz p-DC sputtering on the rough surface(Figure 3.8c), as seen in Figure 3.8d, the shape of the hills turned from sharp pyramids in Figure 3.8c to round bumps and the hills were broadened.

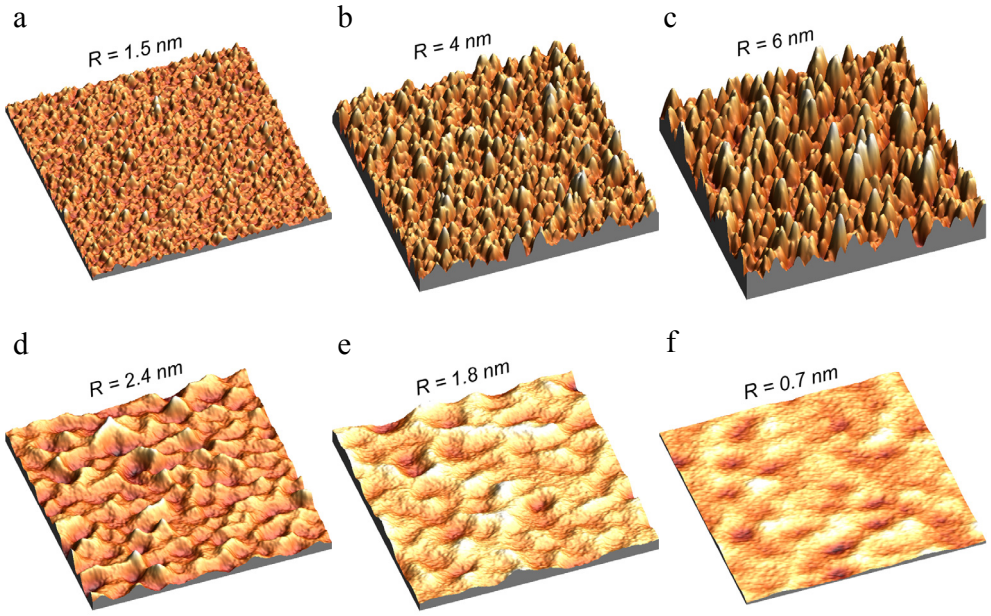

Figure 3.8 AFM micrographs (2×2 μm²) of TiC/a-C nanocomposite coatings deposited by p-DC sputtering at different pulse frequencies and deposition times: at 100 kHz pulse frequency for (a) 30 min, (b) 60 min, (c) 90 min; and at 350 kHz pulse frequency [deposited on surface (c)] for (d) 45 min (e) 90 min and (f) 180 min. The corresponding RMS roughness (R) is indicated.

As the deposition progressed, the hills merged into each other at the bottom of the valleys (Figure 3.8d-f), which was due to the preferred growth of the valley in the midst of the hills. This is in accordance with the densification under ion assisted coating growth.[26] The peak-to-valley distance decreased and the RMS roughness reduced to 0.7±0.02 nm after 180 min of deposition time indicating dynamic smoothing. Figure 3.9 presents the surface roughness evolution of TiC/a-C coatings as a function of deposition time and frequency of p-DC sputtering graphite targets.

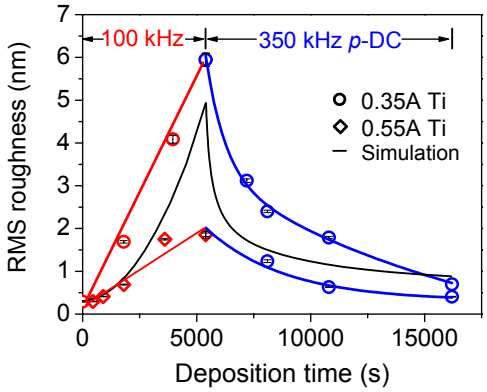

Figure 3.9 Surface RMS roughness of TiC/a-C coatings as a function of deposition time and p-DC frequency. Rapid smoothing effect was fitted by exponential decay for the 350C0.35Ti top layers. The black curves are the simulated results.

It is interesting to note that the surface roughness of the layers deposited at 100 kHz frequency experienced continuous roughening (similar to that observed in section 3.3.1) and those of 350 kHz p-DC sputtered layers, deposited on initial rough surfaces, exhibited dynamic smoothing instead. In addition, the sputtering current applied to Ti-target also plays a role. By intentional use of different currents to Ti-target, two different levels of roughness were achieved after 90 min of deposition time with 100 kHz p-DC sputtering, i.e. 5.93±0.15 nm with 0.35A and 1.85±0.04 nm with 0.55A current to Ti-target, respectively. Thereafter, rapid smoothing has been observed with 350 kHz p-DC sputtering, i.e. no matter how high the initial roughness was. Within a limited deposition time of 180 min, however, the final roughness was related to the initial roughness. It must be noted that in the case of 350 kHz p-DC sputtering, the RMS roughness was decreased from an initial value of 5.93 ±0.15 nm to about 0.7 nm. This clearly demonstrated that smooth coatings can be deposited on initial rough (~ 6 nm RMS roughness) surfaces by 350 kHz p-DC sputtering.

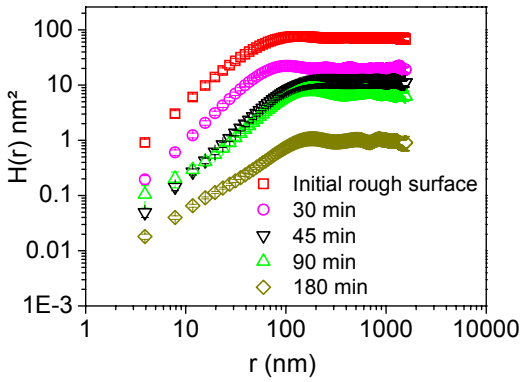

Figure 3.10 Log-log plot of height-difference correlation function for initial rough surface (deposited at 100 kHz) and 350 kHz p-DC sputtered TiC/a-C nanocomposite coatings deposited for various deposition times as indicated. (Note the error bars inside the symbols).

The change in pulse frequency causes a transition of dominating growth mechanism that controls the coating growth. To understand the growth mechanism the coatings were further investigated with height-difference correlation function, as described in section 3.3.1 and is shown in Figure 3.10. The values of α and ξ for 100C0.35Ti series were calculated from the height-difference correlation function, and the exponent 1/z was calculated from the log-log plot of ξ versus growth time. Consecutively, β was calculated, by using $z=\alpha/\beta$, as 0.53 ± 0.02. Alternatively, β was calculated from the log-log plot of *w* versus growth time as 1.13. The considerable difference in the values of β implied the breakdown of self-affinity of the system due to presence of nonlocal growth effects such as geometrical shadowing.[27] This is well supported by previous theoretical or experimental studies which revealed that if the geometrical shadowing effect dominates in the coating growth the value of β will be equal to or above 0.5.[28-31] Similarly for 100C0.55Ti coatings, the scaling relationships between the exponents cease to exist, the power law scaling behavior gave $\beta = 0.84$. Thus, increasing the current of Ti target to 0.55A reduced the absolute value of the interface width as well as the value of β, indicating that the interface width grew less rapid than that of the 100C0.35Ti coatings. This was due to increased Ar^+ ion flux impinging at the growing interface with increasing target current. Thus, geometrical shadowing, where taller surface features block the nonnormal incident flux from reaching lower-lying areas of the surface, dominated the coating growth to yield dynamic roughening in 100 kHz p-DC sputtered coatings.

The dramatic decrease in the surface roughness as a function of growth time during 350 kHz p-DC sputtering is interesting since it indicated the presence of surface diffusion driven growth. The log-log plot of w versus growth time for 350C0.35Ti coatings gave values of β as -0.76 and -0.96 respectively indicating surface smoothing. The flux and energy distribution of impinging ions at the growing interface play a crucial role in achieving the smoothing effect. During 350 kHz p-DC sputtering a high Ar^+ ions and energy flux was delivered to the growing coating, as discussed in chapter 2. Also the plasma fills the whole chamber ensuring continuous impingement of the growing coating in a closed-field unbalanced configuration. The intensive ion impingement on the growing interface provides an important contribution to the surface diffusion of adatoms during the growth of the coating. Furthermore, the Ar^+ ions impinge more likely at the surface protrusions or hills rather than in the valleys. It means that the ion impingement can erode hills and fill in the valleys. At the final stage of the growth at 180 min, the surface became smoother and the peak-to-valley distance decreased. The value of α, calculated from height-height correlation function, for these coatings show decreasing trend from 0.7 to 0.5 with increasing deposition time indicating formation of sub-nanometer crater formation in the vicinity of impact site.

A very low roughness and $\beta \sim 0$ have been observed by Casiraohi et. al. in *ta*-C thin coatings deposited with filtered cathodic vacuum arc[4] and the smoothing mechanism is proposed to be local melting induced by impact induced thermal spikes. The basic idea in this model is that the energy of the depositing C ions dissipates locally as heat in a so called thermal spike of ~ 1 ps and that this heat causes a local surface melting. During this time, surface energy minimization flattens the surface locally. They observed an increase in α with deposition time. However, in the case of 350 kHz p-DC sputtered coatings, the local surface becomes more jagged at an atomic level during the dynamic smoothing process as evidenced by the reduced α with deposition time (Table 3.2). Thus, the thermal spike model is not applicable to the dynamic smoothing at 350 kHz. Also, in comparison with the work by Casiraohi et. al., we have observed the dynamic smoothing effect in much thicker coatings (1.5 μm thickness versus < 100 nm), revealing a more general phenomenon of dynamic smoothing of growing surfaces induced by concurrent Ar^+ ion impingement. Moreover, the dynamic smoothing is active in a coating system consisting of nanocrystalline phases with a size one order of magnitude larger than the roughness of the coatings. Recently, Moseler et. al.[3] proposed an impact induced downhill flow model, where they attributed the intrinsic ultra-smoothness of DLC films to the impact of carbon ions which induce downhill currents of atoms in the top layer of the film. Their simulation suggested formation of sub-nanometer craters (surface locally becomes rough) in the vicinity of the impact sites can lead to surface fluctuations which further are efficiently dampened by erosion of the hills into neighboring valleys. Also, they concluded that amorphicity is another important prerequisite for achieving ultra-smoothness. The underlying film must be disordered; the presence of crystallinity or ordered areas on a nanometer scale will lead to roughening of the film. The hypothesis of this model is consistent with the 350 kHz p-DC sputtered coatings since the surface became locally rough, as evidenced by decrease in α.

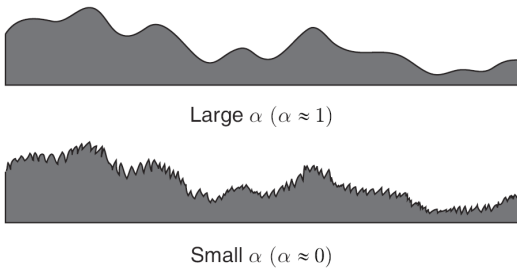

Figure 3.11 This diagram shows a comparison of the local surface morphology for surfaces with similar values for the interface width w, but different values of α. A smaller value of α implies a rougher local surface.[32].

The roughness exponent α characterizes the short-range roughness, with larger values of α representing a smoother local surface profile. Surfaces with different values of α are depicted in Figure 3.11. Also, the top front layer of the 350 kHz p-DC sputtered

coatings was amorphous which is consistent with the requirement of the model. Thus, it is believed that the intensive and continuous impingement with high flux and high energy ions cause impact induced downhill flow of adatoms, in the presence of top amorphous front layer, as proposed by Moseler et al. This surface diffusion competes with the geometrical shadowing and noise induced roughening to evolve surface smoothing. However, during 100 kHz p-DC sputtering, the Ar^+ ion and energy flux is quite low compared to the case of 350 kHz p-DC sputtering. Also the plasma does not cover the whole chamber. Under these growth conditions the surface diffusion does not provide enough lateral relaxation yielding dynamic roughening. Another contribution to the increase in roughness may be the strength of the shot noise, which is expected to increase with deposition rate.[33]

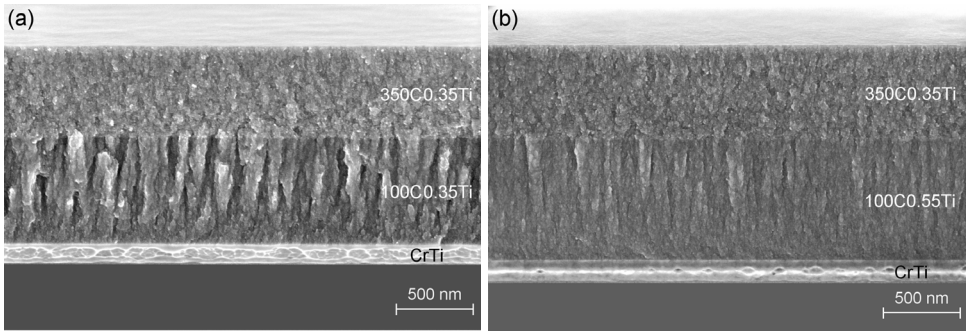

Figure 3.12 Cross sectional SEM micrographs of TiC/a-C coatings deposited with p-DC sputtering graphite targets first at 100 kHz for 90 min and then at 350 kHz for 180 min: (a) 100C0.35Ti-350C0.35Ti and (b) 100C0.55Ti-350C0.35Ti. Immediate transition of microstructure from columnar to column-free is observed at the switch of pulse frequency.

Figure 3.12 shows the microstructural evolution of the coatings 100C0.35Ti-350C0.35Ti and 100C0.55Ti-350C0.35Ti, respectively. During 100 kHz p-DC sputtering, the microstructure showed strong columns but evolved as dense and non columnar structure in the onset of 350 kHz p-DC sputtering.

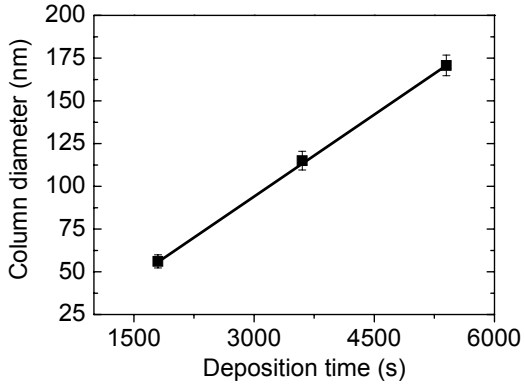

Figure 3.13 Evolution of column diameter as a function of deposition time for 100 kHz p-DC sputtered TiC/a-C nanocomposite coatings.

The evolution of column diameter as a function of deposition time for p-DC 100C0.35Ti layer is shown in Figure 3.13. Considering the roughness evolution with time for 100 kHz p-DC sputtering (Figure 3.9), it is evident that the rapid growth of columns (Figure 3.13) from approximately 56 nm at 30 min to 170 nm at 90 min is directly in accordance with the steep increase in surface RMS roughness from approximately 1.6 nm at 30 min to 5.9 nm at 90 min. Nevertheless, a smaller surface roughness corresponds to a weaker character of columnar microstructure in the 100C0.55Ti layer (see Figure 3.9 and Figure 3.12b). It is important to note that increasing the current to Ti target gives a weak columnar structure as shown in Figure 3.12b compared to Figure 3.12a during 100 kHz p-DC sputtering. The formation of columns in these coatings can be restrained if the growth front can be smoothed. This is evident due to the microstructural evolution of the TiC/a-C nanocomposite coatings revealed in Figure 3.12, namely the transition from dynamic roughening to dynamic smoothing with increasing frequency of p-DC sputtering due to intensified concurrent ion impingement. Thus, the growth mechanisms essentially determine the growth front roughness evolution and hence the microstructure of these coatings. If shadowing effects dominate the growth, it magnifies the initial surface roughness yielding columns separated by void regions. And if surface diffusion dominates it effectively erases the initial rough surface structure to yield column-free microstructure.

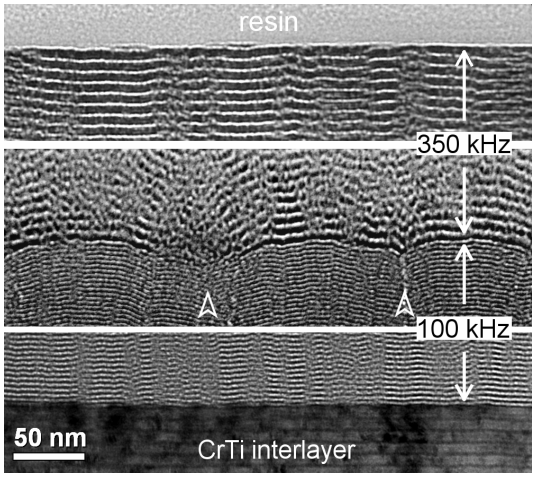

Figure 3.14 Cross-sectional TEM micrograph of the TiC/a-C coating 100C0.55Ti-350C0.55Ti. The evolution of the multilayered structure clearly reveals that the increased roughness during 100 kHz p-DC sputtering was smoothed out by the following 350 kHz p-DC sputtering.

XTEM (cross-sectional Transmission Electron Microscopy) was also performed to reveal the internal structure evolution during growth of the coating along the thickness direction. As shown in Figure 3.14, both the 100 kHz layer and the 350 kHz layer exhibited multilayered structures. The column boundaries grown during 100 kHz p-DC sputtering are indicated by open triangles in Figure 3.14. In the early period of 100 kHz

p-DC deposition, the columns do not develop due to a low surface roughness. Rather, the columns gradually occur and rapidly grow when the coating grows to a thickness of approximately 200 nm, as shown by both the XSEM (cross-sectional Scanning Electron Microscopy) and XTEM micrographs in Figure 3.12 and Figure 3.14. Considering the roughness evolution with time for 100C0.35Ti coatings (Figure 3.9), it is evident that the rapid growth of columns is directly in accordance with the steep increase in surface RMS roughness from approximately 1.6 nm at 30 min to 4 nm at 60 min. The immediate suppression of the columnar structure was apparent and independent of surface roughness in both the cases of 350 kHz p-DC deposition, and the structure evolves as fully homogeneous within 100 nm thickness growth. Correspondingly, the roughness developed during 100 kHz deposition was smoothed out rapidly by the following 350 kHz deposition as clearly revealed by the XTEM observation.

3.3.3 Simulation:

To understand the mechanisms of dynamic smoothing of the growing interface and to reveal the parameters and processes those control the evolution of interface roughness in these coatings, a phenomenological model is briefly discussed and the experimental data are analyzed accordingly. Several models of roughening kinetics and the scaling behavior of random surface structures during coating growth are reviewed in Refs. [1,34,35]. In particular kinetic Monte-Carlo models are frequently used for the simulation of coating growth on an atom-by-atom basis using probabilistic rules to govern deposition, diffusion and other growth processes. The drawback of this approach is that it requires a detailed knowledge about all processes taking place on an atomic scale. A continuum approach that is based on a stochastic differential equation was considered.[16] The continuum models proved to be useful for the understanding of roughening kinetics, despite the complexity of the growth process on atomic scale. Since the roughness of the coatings deposited in our experiments was very low, a "minimal" equation of interface motion (without nonlinear terms) was considered which contains the Edwards-Wilkinson term $D_2\nabla^2(...)$ [36] and the Mullins term $D_4\nabla^2\left(\nabla^2(...)\right)$ [37]

$$\frac{\partial h(\mathbf{r},t)}{\partial t} = D_2\nabla^2 h(\mathbf{r},t) - D_4\nabla^2\left(\nabla^2 h(\mathbf{r},t)\right) + \eta(\mathbf{r},t) \qquad (3.1)$$

$$h(\mathbf{r},0) = h_0(\mathbf{r}) \qquad (3.2)$$

where D_2 and D_4 are the positive diffusivity parameters that control the atomic mobility along the interface, $h(\mathbf{r},t)$ is the deviation of the interface profile $Z(\mathbf{r},t) = h(\mathbf{r},t) + Ft$ from the flat interface of the growing coating of mean thickness $\langle Z(\mathbf{r},t)\rangle = Ft$ and $h_0(\mathbf{r})$ is the initial (substrate) profile. The stochastic noise term $\eta(\mathbf{r},t)$

is related to the fluctuations of deposition flux and is assumed to be Gaussian and uncorrelated with zero mean. The noise covariance is given by

$$\langle \eta(\mathbf{r},t)\eta(\mathbf{r}',t')\rangle = D\delta(\mathbf{r}-\mathbf{r}')\delta(t-t') \tag{3.3}$$

where $\langle ... \rangle$ stands for the ensemble average, $\delta(\mathbf{r}-\mathbf{r}')$ is the two-dimensional delta-function. The scaling behavior of Eq. (3.1) in various limiting cases has been studied in Ref. 38. The diffusion terms in Eq. (3.1) become comparable at the length scale

$$L^* = \sqrt{\frac{D_4}{D_2}} \tag{3.4}$$

Therefore the smoothing process is governed by the fourth derivative term on scales smaller than L^*, the second order Edwards-Wilkinson term dominates on scales larger than L^*. The formal solution to Eq. (3.1) can be written as

$$h(\mathbf{r},t) = \Im^{-1}\left(\Im\left(h_0(\mathbf{r})\right)e^{-a(q)t}\right) + \Im^{-1}\left(\int_0^t \Im\left(\eta(\mathbf{r},t')\right)e^{-a(q)(t-t')}dt'\right) \tag{3.5}$$

where $a(q) = D_2 q^2 + D_4 q^4$, $\mathbf{q}$ is the vector in 2D reciprocal space. $\Im$ and $\Im^{-1}$ stand for the direct and inverse Fourier transforms, respectively. Note that the first term decreases with time, i.e. the contribution from the initial profile diminishes with deposition time or coating thickness.

3.3.3.1 Deposition noise strength

An exact calculation of the deposition noise strength is hardly possible. However it can be estimated using simple arguments. The growth rate of the coating consists of two contributions: (i) deposition of C-atoms and (ii) coating sputtering by Ar-ions $F = F_+ - F_- = \left(\alpha_C j_C^+ - j_C^-\right)\Omega$, where Ω is the mean volume per atom in the coating, and j_C^+ and j_C^- represent the flux of carbon atoms to the substrate and re-sputtered from the substrate, respectively.

The sticking coefficient α_C<1 (the fraction of collisions which result in the capture of carbon atoms by the thin coating).[39] The maximum deviation of the growth rate from the average value is about the growth rate itself $|\max(\eta)| \sim F_+$, therefore in the relation $\langle \eta(\mathbf{r},t)\eta(\mathbf{r}',t')\rangle = D\delta(\mathbf{r}-\mathbf{r}')\delta(t-t')$ the term in the left hand side is about F_+^2. In the right hand side the combination $\delta(\mathbf{r}-\mathbf{r}')\delta(t-t')$ was estimated as $\delta(\mathbf{r}-\mathbf{r}')\delta(t-t') \sim \Omega^{-2/3}\tau_0^{-1}$, where $\Omega^{2/3}$ is the minimal "atomic area" and $\tau_0 \sim \Omega^{1/3}F_+^{-1}$

is the average time interval between arrivals of atoms to that minimal area occupied by a single atom. Hence the strength of the deposition noise is proportional to the thin coating growth rate

$$D = F_+ \Omega \tag{3.6}$$

Re-sputtering of a growing thin coating due to concurrent ion impingement is statistically independent of deposition. Re-sputtering is equivalent to the arrival of atoms of "antimatter", therefore re-sputtering contributes additively to the growth noise

$$D = F_+ \Omega + F_- \Omega = \left(\alpha_C j_C^+ + j_C^-\right)\Omega^2 \tag{3.7}$$

This expression shows that the optimum parameters of the p-DC power supply should be selected in order to avoid re-sputtering of the thin coating and, at the same time, to ensure sufficient mobility of surface atoms due to the impingement of Ar+ ions.

3.3.3.2 Estimation of diffusion coefficient D_2

As with any deposition method, the growth of a coating is driven by a random arrival of atom/ions onto the substrate. If the adatoms have no or only limited possibility to migrate along the surface, the deposition noise inevitably causes a rapid increase of the interface roughness as a function of coating thickness.[1,35] The smoothing of initially rough interface during deposition of ta-C has been explained in Ref. 4 by local melting in the region of impact-induced thermal spikes that result in a reduction of local surface curvature. However, in Ref. 3 on the basis of MD simulations[39] it was noticed that the size and duration of a thermal spike in amorphous carbon seem too small for the establishment of a liquid-like behavior. Instead, the smoothness of DLC thin coatings deposited with carbon ion beam has been explained by ballistic effects resulting in downhill diffusion along the inclined surface.[3] This mechanism is likely relevant to our case of p-DC magnetron sputtering deposition. From MD simulations the authors of Ref. 3 concluded that Edwards-Wilkinson diffusion flux along the interface is given by

$$\mathbf{j}_2 = -J_C \Omega \nu(E) \nabla h = -D_2 \nabla h \tag{3.8}$$

where J_C is the carbon-ion flux, $\nu(E)$ is the smoothing strength that is proportional to the sum of lateral atomic displacements in the vicinity of an energetic particle impinged on the thin coating. According to Ref. 3, $\nu(E)$ increases linearly with the energy of incoming carbon ions up to the value of about 2 nm at $E^* \approx 120$ eV, then it saturates because for higher energies ions penetrate into the subsurface layer and release a part of the impact energy in the bulk.

In the case of p-DC magnetron sputtering deposition, the Edwards-Wilkinson diffusion coefficient can be written in terms of Ar+ flux to the growing thin coating

$$D_2 = \Omega \int \nu(E) f_{Ar}^{S}(E) dE = b\Omega \int_0^{E^*} E f_{Ar}^{S}(E) dE + bE^* \Omega \int_{E^*}^{\infty} f_{Ar}^{S}(E) dE \quad (3.9)$$

Here the energy distribution of Ar+ ion flux to the substrate is denoted as $f_{Ar}^{S}(E)$ and $\nu(E)$ can be approximated by the dependence

$$\nu(E) = \begin{cases} bE & E < E^* \\ bE^* & E > E^* \end{cases} \quad (3.10)$$

where b is a constant independent of the energy of impinging ions. The first term in the RHS of Eq. (3.9) is proportional to the total energy delivered by the low energy Ar+ ions to the subsurface layer of the thin coating. The second term shows that only a fraction of energy of the energetic ions is available to induce diffusion along the surface, the rest of the energy is released in the bulk of the thin coating.

3.3.3.3 Estimation of diffusion coefficient D_4

Following Mullins[37], the kinetic coefficient D_4 is usually attributed to the interface diffusion of adatoms driven by the gradient of the chemical potential along the interface, which is associated with the gradient of the local curvature. Under near-equilibrium conditions the Mullins expression for the coefficient D_4 is given by

$$D_4 = \frac{D_s \gamma \Omega^2 n}{k_B T} \quad (3.11)$$

where D_s is the coefficient of interface diffusion, γ is the interface energy and n is the number of interface atoms per unit area. In the case of non-equilibrium process of crystal growth (molecular beam epitaxy) the number of interface atoms is determined by the balance between the arrival rate of incoming atoms and the rate of their absorption by steps; the step density is determined self-consistently by kinetics of nucleation and attachments of adatoms to step edges. For amorphous thin coatings it is not clear how to define the number of interface atoms or the number of interface defects that absorbs arriving atoms.

3.3.3.4 Comparison with the experimental data

To compare the simulated result with the experimental data of surface roughness evolution of 350 kHz p-DC sputtered coatings in section 3.3.1, the deposition noise was fixed at the value $D = 6.5\text{x}10^{-4}$ nm^4/s that corresponds to the mean atomic volume $\Omega = 6.5\times10^{-3}$ nm^3. The parameters D_2 and D_4 were adjusted to obtain a good fit to experimental data. The fitting procedure is detailed in Ref. 16.

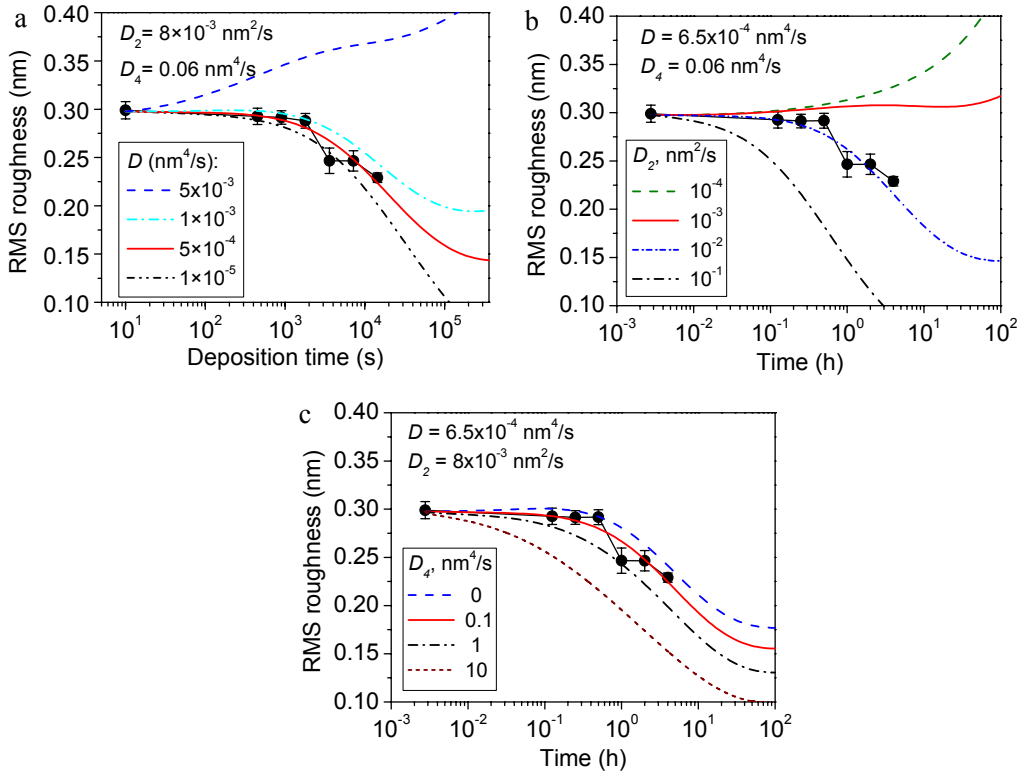

Figure 3.15 Time dependence of the RMS roughness at various values of the parameter (a) D; (b) D_2 and (c) D_4.

A good agreement with experimental data was obtained at $D = 6.5\times10^{-4}$nm^4/s, D_2 = 8×10-3 nm^2/s and $D_4 = 0.06$ nm^4/s. The dependence of the RMS roughness on the model parameters for the cases of 100 hours of deposition time along with the experimentally measured roughness values is shown in Figure 3.15. At a given "smoothing efficiency" D_2 and D_4, the interface roughness decrease significantly with the deposition time but may also increase upon time once the deposition flux is beyond a threshold (Figure 3.15a). Therefore the deposition flux comes into play mainly at high growth rates where dynamic roughening is observed. Figure 3.15b shows the influence of the diffusivity parameter D_2 on the time dependence of interface roughness. It is noteworthy that variation of D_2 can affect considerably the dynamic behavior of interface roughening/smoothing. The gradient of chemical potential along the interface and the local temperature increase due to the energy delivered to the growth front by impinging Ar^+ ions may also lead to smoothing by means of surface diffusion through the coefficient D_4 (Figure 3.15c), which has only a minor effect as compared to that of the parameter D_2. This means that the Edwards-Wilkinson relaxation term dominates in the process. That is to say, the smoothing process is governed by the second order Edwards-Wilkinson term on length scales larger than the critical length scale $L^* = \sqrt{D_4 / D_2}$ (a

couple of nanometer for the simulated cases in Figure 3.15), and the fourth derivative term becomes dominant only on scales smaller than L*. Roughness can be controlled effectively by increasing the mobility of adatoms with concurrent ion impingement. Figure 3.15b shows the influence of the diffusivity parameter D_2 on the time dependence of RMS roughness. However the fourth-order term is necessary in order to reproduce the shape of the PSD and the RMS slope observed experimentally.[16]

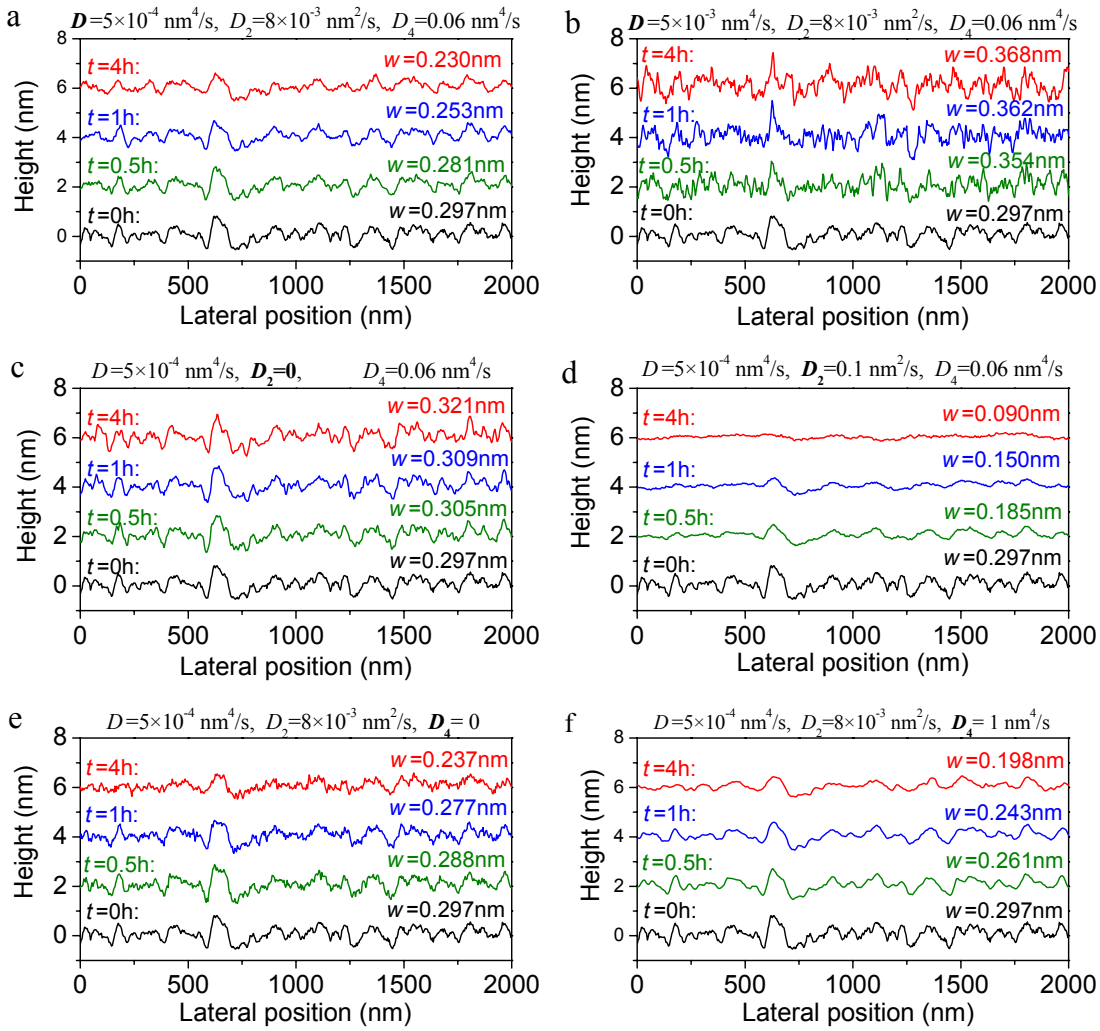

Figure 3.16 Numerically simulated interface profiles versus deposition time (t), with the interfaces width (w) indicated: (a) profiles simulated with the basic set of parameters to fit the experimental result plotted in Fig. 3.15; (b) with high deposition noise; (c) with no D_2 diffusion; (d) with high value of D_2 diffusivity; (e) with no D_4 diffusion and (f) with high value of D_4 diffusivity. For clarity, each profile is shifted along z-axis by 2 nm.

To visualize the effect of the diffusivity parameters and the noise strength on the interface evolution, the growth front profiles of the coating were simulated by numerical evaluation of the Eq. 3.5 on a 512×512 lattice (i.e. 2000×2000 nm² area). The deposition

noise $\eta_{nm}^{\alpha} = \sqrt{D/(\Delta x^2 \Delta t)}\xi_{nm}^{\alpha}$ has been generated at the lattice points (x_n, y_m) (Δx is the spacing between points) at all time moments $t \le t_{\alpha}$ with a time increment Δt. The random numbers ξ_{nm}^{α} are taken from the Gaussian distribution with mean zero and unit variance. The "discrete" deposition noise η_{nm}^{α} has the same variance as the spatial average of the continuous noise $\eta(\mathbf{r},t)$ on the square area Δx^2 around (x_n, y_m) integrated over the time interval Δt. The initial interface $h_0(\mathbf{r})$ has been extracted from the AFM micrograph in Figure 3.2a, and then Eq. 3.5 was integrated numerically. The results are presented in Figure 3.16, where each figure demonstrating the sensitivity of the interface profile and roughness to a variation of the parameters D, D_2 and D_4, respectively. The results of the numerical simulation clearly confirm that both dynamic roughening and smoothing are observed and dominated by the noise strength D (Figure 3.16a and b). At a fixed deposition rate or noise strength D, the coefficient D_2 of the second order Edwards-Wilkinson term controls the smoothing process of the low-frequency or large-scale interface undulations (Figure 3.16a, c, and d), whereas the coefficient D_4 of the Mullins term is responsible for the high-frequency or small-scale undulations (see Figure 3.16a, e, and f).

The time dependence of RMS roughness of coatings deposited at 100 kHz p-DC is essentially linear with $\beta \sim 1$, where β is the growth exponent. In local models of random deposition the largest growth exponent $\beta = 1/2$ is attained at zero mobility of atoms along the surface.[40] This implies that some other roughening mechanism besides noise is present during deposition with p-DC magnetron sputtering. The fast growth of roughness can be attributed to geometrical shadowing, the process in which some parts of the surface are shadowed from the incoming flux by other parts of the growing surface.[41-49] Initially, the smooth surface roughens due to the noise. If the depositing particles strike the substrate from a broad range of angles, the shadowing effect sooner or later becomes important. Peaks of the surface undulation are exposed to incoming particles from all directions, and thus grow faster than the average growth rate. At the same time, valleys of the surface undulation receive fewer particles since they are screened by peaks; therefore, their growth lags behind. This leads to instability of the planar surface and results in the development of a mountain landscape or columnar structure, i.e. the coating becomes extremely rough if the surface mobility of atoms is too low.

To understand the rapid increase in roughness of the coatings deposited at 100 kHz p-DC sputtering, the shadowing effects in three spatial dimensions and the angular distribution of depositing flux were included in the model described in the previous section. The important role of angular distribution of depositing flux, which is inevitably

connected to the motion of substrates passing by one magnetron to another, is highlighted. Furthermore, the influence of diffusion parameters on the evolution of surface morphology was investigated.

The necessary prerequisite of the shadowing effect is the angular distribution of the incident particle flux.[1] In the magnetron sputtering system, the shadowing effect must be essential, because the flux of depositing particles has an angular distribution due to the structure of the magnetron installation (finite size of sputtering targets, rotation of sample holder in a cylindrical configuration or linear motion in a planar arrangement of magnetrons, etc). As an example we simulate the coating growth with a realistic angular distribution of depositing particles, which has been constructed by taking into account the cylindrical configuration of magnetrons. Simulation results are in good agreement with the experimental data on 100 kHz and 350 kHz p-DC deposition described in section 3.3.2.

A three-dimensional continuum model was considered with the additional term, which takes into account the angular distribution of depositing particles

$$\frac{\partial h(\mathbf{r},t)}{\partial t} = F\left(\mathbf{r},\{h\}\right) + D_2\nabla^2 h(\mathbf{r},t) - D_4\nabla^2\left(\nabla^2 h(\mathbf{r},t)\right) + \eta(\mathbf{r},t) \quad (3.12)$$

$$F\left(\mathbf{r},\{h\}\right) = \int_0^{2\pi} d\varphi \int_0^{\theta(\varphi)} f(\theta',\varphi)\sin\theta' d\theta' \quad (3.13)$$

where $f(\theta,\varphi)$ is the angular distribution of depositing particles, integration is carried out over the exposure solid angle $\Omega\left(\mathbf{r},\{h\}\right)$ at a point $\mathbf{r}$ (Figure 3.17). The exposure solid angle depends on the surface profile around the point $\mathbf{r}$ and is as follows:

$$\Omega\left(\mathbf{r},\{h\}\right) = \int_0^{2\pi} d\varphi \int_0^{\theta(\varphi)} d\theta' \sin\theta' \quad (3.14)$$

where θ is the polar angle and φ is the azimuthal angle in the local spherical coordinates with the origin at the surface point $\mathbf{r}$. $\theta(\varphi)$ defines the maximum angle of a line of sight access to the surface point $\mathbf{r}$.

D_2 and D_4 are the positive diffusivity parameters, as discussed before. The important feature of the growth equation (3.12) is that shadowing, noise and relaxation are assumed to contribute additively to the roughness evolution. In a real situation other effects can be present. For example the diffusion coefficient D_2 may depend on position on the coating surface because of possible influence on the ion flux of a higher electrical field in the vicinity of the surface protrusions with a high curvature.

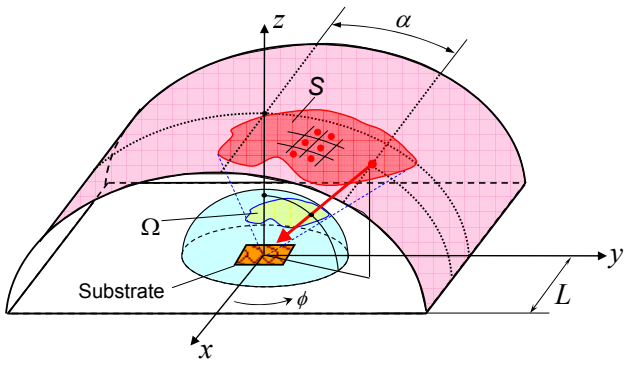

Figure 3.17 System geometry used in modeling the flux of atoms onto a planar substrate. Real discrete targets in the magnetron installation are replaced with the continuous cylindrical surface that emits atoms. Label S denotes the area that is seen from a given position on the growing coating, i.e. which lies within the solid angle Ω.

It should be noted that there exists a non-local smoothing mechanism in addition to diffusion along the surface. Depending on deposition conditions, particles can either stick to or bounce off from their impact points depending on a sticking coefficient. Nonsticking particles are reflected diffusely (or re-emitted) and can arrive at other surface points including shadowed valleys.[49] At sticking coefficients close to unity, the shadowing effect becomes the dominant process and columnar rough morphologies start to form.[50] To avoid computational difficulties in Eq. (3.13) the reflection of depositing flux from the coating surface is neglected.

To analyze the growth equation dimensionless variables were considered where the length scale l_0 and time scale τ_0 were defined as:

$$l_0 = D_2/G, \tau_0 = l_0/G \qquad (3.15)$$

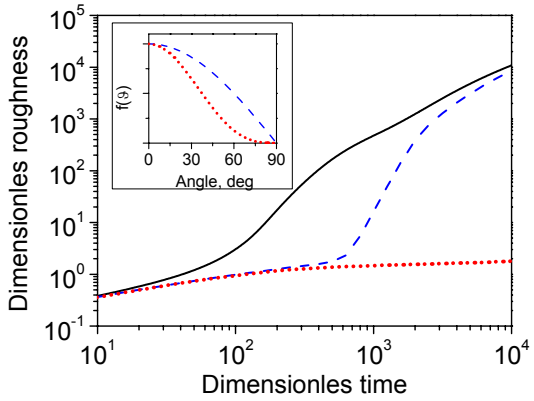

Figure 3.18. Influence of the angular distribution of depositing flux on the development of shadowing instability considering the angular distribution of deposition flux $f(\theta,\varphi) \propto \cos^n(\theta)$. The solid line correspond to $n = 0$, the dashed and dotted lines correspond to n = 1 and 3, respectively (corresponding distributions are shown in the insert).

In Figure 3.18 we compare the time dependence of the RMS roughness of a coating obtained with the angular distribution $f(\theta,\varphi) \propto \cos^n(\theta)$, where $n = 0, 1, 3$. It is seen that for the $\cos^3(\theta)$ distribution the RMS roughness evolve very slow. For this type of distribution the fraction of particles with polar angles close to $\theta = 90^o$ is small compared to the uniform distribution. In practice, a collimation of the sputtered particles is an efficient way to reduce the fraction of particles depositing at oblique angles and to suppress the surface roughness.[51] However collimation can not be used for deposition on a substrate of a complicated shape.

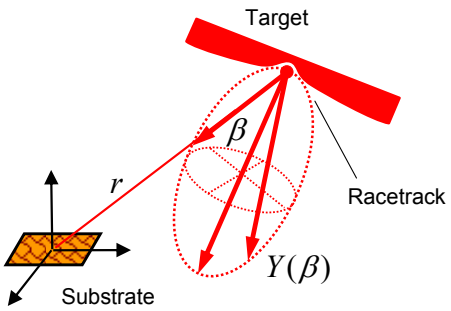

Figure 3.19 Angular emission distribution of sputtered atoms. The target with the racetrack is shown schematically. Experimentally a deep racetrack is observed on the target. Therefore it is assumed that atoms are mostly emitted from the racetrack with the "over-cosine" sputtering yield $Y(\beta) \propto \cos^n \beta$, $n > 1$

In a real installation, the flux of depositing particles exhibit an angular dependence, which is determined by the geometry of the sputtering chamber, collision and scattering of particles in the plasma depending on the working pressure, rotation/motion of targets/substrates, etc. The working gas tends to randomize directions from which particles approach the substrate. The angular distribution $Y(\beta)$ of atoms emitted from the surface of the target due to normally incident ions is usually assumed to follow a cosine-like distribution $Y(\beta) \propto \cos^n \beta$, where β is the ejection angle (Figure 3.19) of the sputtered atoms with respect to the surface normal[52,54]. Because of a special magnetic field configuration in the magnetron installation the deep racetracks form on targets. Therefore the sputtering yield can be strongly "over-cosine" $Y(\beta) \propto \cos^n \beta$ with $n > 1$.

Schematically, the deposition installation consisted of several targets emitting atoms that are depositing onto the substrates mounted on a rotating carousel (Figure 3.20). To find the angular dependence of the atomic flux to the substrate we use the following simplifications (Figure 3.20): 1. The frame of reference is fixed to the substrate, then the targets rotates around the substrate; 2. The rotating targets are approximated by a cylindrical surface emitting particles.

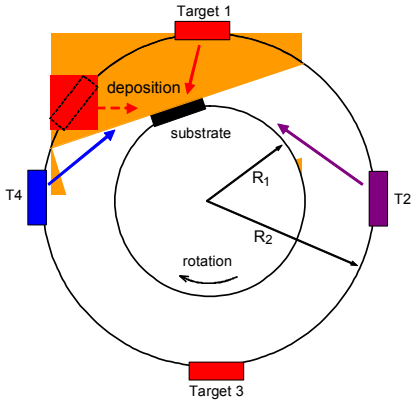

Figure 3.20 Configuration of the used magnetron sputtering system. The substrate receives sputtered atoms from the region labeled as "deposition".

Particles emitted from the cylindrical surface are assumed to follow a linear path to the substrate. The flux of particles depositing to the point (x_0, y_0) on the substrate is the sum of contributions of all surface elements $dS = R_2 d\alpha dx$.

$$F(x_0, y_0) = R_2 \int_{S(x_0,y_0)} \frac{Y(\beta(\alpha,x))}{(r(\alpha,x))^2} d\alpha dx \qquad (3.16)$$

where R_2 is the radius of cylindrical chamber on which the targets are installed (see Figure 3.20), α and x are the coordinates on the cylindrical surface, $r(\alpha,x)$ is the distance from the source point to the point on the substrate, $Y(\beta)$ is the angular emission distribution of sputtered particles, $\beta(\alpha,x)$ is the angle between the local normal and direction to the target (see Figure 3.19). Note that the flux decreases as the square of the distance away from the source

A simple cosine-like emission distribution was considered that agrees with the Sigmund approximation of linear cascade sputtering[52,53] and experimental data on sputtering of various polycrystalline targets [54,55]

$$Y(\beta) = A\cos^n \beta \qquad 1 \le n \qquad (3.17)$$

The normalization constant A is related to the mean growth rate G of a smooth coating by the relation

$$G = A R_2 \int_{-L}^{L} \int_{0}^{\alpha_{max}} \frac{\cos^n(\beta)}{r^2} d\alpha dx ,$$

where the integration is carried out over the whole area that emits particles.

It was shown that the angular distribution of depositing particles that corresponds to Figure 3.17 is given by [17]

$$f(\theta,\phi)=\begin{cases}\dfrac{Y(\beta)}{\cos\beta} \\ 0 \qquad \text{if} \quad \theta>\theta_{max}(\phi)\end{cases} \tag{3.18}$$

where $\theta_{max}(\phi)$ defines the "perimeter" of the cylindrical source of particles and $\cos(\beta(\theta,\phi))=\sqrt{\cos^2\theta+1-(R_1/R_2)^2\sin^2\theta\sin^2\phi}$.

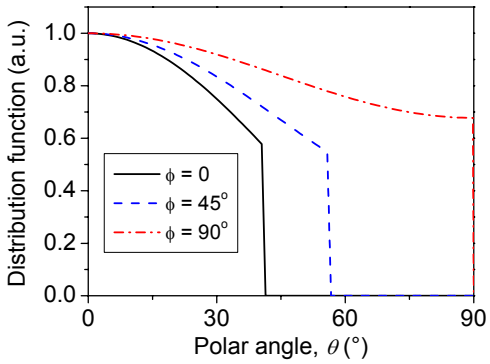

Figure 3.21 The dependence of distribution on polar angle plotted for several values of azimuthal angle. The sputtering yield $Y(\beta)\propto\cos^3\beta$. *Geometrical parameters are listed in Table 3.3.* $\phi=0$ *corresponds to the cross-section y = 0 (see Figure 3.17).*

Figure 3.21 shows the dependence of particle distribution on polar angle plotted for several values of azimuthal angle. The particle distribution is anisotropic in respect to the azimuthal angle. In principle, if the relaxation mechanisms are not strong enough this may result in an anisotropic surface structure.

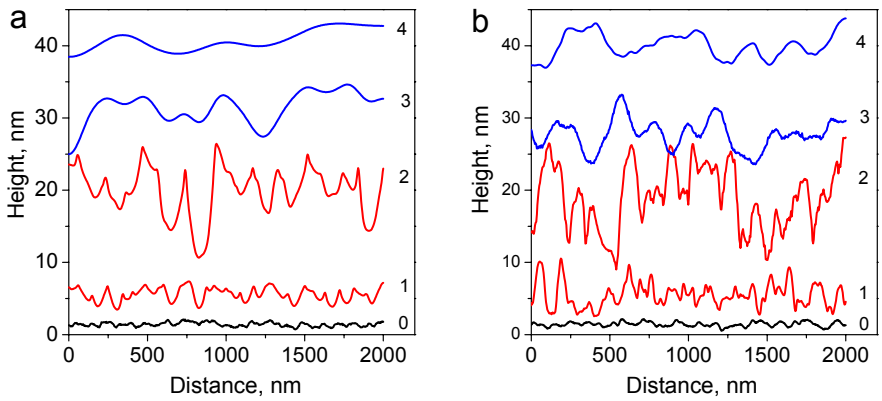

Figure 3.22 Evolution of the coating surface profile. The sections x =const are taken from the central part of the simulation area (a) and the experimental AFM data (b). Profiles are shifted along the vertical axis by arbitrary values to make the roughness evolution clear. Labels have the following meaning: 0 denotes the initial profiles; 1 and 2 refer to deposition at 100 kHz for 0.5 and 1.5 hr; 3 and 4 refer to deposition at 350 kHz for additional 0.5 hr and 1.5 hr, respectively.

The model predictions are compared with the experimental data. Eqs. (3.13) and (3.18) are used to find the flux in each point of the surface. The initial surface profile is taken from an AFM scan of TiCr interlayer (Figure 3.2a). To avoid contribution of deep narrow holes to RMS roughness the AFM measurements are simulated with a parabolic tip (r ~ 10 nm). The input parameters for deposition simulation are listed in Table 3.3. The configuration of the deposition system and the coating growth rate correspond to the experiments.

Table 3.3 Parameters used for simulation during 100 kHz and 350 kHz p-DC sputtering.

Pulse frequency	100 kHz	350 kHz
Growth rate, G , nm/s	0.13	0.05
Deposition noise, D, nm4/s	1×10-3	4×10-4
Diffusion coefficients, D_2 , nm2/s	0.05	2
Diffusion coefficients, D_4 , nm4/s	0.5	1
System geometry, mm	L = 70, R1 = 105, R2 = 185	
Sample size, nm (512×512 points)	2000	
Sputtering yield	$Y(\beta) \propto \cos^3 \beta$	

The results of the calculations with the found angular distribution of "cylindrical magnetron" are shown in Figure 3.9 and Figure 3.22. Depositions with 100 kHz p-DC sputtering were simulated (labeled as 100 kHz in the figures) up to 1.5 hours and then the simulations were continued by increasing the diffusion coefficients D_2 and D_4 to describe the higher flux of Ar^+ ions drawn to the substrate during 350 kHz p-DC sputtering. Figure 3.22 shows that the shadowing effect leads to amplification of initial large scale roughness during 100 kHz p-DC sputtering with a high deposition rate. At the same time small scale features disappear due to the diffusion along the coating surface. With increasing the diffusion coefficients D_2 and D_4 the surface becomes smoother; and only large scale hills remain, the size of which is comparable with the dimension of the simulation area. At the chosen diffusion parameters the anisotropy of the angular distribution (Figure 3.19) did not result in noticeable anisotropy of the coating surface. In Figure 3.9, the simulation results are compared with the RMS roughness measured experimentally. The numerical calculations presented in this section clearly reveal the influence of the deposition conditions and the diffusion parameters on the transition to shadowing growth.

3.4 Conclusions

With increasing intensity of concurrent ion impingement by raising the frequency of pulsed DC sputtering, a transition in predominant growth mechanisms occurs during growth of TiC/a-C nanocomposite coatings, i.e. a mechanism dominated by geometric shadowing at a p-DC frequency of 100 kHz evolving to a surface diffusion mechanism driven by impact-induced atomistic downhill flow process by Ar^+ ions at a p-DC frequency of 350 kHz. This leads to a transition from dynamic roughening to dynamic smoothing in the growth behavior of TiC/a-C nanocomposite coatings, in correspondence with a transition of the coating microstructure from columnar to columnar-free. As a solid proof of the impact-induced downhill flow model and subplantation model, an amorphous front layer of 2 nm thickness is observed to always cover the bulk nanocomposite during 350 kHz p-DC sputtering. The formation of such an amorphous front layer excludes any influence of nanocrystallites on the dynamic growth behavior and roughness evolution of the nanocomposite coatings. The predicted evolution of surface roughness based on a linear equation of surface growth which contains two gradient terms $D_2\nabla^2(...)$ and $D_4\nabla^2\left(\nabla^2(...)\right)$ is in good agreement with the atomic force microscopy measurements of roughness evolution for 350 kHz p-DC sputtered coatings. The angular distribution of depositing particles strongly influences the intensity of shadowing growth effects. Particles depositing at oblique angles (with polar angles close to $\theta = 90^o$) initiate the shadowing growth which dominates the growth and leads to dynamic roughening for 100 kHz p-DC sputtered coatings. By selecting the angular distribution function of depositing particles the shadowing instability can be effectively suppressed.

References

1.A.L. Barabasi, H.E. Stanley, Fractal Concepts in Surface Growth (Cambridge Univ. Press, Cambridge, 1995).

2. P.R. Goglia, J. Berkowitz, Hoehn J, Xidis A, Stover L. Diam Relat Mater 10 (2001) 271.

3. M. Moseler, P. Gumbsch, C. Casiraghi, A. C. Ferrari, and J. Robertson, Science 309 (2005) 1545.

4. C. Casiraghi, A. C. Ferrari, R. Ohr, A. J. Flewitt, D. P. Chu, and J. Robertson, Phys. Rev. Lett. 91 (2003) 226104.

5. J.M. López. Phys Rev Lett 83 (1999) 4594.

6. E.A. Eklund, R. Bruinsma, J. Rudnick, R.S. Williams. Phys Rev Lett 67 (1991) 1759.

[7]7. M. Kardar, G. Parisi, Y-C Zhang. Phys Rev Lett 56 (1986) 899.

8. B. Reinker, M. Moske, K. Samwer. Phys Rev B 36 (1997) 9887.

9 .M. Pelliccione, T. Karabacak, C. Gaire, G.C. Wang, T.M. Lu. Phys Rev B 74 (2006) 125420.

10. W.M. Tong, R.S. Williams. Annu Rev Phys Chem 45 (1994) 401.

11. J.T. Drotar, Y.P. Zhao, T.M. Lu, G.C. Wang. Phys Rev B 61 (2000) 3012.

12. E.A. Eklund, E.J. Snyder, R.S. Williams. Surf Sci 285 (1993) 157.

13. P.I. Tamborenea, S. Das Sarma . Phys Rev E 48 (1993) 2575.

14. K.R. Bray, G.N. Parsons. Phys Rev B 65 (2001) 035311.

15. J. Erlebacher, M.J. Aziz, E. Chason. Phys Rev Lett 84 (2000) 5800.

16 A. A. Turkin, Y. T. Pei, K .P. Shaha, C.Q.Chen, D. I. Vainshtein, J. Th. M. De Hosson, J. Appl. Phys. 105 (2009) 013523.
17 A. A. Turkin, Y. T. Pei, K .P. Shaha, C.Q.Chen, D. I. Vainshtein, J. Th. M. De Hosson, J. Appl. Phys. (2010) accepted.
18. I. Horcas, R. Fernández, J.M. Gómez-Rodríguez, J. Colchero, J. Gómez-Herrero, A.M. Baro Rev Sci Instrum 78 (2007) 013705.
19. Y.P. Zhao, G.C. GC, T.M. Lu. Characterization of amorphous and crystalline rough surface: principles and applications. London: Academic Press; 2001.
20. O. Wouters, W.P Vellinga , R. Van Tijum,J.Th.M. De Hosson. Acta Mater 53 (2005) 4043.
21. Y. Lifshitz,S.R. Kasi,J.W. Rabalais. Phys Rev Lett 62 (1989)1290.
22. D.R. McKenzie, D.A. Muller, B.A. Pailthorpe. Phys Rev Lett 67 (1991)773.
23. J. Robertson Philos Trans R Soc London A 342 (1992) 277
24.C.A. Davis, K.M. Knowles., G.A.J. Amaratunga. Surf Coat Technol 76-77 (1995) 316.
25. C.A. Davis, G.A.J. Amaratunga ,K.M. Knowles. Phys Rev Lett 80 (1998) 3280.
26. M. Natasi, J.W. Mayer, J.K. Hirvonen: 'Ion - Solid Interactions', 374; 1996, Cambridge University Press, Cambridge.
27. M. Pelliccione, T. Karabacak and T.-M. Lu, Phys. Rev. Lett. 96 (2006) 146105.
28. J. Yu, J.G. Amar, Phys. Rev. E 66 (2002) 021603.
29. L. Golubovic, Phys. Rev. Lett. 78 (1997)90.
30. J. Drotar, Y.P. Zhao, T.M. Lu, G.C. Wang, Phys. Rev. B. 62 (2000) 2118.
31. J. Xu, L. Yu, I. Kojima, J. App. Phys. 94 (2003) 6827.
32 M. Pelliccione and T.-M. Lu, Evolution of thin film morphology, Springer (2008)
33. M. Raible, S.J. Linz and P. Hanggi, Phys. Rev. E 62 (2000) 1691.
34. P. Meakin, Phys. Reports 235 (1993) 189.
35. J. Krug, Adv. in Physics 46 (1997) 139.
36. S.F. Edwards and D.R. Wilkinson, Proc. R. Soc. Lond. A 381 (1982) 17.
37. W. W. Mullins, J. Appl. Phys. 28 (1957) 333.
38. S. Majaniemi, T. Ala-Nissila, and J. Krug, Phys. Rev. B 53 (1996) 8071.
39. N.A. Marks, J. M. Bell, G. K. Pearce, D. R. McKenzie, and M. M. M. Bilek, Diamond Rel. Mater. 12 (2003) 2003.
40. F. Family, and T. Vicsek, J. Phys. A: Math. Gen. 18 (1985) L75.
41. R. P. U. Karunasiri, R. Bruinsma, and K. Rudnick, Phys. Rev. Lett. 62 (1989) 788.
42. G. S. Bales, and A. Zangwill, Phys. Rev. Lett. 63 (1989) 692.
43 C. Roland, and H. Guo, Phys. Rev. Lett. 66 (1991) 2104.
44. J. H. Yao, C. Roland, H. Guo, Phys. Rev. A 45 (1992) 3903.
45. G. S. Bales, and A. Zangwill, J. Vac. Sci. Technol. A 9 (1991) 145.
46. J. Krug, and P. Meakin, Phys. Rev. E 47 (1993) R17.
47. T. H. Vo. Thi, J-L. Rouet, P. Brault, J-M. Bauchire, S. Cordier, and C. Josserand, J. Phys. D: Appl. Phys. 41 (2008) 022003.
48. J. H. Yao, and H. Guo, Phys. Rev. E 47 (1993) 1007.
49. J. T. Drotar, Y.-P. Zhao, T.-M. Lu, and G.-C. Wang, Phys. Rev. B 62 (2000) 2118.
50. T. Karabacak, H. Guclu, and M. Yuksel, Phys. Rev. B 79 (2009) 195418.
51. A. Vickery, C. P. Jensen, F. E. Christensen, M. P. Steenstrup, and T. Schønfeldt, X-Ray Optics and Instrumentation, (2008), Article ID 792540
52. T. Ono, T. Kenmotsu, and T. Muramoto, Simulation of the Sputtering Process, in: Reactive Sputter Deposition (Eds. D. Depla, S. Mahieu), Springer Series in Materials Science, Vol. 109, Springer Berlin Heidelberg, 2008, p. 1-42.
53.W. O. Hofer, Angular, energy, and mass distribution of sputtered particles, in: Sputtering by Particle Bombardment III: Characteristics of Sputtered Particles, Technical Applications (Eds. R. Behrisch and K. Wittmaack), Topics in Appl. Physics, Vol. 64, Springer-Verlag, New York, 1991, p. 15-90.
54. H. Gnaser, Energy and Angular Distributions of Sputtered Species, in: Sputtering by Particle Bombardment (Eds. R. Behrisch, W. Eckstein), Topics Appl. Physics Vol. 110, Springer-Verlag Berlin Heidelberg, 2007, p. 231–328.
55. K. Rodelsperger, and A. Scharmann, Z. Phys. B, 28, 37 (1976).

Chapter 4
MICROSTRUCTURE AND DEFORMATION BEHAVIOR OF TiC/a-C COATINGS*

This chapter is focused on the microstructure and deformation behavior of TiC/a-C nanocomposite coatings. The microstructural evolution as a function of pulse frequency was scrutinized. The nanoscale structures together with chemical composition, especially at the growing front, have been investigated. Concurrent ion impingement to the growing coatings produces an amorphous capping layer ~ 3 nm in thickness where spatially modulated phase separation is initiated. It is shown that the modulation of multilayers, as controlled by the self-organization of nanocrystallites below the capping layer, can be tuned through the entire coating thickness. Combined nanoindentation and ex situ cross-sectional transmission electron microscopy (XTEM) investigations are carried out on TiC/a-C nanocomposite coatings, with and without multilayered structures deposited by pulse DC magnetron sputtering. It is shown that by controlling the distribution of nanocrystallites forming nanoscale multilayers, the system can be used as a "microstructural ruler" that enables distinguishing various deformation patterns which can be hardly detected otherwise in a homogenous structure. It is shown that rearrangement of TiC nanocrystallites and displacement of a-C matrix occurs at length scales from tens of nanometer down to 1 nm. At submicrometer scale, homogeneous nucleation of multiple shear bands has been observed within the nanocomposites. The multilayered structure in the TiC/a-C nanocomposite coating contributes to an enhanced toughness.

---

* This chapter is published in the following papers:
1. C.Q. Chen, Y.T. Pei, K.P. Shaha, J.Th.M. De Hosson. Tunable self-organization of nanocomposite multilayers. *Appl. Phys. Lett.* 96 (2010), 073103.
2. C.Q. Chen, Y.T. Pei, K.P. Shaha, J.Th.M. De Hosson. Nanoscale deformation mechanism of TiC/a-C nanocomposite coatings. *J. Appl. Phys.*, 105 (2009), 114314.
3. C.Q. Chen, Y.T. Pei, K.P. Shaha, J.Th.M. De Hosson. Nanoscale deformation in TiC/a-C multilayered nanocomposite coatings. *Appl. Phys. Lett.* 92 (2008), 241913.

4.1 Introduction

In nanocomposite coatings composed of hard nanograins and a compliant matrix, two different designs have been recently put into practice in thin coating applications, namely superhard and supertough nanocomposite coatings.[1] The concept of superhard nanocomposite coatings lies on the suppression of dislocation operation by using 3-5 nm small grains and inducing grain incoherence strains with <1 nm thin matrix for grain separation. On the other hand, nanocomposite coatings generate a high density of interphase interfaces that assist in crack deflection and termination of crack propagation. Especially, the introduction of amorphous matrix facilitates grain sliding that releases the strain energy stored. Based on these toughening mechanisms, the concept of supertough nanocomposite coatings has been proposed. It has been suggested for super toughness a coating structure consisting of 10-20 nm nanocrystalline grains separated by 2-10 nm amorphous matrix.[2] Furthermore, the ductility and therefore the toughness will be enhanced provided the particle size of the nanocrystallites becomes of approximately the same size as the separation.[3] To manipulate the size and separation of TiC nanocrystallites, a possible approach is to tailor a multilayered structure into a nanocomposite coating, such that the nanocrystallite containing sub-layers are separated by the matrix sub-layers of desired thickness via composition fluctuation during deposition. Through such an integrated multilayer-composite structure, the size and separation of TiC nano-particles can be well controlled independently, which is not possible in a homogeneous nanocomposite coating.

Recently self-assembling has been realized and utilized in the growth of thin coatings with nanoscale ordered structures, like superlattices or multilayers in metal-metal[4,5] and metal-carbon systems.[6-10] Despite the experimental accomplishments, understanding of the physical mechanism and the driving force is still rather limited, partially due to the fact that a high spatial resolution examination of the structures were not performed. Self-assembling is often associated with surface irradiation,[5,9,10] high temperature,[10] metal species and content,[8,10] deposition rate,[7] etc. However, the atomic underpinning mechanism is still rather obscure. Also, the self-organized nanocomposite multilayers reported in literature generally degrade fast and the modulation is lost after growth of tens of nanometers.[6-10] Further, the driving force of self-organization, i.e. whether it refers to nucleation and growth or spinodal decomposition, is still under debate.[8,10]

Also, despite the importance and extensive study on amorphous and nanocomposite carbon systems, several aspects regarding the deformation and fracture behavior at the nanoscale, and the underpinning physical mechanisms are not yet understood. Recently several molecular dynamics (MD) simulations have been reported on the deformation and fracture mechanism of DLC and DLC-based nanocomposite at atomic scale[11-14].

However, direct experimental validations of the theoretical models are not available. High resolution transmission electron microscopy (HRTEM) is the most direct method to observe the effects of a mechanical response at nanometer scales. Nevertheless, it experiences a practical difficulty in the examination of DLC or DLC based nanocomposites due to the amorphous nature of DLC. In crystalline materials, HRTEM makes use of the fact that defects create local discontinuity in the otherwise perfect periodicity of the crystalline structure. Thus, it is the presence of a lattice, which acts as an intrinsic reference, that allows the detailed characterization of various defects like line defects (dislocations), and planar defects (homophase and heterophase interfaces), and to investigate their evolution during or after deformation. However, in pure DLC or a homogeneous DLC-based nanocomposite the amorphousness and homogenous state at various length scales make tracing of defects, and evolution of nanostructure, during and after deformation quite elusive. In this chapter, it is shown that, by controlling the distribution of nanocrystallites (NCs), so that they form nanoscale multilayers, the NCs can serve as perfect markers for distinguishing various deformation patterns that can hardly be detected in a homogenous structure. Multilayers with bilayer thicknesses down to <10 nm and interparticle distance of ~1 nm provides extremely fine interior markers for high resolution observations.

In this chapter, the first section describes a tunable and sustainable growth of self-organized nanocomposite multilayers by surface ion-impingement during p-DC sputtering of carbon and Ti. The evolution of the nanostructure with growth (thickness) is investigated in detail by combined atomic scale HR-XTEM (high resolution cross-sectional transmission electron microscopy) and energy filtered XTEM, which is capable of resolving atomic scale chemical information. The second section concentrates on visualizing nanoscale deformation mechanisms of the nanocomposite thin coating under depth sensing indentation. XTEM investigation of individual indents on a thin coating is a nontrivial problem, due to the difficulty of precisely preparing a cross-section specimen out of the microscaled indent. The nanoscale deformation processes are first visualized in a typical nanolayered nanocomposite thin coating. Thereafter, investigations are extended to nanocomposites of various structural configurations, with and without multilayer and having controlled TiC nanocrystallites size and distribution. An interparticle deformation process involving rearrangement of TiC nanocrystallites and displacement of a-C matrix is demonstrated to dominate the deformation mechanism at length scales ranging from tens of nm down to 1 nm. The mechanism and toughening effect of this interparticle process are discussed. This process provides a link between the submicron deformation, which can be readily experimentally revealed, and the atomic scale process as recently modeled by molecular dynamics simulations.

4.2 Experimental

The TiC/a-C nanocomposite thin coatings were deposited on <001> oriented Si wafer by simultaneous non-reactive DC sputtering of Ti and pulsed-DC sputtering of graphite targets at different pulse frequency viz. 100, 250 and 350 kHz. A TiCr interlayer was deposited between the substrate and the top thin coating to improve adhesion. A substrate bias of 40 V was used for all the depositions. The substrate rotational speed was kept at 3 rpm during deposition. Structure observations were performed in a JEOL 2010FEG high resolution TEM operating at 200 kV and having a Gatan energy filtering system. Depth sensing indentation with a Berkovich diamond indenter was employed to measure the indentation hardness and modulus of the nanocomposite thin coatings and to study their deformation mechanism. The indentations were performed with a MTS Nanoindenter XP® system. TEM observations of the nanostructure of the top layer and interlayer were carried out before and after indentation by TEM. Si wafer was used as a model substrate that is expected to decrease the influence of substrate because of its high modulus and hardness.[15] For post-indentation XTEM investigation, a special design making an array of nanoindentations (up to 400) was used and followed by classic cross-section TEM specimen preparation. This method of XTEM specimen preparation may produce extremely thin specimen for atomic scale high resolution examination of a particular indent or even a specific area within the indent, due to the feasibility of intentional interruption and resumption of the ion beam thinning process. Two indented samples were glued face-to-face, followed by cutting, grinding, dimpling, and finally ion thinned to electron transparent thickness using a Gatan PIPS operated at 3.5 kV.

4.3 Results and discussion

4.3.1 Evolution of nanostructure as a function of pulse frequency

In this section, the evolution of the nanostructure as a function of pulse frequency for p-DC sputtered TiC/a-C coatings is described in detail by combined atomic scale HR-XTEM (high resolution cross-sectional transmission electron microscopy) and energy filtered XTEM, which is capable of resolving atomic scale chemical information. The deposition and structural parameters of the TiC/a-C nanocomposite coatings studied are listed in Table 4.1. The coatings are termed by a combination of pulse frequency applied to the graphite targets and substrate bias voltage. With increasing the p-DC frequency, the sputtering yield of graphite targets decreases so that the content of carbon in the coatings decreases even though the sputtering currents applied to the targets were kept unchanged for the first three coatings. On the other hand, increasing substrate bias voltage enhances the re-sputtering of carbon atoms from the coating, also leading to the reduction of carbon content.

Table 4.1Chemical composition of TiC/a-C coatings named with p-DC pulse frequency and substrate bias voltage, size d of TiC nanocrystallites, wavelength Λ of the multilayers, revolutions n needed to yield a bilayer, surface roughness w, and impingement enhanced diffusion coefficient $\bar{D}^*$. Sputtering currents applied to Ti and graphite targets are I_{Ti}=0.35 A and I_C =1.5 A respectively, except the I_{Ti}=0.55A for the last coating for comparison.

Coating code	Composition (at%)			Λ (nm)	d (nm)	n	w (nm)	$\bar{D}^*$ ($\times 10^{-19}$ m^2s^{-1})
	C	Ti	O					
100k40V	89.8	9.7	0.5	Homogeneous	~2	-	4.6	-
250k40V	86.6	12.9	0.5	6.7	3-5	3.7	0.3	-1.5
350k40V	80.1	19.3	0.6	9.8	4-6	6	0.28	-2.0
350k100V	75.2	23.9	0.9	14.2	3-7	11	0.23	-2.3
350k40V0.55	66.3	32.7	1.0	Weak multilayer	3-7	-	0.25	-

Accordingly, the composition of the nanocomposite coatings covers a wide range of interest. The XTEM of the nanostructures of the coatings is shown in Figure 4.1.

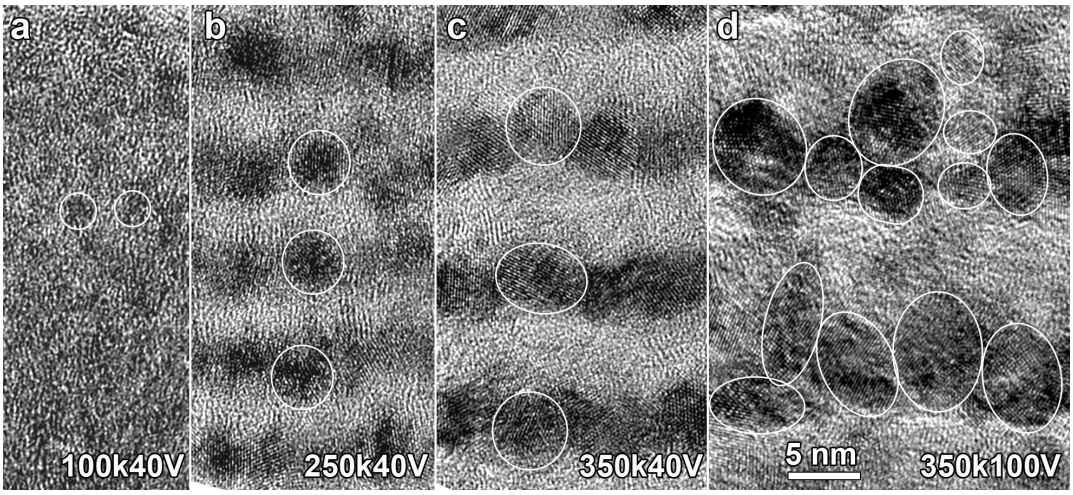

Figure 4.1 HR-XTEM images showing the structure evolution of p-DC deposited TiC/a-C coating with increasing pulse frequency and substrate bias. Circles in white color mark TiC nanocrystallites.

The coating deposited at 100 kHz showed a seemingly homogeneous nanocomposite structure with weak contrast of crystalline domains; while those deposited at pulse frequencies higher than 250 kHz possessed multilayered structures, with tunable bilayer thickness that increased with increasing pulse frequency and substrate bias voltage. The multilayers were composed of alternating Ti-rich and C-rich layers, with the darker ones containing aligned TiC nanocrystallites separated by a-C boundaries, while the bright ones being C-rich layer mainly composed of a-C. From a closer examination of the nanostructures it turns out that the formation of these multilayers was a spontaneously assembling process via phase separation, rather than a direct result of the sequential

deposition of Ti and C species, as the formation of a bilayer generally involved more than one substrate revolutions, e.g. 3.7, 6 and 11 revolutions for the coatings 250k40V, 350k40V and 350k100V, respectively. Moreover, the number of revolutions yielding one bilayer increased with increasing pulse frequency and/or substrate bias voltage. Consequently, the bilayer thickness of the three coatings was 6.7, 9.8 and 14.2 nm, respectively, despite the slight decrease of deposition rate. Presumably this trend is associated with the intensified concurrent Ar ions impingement at the growing surface at higher pulse frequency and substrate bias voltage. A detailed evaluation of the energy distribution of sputtering ions showed that the energy flux coincides well with the trend of bilayer thickness, as illustrated by Figure 4.2.

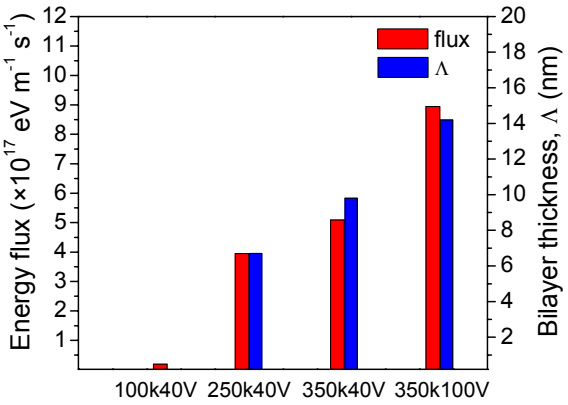

Figure 4.2 Diagram showing the trend of energy flux and bilayer thickness (except 100k40V where no layers form) at different deposition parameters with the inset showing the energy distribution of impinging ions at various deposition frequencies.

It has been revealed that the coating 100k40V exhibited a homogeneous nanocomposite structure composed of ~2 nm TiC nanocrystallites (NCs) embedded in brighter C-rich matrix. By increasing the pulse frequency and thus the energy of ion impingement, the deposited atoms were able to diffuse over a larger depth, which facilitated local enrichment of Ti atoms and thus the subsequent formation of larger TiC NCs. These NCs were aligned parallel to the surface, giving rise to a multilayered structure. In the coating 250k40V, each Ti-rich sublayer contained one monolayer of TiC NCs of 3-5 nm diameter. The size of TiC NCs increased to 4-6 nm with the frequency increasing to 350k. The further intensified ion impingement by applying higher bias voltage of 100V produced a stack of NCs in an individual Ti-rich layer in the coating 350k/100V, in addition to the larger wavelength. At the same time, the size of the nanocrystallites was getting more scattered within a range of 3-7 nm. It is also noticed that in the coatings 250k40V and 350k40V the C-on-Ti and Ti-on-C interfaces showed equally well defined contrast. However, in the 350k100V coating, the Ti-on-C interface appeared rather sharp, but the C-on-Ti interface was relatively diffuse, as to be discussed

later. The diffuseness was likely related to the random growth of TiC NCs and subsequent random nucleation and growth of new (secondary) NCs that stack on the preformed (primary) NCs.

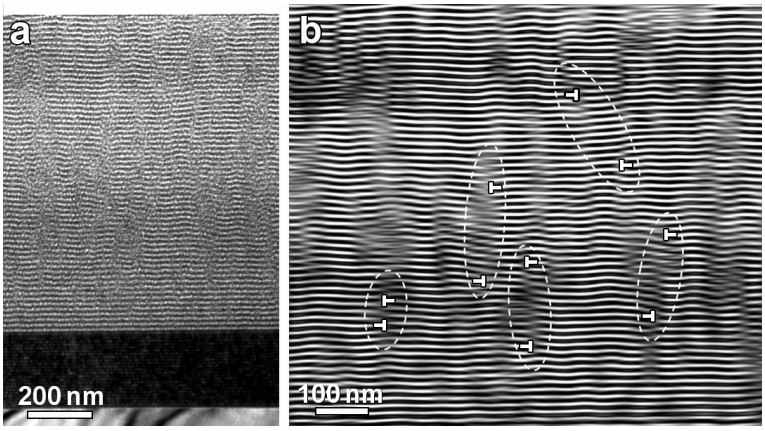

Figure 4.3 (a) XTEM images showing the evolution of multilayers with growing thickness in the coating 350k100V, with (b) filtered inverse FFT image highlighting multilayer waviness, which shows similarity with edge dislocations induced distortion in lattice planes in a crystal, with the maximum fluctuation smaller than a period.

In contrast to the multilayers deposited layer by layer, whose waviness is governed by the surface roughness, the waviness of the multilayers presenting the self-organized distribution of TiC NCs was decoupled from the surface roughness and was more complex. In fact, this is also one of the major difficulties in maintaining the growth stability of the self-organized multilayers, and the reason why the modulation reported in literature was generally lost after tens of nanometers growth. However, the self-organized multilayers reported here were rather stable during growth. The XTEM micrograph, in Figure 4.3a, shows the overall evolution of the multilayered structure of the coating 350k100V. Clearly, the waviness increased slowly at the early stage (~10 periods), but subsequently became saturated and stable. It is concluded that the intensive ion impingement used results in a continuously low or even decreasing roughness of the growing surface with deposition time, which ensured the self-assemble process and multilayered structure throughout the entire thickness of the coatings. The waviness of the nanocomposite multilayers is highlighted in Figure 4.3b by an inverse filtered FFT treatment. Interestingly, the fluctuation of the multilayers, if deemed as crystallographical planes, resembles the distortion introduced by an edge dislocation. These “dislocation”-like defects introduce locally an extra layer of TiC NCs, resulting in distortion of the multilayers. The “dislocations” generally appear as dipoles, i.e. two dislocations with deferent signs close to each other locating at a vertical sliding plane. They cancel the effect of each other, and as a result, the fluctuation initiated at the lower “dislocation” is flattened out by the upper one. The “dislocation-glide-plane” in-between the two dislocations appears as a stripe-like region with a locally diffuse appearance. HRTEM

examination of the stripe-like regions (not shown) revealed that the diffuse multilayered configuration was related to an increasing local disorder of TiC nanocrystallites, i.e. imperfections in the self-organization.

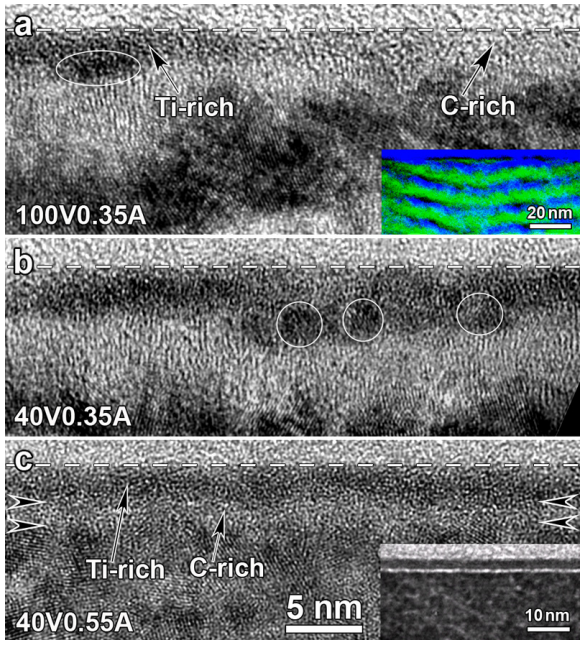

Figure 4.4 HR-XTEM observations at the growing fronts of coatings deposited at 350kHz frequency, with the current to Ti target and substrate bias noted in the images. A dashed line indicates the surface of the coatings. Insets of (a) and (c) are energy filtered compositional map (Ti green, C blue) at the growing front and zoom out of (c), respectively.

A detailed HRTEM examination of the growing front revealed a very thin (~3 nm) capping layer or surface layer, which was invariably amorphous and covered the coating. It is noticed that for a multilayered coating the surface layer may contain alternating C-rich and Ti-rich segments as confirmed by the energy filtering TEM in Figure 4.4a, while the C-rich domains were not clearly distinguishable from the underneath a-C sublayer. However, this surface layer could be clearly observed in the coating 350k40V0.55 shown in Figure 4.4c, which was composed of monolithic structure of TiC nanograins and a-C boundaries due to the largely increased Ti content. The capping layer is clearly observable in either the high-resolution or the bright field (inset) micrographs in Figure 4.4c. The existence and amorphous nature of the surface layer were mainly attributed to the greatly intensified concurrent impingement by p-DC sputtering at high frequencies. It is also a direct evidence of impingement induced subplantation model for surface smoothing in diamond-like-carbon.[16] The surface layer was supposed to be sp^2 bonded carbon of a relatively low density,[16,17] but could not be imaged in pure a-C due to the lack of contrast. The wavelength that can be tuned via the p-DC sputtering process was associated with an enhanced interdiffusion of C and Ti species caused by the concurrent ion impingement, a phenomenon noticed as early as in 1970-80s.[18,19] It was suggested

that the high density of defects may be responsible for the enhanced diffusivity under intensified ion impingement. The impingement-enhanced diffusion coefficient $D^*(z)$ decays exponentially with depth z and can be expressed as:[19]

$$D^*(z) = D^*(0)\exp\left(\frac{-z}{L_d}\right) \qquad (1)$$

where $D^*(0)$ is the enhanced diffusion coefficient at the surface $(z=0)$, and L_d represents a characteristic diffusion length of the ion-impingement-produced defects and can be assumed here as the wavelength Λ. For the present case, $D^*(0)$ was associated with the experimentally measured energy flux $\boldsymbol{I}$ illustrated in Figure 4.2 and can be tentatively expressed in the form of:

$$D^*(0) = D_{th}\exp\left(\frac{\alpha I}{kT}\right) = D_0\exp\left(-\frac{Q-\alpha I}{kT}\right) \qquad (2)$$

with D_{th} representing the thermal diffusion coefficient of the phase separation given by the pre-exponential factor D_0 and the activation energy Q, $\exp(\alpha I/kT)$ being an enhancement factor and α is a positive constant. Equation (2) can be interpreted as an effective coefficient of thermal diffusion with the activation energy decreasing to $(Q-\alpha I)$ linearly with the energy flux. Therefore Eqs. (1) and (2) provide a correlation between the bilayer thickness and the intensity of ion impingement as shown in Figure 4.2.

The spatial coordinate z in Eq. (1) is related to the deposition rate υ and deposition time t by $z=\upsilon t$. For a rough estimate, the diffusion length can be approximated by $L_d = 2\sqrt{\bar{D}^* t_\Lambda}$, where t_Λ is the deposition time for one bilayer and $\bar{D}^*$ the average impingement-enhanced interdiffusivity. By assuming the bilayer thickness as a measure of L_d, $\bar{D}^*$ is calculated for the coatings as listed in Table 4.1, and the minus sign represents the up-hill nature of the interdiffusion.

The C-rich and Ti-rich segments in the surface layer indicated that the local composition of the layer was markedly influenced by the underneath wavy sublayers via the vertical diffusion process. For example, on the right side of Figure 4.4a the capping layer was C-rich since the Ti atoms could travel a short distance downwards to the underneath Ti-rich layer. However, on the left side Ti atoms could not travel to the underneath Ti-rich layer due to the larger distance, consequently Ti is locally enriched and a new TiC nucleus marked by a circle forms at the bottom of the amorphous capping layer. This process initiated the formation of a new Ti-rich sublayer. While the capping layer was "flat", the waviness of the multilayers was thus restricted by the diffusion length (wavelength). Once the amplitude of local waviness of the Ti-rich layer

underneath the capping layer is larger than the diffusion length, an extra layer ("dislocation") can be introduced, which causes local disordered arrangement of TiC NCs on the slip plane of the “dislocations”.

One final point to be considered is the driving force of phases separation, i.e. nucleation and growth versus spinodal decomposition. In one of the previous reports about a Ti-C coating containing 5 at.% Ti the Ti-rich layers was found to be fully amorphous,[8] which definitely points to spinodal decomposition. We did not observe a fully amorphous Ti-rich layer here due to the relatively high Ti-concentrations. Nevertheless, the wide size distribution of TiC NCs in the coating 350k100V (Figure 4.1d) and especially the fine TiC NCs formed right at the bottom of the amorphous capping layer (Figure 4.4a and b) indicate nucleation and growth mechanism. It should be stressed that the up-hill interdiffusion of Ti and C atoms driven by the intensified concurrent ion impingement lays the basis for the phase separation and multilayer formation.

4.3.2 Deformation behavior of TiC/a-C coatings

4.3.2.1 Nanostructure and mechanical properties

In this section, the deformation behavior of nanocomposite/multilayer TiC/a-C coatings is discussed. TiC/a-C nanocomposite coatings were obtained by p-DC sputtering of graphite targets at 350 kHz, to enhance the impingement at the growing interface for producing the multilayers, as discussed in above section. The properties are listed in Table 4.2, with the coating having three different Ti contents named according to the atomic ratio of C and Ti elements. With the optimized deposition parameters, nanoscale multilayers were successfully produced in the thin coatings $C_{85}Ti_{15}$ and $C_{73}Ti_{27}$ with well aligned TiC nanocrystallites.

Table 4.2 Chemical composition, coating thickness t, wavelength Λ of multilayers, volume fraction V_F and size d of TiC particles, and mechanical properties including hardness (H), Young’s modulus (E) (H and E are derived from the data with displacement up to 100 nm indentation, i.e. < 1/10 of the coating thicknesses), as well as the ratio of residual to total indentation depth d_r/d_t.

Thin coating	Composition (at%)			t (μm)	Λ (nm)	VF (%)	d (nm)	H (GPa)	E (GPa)	H/E	H^3/E^2 (GPa)	dr/dt (%)
	C	Ti	O									
C85Ti15	84.8	14.9	0.3	1.30	27.4	2-4	7.5	19.1	195.2	0.098	0.183	53.8
C73Ti27	71.7	27.1	1.2	1.29	52.4	3-5	11.4	21.1	207.9	0.101	0.217	51.8
C65Ti35	64.0	35.0	1.0	1.50	69.1	3-5	Uniform	27.5	262.5	0.105	0.302	48.5

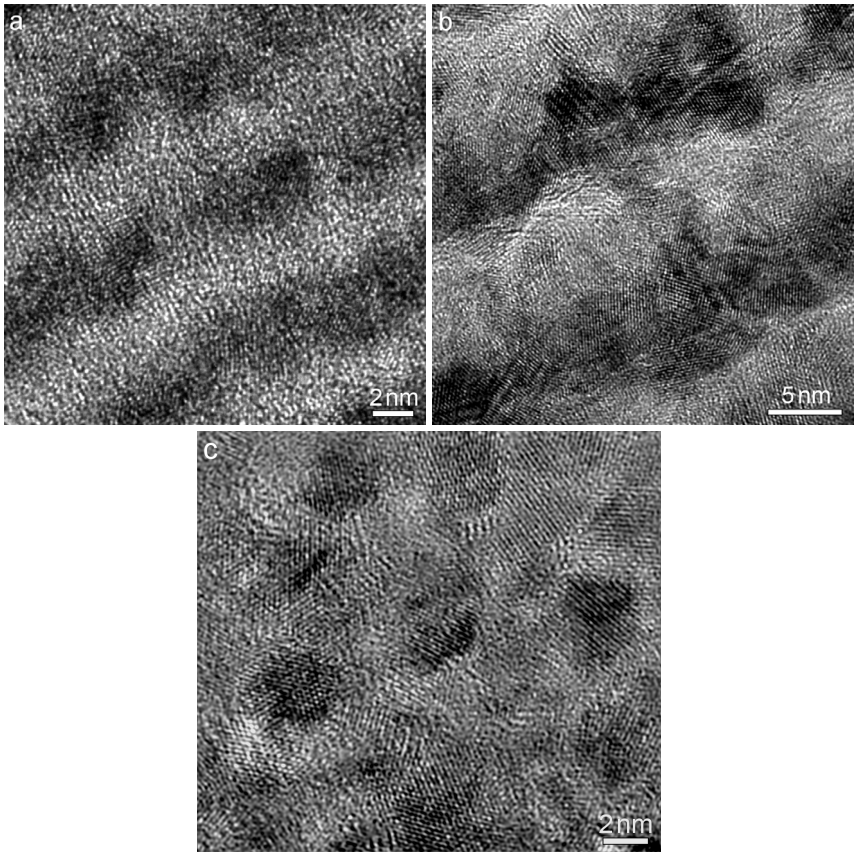

Figure 4.5 High resolution XTEM micrographs showing the microstructure evolution of the coatings with increasing Ti content: multilayered structure of the coating $C_{85}Ti_{15}$ (a) and $C_{73}Ti_{27}$ (b), and homogeneous nanostructure of the coating $C_{65}Ti_{35}$ (c).

As shown in Figure 4.5a, the multilayers in the thin coating $C_{85}Ti_{15}$ consist of amorphous carbon sublayers (bright lamellae) and Ti-rich sublayers (darker lamellae) composed of aligned discrete TiC nanocrystallites. The microstructure parameters for all the thin coatings are listed in Table 4.2. The bilayer thickness and the diameter of TiC nanocrystallites increased with increasing Ti contents. The multilayered structure was formed through a self-organization process governed by the interdiffusion of C and Ti, with the bilayer thickness, the size of TiC nanocrystallites, and the growth front roughness controllable with the intensity of concurrent ion bombardment but independent of the substrate rotation speed. The detailed mechanism is discussed in chapter 3. By increasing Ti content to $C_{65}Ti_{35}$, the whole system evolved into uniform nanocomposite of homogeneously distributed TiC nanoparticles separated by very thin a-C tissue phase (matrix), as shown in Figure 4.5c.

The indentation hardness of the coatings, listed in Table 4.2, showed a monotonic increase with Ti contents: from 19 GPa for the thin coating $C_{85}Ti_{15}$ to 21 GPa for the thin coating $C_{73}Ti_{27}$ and then rapidly rising to 27 GPa for the thin coating $C_{65}Ti_{35}$. The Young's modulus showed a similar tendency of increase. The other two parameters often

used to predict the wear resistance of a thin coating, i.e. the ratios H/E and H^3/E^2, are also listed in Table 4.2. The ratio H^3/E^2 is considered as an indicator of the resistance to plastic deformation (resilience) in loaded contact while H/E ratio is known as the elasticity index[20]. These two ratios increased with increasing Ti content, suggesting an enhanced deformation and wear resistance of the nanocomposite thin coatings.

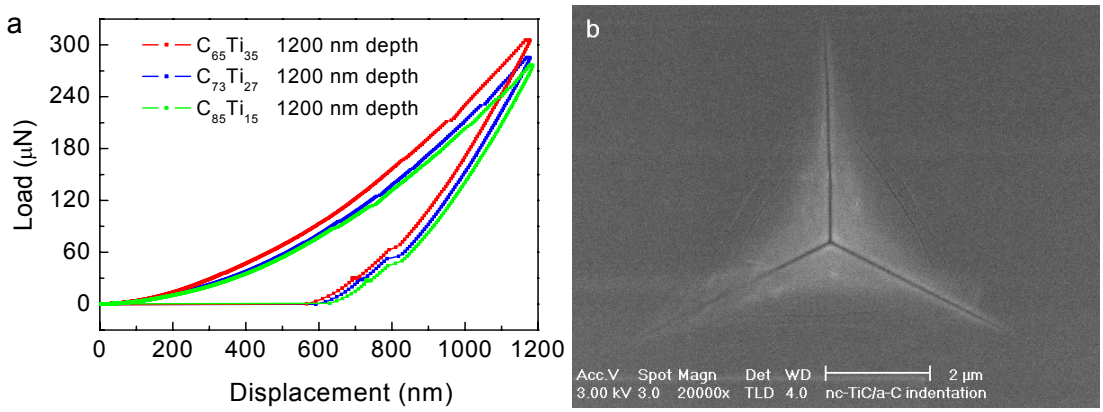

Figure 4.6 (a) Indentation load responses of three nanocomposites coatings, indented to a maximum depth of 1200 nm and (b) SEM top view of an indent revealing tiny side cracks in the coating $C_{65}Ti_{35}$.

Figure 4.6a shows indentation load responses of the three thin coatings indented to a maximum depth of 1200 nm, which almost penetrated through the entire thin coating thickness. The load-depth curves showed a weak discontinuity at large indentation depths, which could be related to the phase transformation inside the Si substrate as to be discussed later. SEM top views of the impressions confirmed no radial cracks formed along the indenter corners. Closer examination reveals only a couple of tiny and discontinuous side cracks located at the border of the impressions due to high tensile strain there, which became increasingly noticeable with increasing Ti content but were still small surface cracks even in the coating $C_{65}Ti_{35}$ (Figure 4.6b) as to be further discussed. Plastic deformation in the indented thin coatings may be estimated by the ratio of residual indentation depth to the total indentation depth d_r/d_t, derived from the load response curves, as listed in Table 4.2. The obtained values ranging from 48.5-53.8% at 1200 nm indentation depth were reasonably high, which can be considered as an indication of a tough character of the nanocomposites[21].

4.3.2.2 Visualization of deformation processes from micro- down to nano- scale

Coating $C_{73}Ti_{27}$: shear delocalization and nanocrystallites rearrangement:

To make use of well aligned nanocrystallites as nano-markers for the observation of nanoscale deformation process, the nanolayered coating $C_{73}Ti_{27}$ was first examined. Deformation behaviors were examined at the indentation depth of 1000 nm and 1200 nm,

close to the thickness of the top-layer and the entire thin coating, respectively. It revealed information of the deformation mechanism in the nanocomposite especially near the top layer-interlayer interface where major shear processes transfer from the interlayer to the top layer with increasing indentation depth. At both indentation depths, XTEM observations revealed that no detectable cracks or delamination were formed at various interfaces.

Figure 4.7 shows the deformation morphologies of a 1000 nm deep indent in the thin coating $C_{73}Ti_{27}$. It can be seen that the interlayer already showed significant plastic deformation to accommodate externally applied strain. The dark field image of the deformed interlayer in Figure 4.7c revealed clearly two dominant and highly localized shear processes appearing symmetrically at either side of the indent, which will be further discussed later.

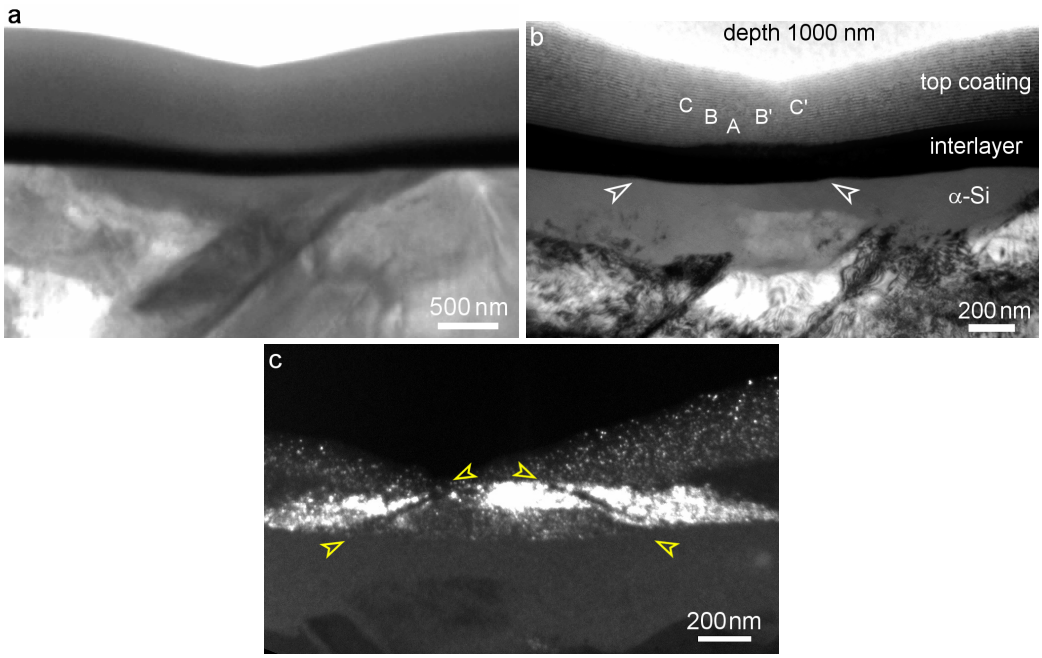

Figure 4.7 XTEM micrographs showing a 1000 nm deep indent in the coating $C_{73}Ti_{27}$: (a) overall morphology, (b) magnified micrograph taken after further ion-thinning (part of the top coating removed) revealing localized plastic deformation indicated by arrows; (c) dark field image taken after ever further ion-thinning highlighting the intense shear bands in the interlayer indicated with arrows.

Bright field TEM micrographs at moderate magnifications revealed that one of the common deformation morphologies of the indented top layer was the permanent bending of the sublayers following the indenter tip geometry, which was necessarily accompanied by an in-plane extension (Figure 4.7b). At the same time, a resulting reduction of the layer spacing up to ~50% is observed underneath the indenter, which was consistent with the ratio of residual indentation depth to the total indentation depth listed in Table 4.2. An

interesting feature, revealed by closer observations, was the numerous shear bands inclined at an angle of about 60° to the substrate interface and distributed symmetrically on both sides of the impression (Figure 4.8).

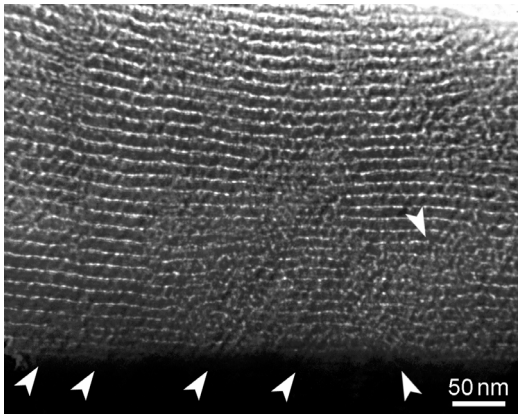

Figure 4.8 Bright field XTEM image at a modest magnification showing multiple short-range shear processes within an impression of 1000 nm depth in the coating $C_{73}Ti_{27}$.

High shear deformation in an indentation is common due to the huge strain gradient, the intrinsic nature of nanoindentation. What is interesting is that many homogeneously distributed, rather than a few predominant and highly localized shear bands were observed, the latter being the common situation in bulk amorphous materials. In addition, these multiple shear bands were of short range characters, namely propagating only several nanolayers rather than crossing the entire cross section of a thin coating as shown in Figure 4.8.

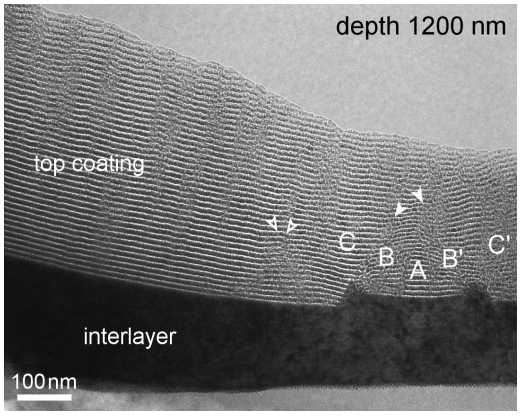

Figure 4.9 Cross-sectional morphology of a 1200 nm deep indent in the coating $C_{73}Ti_{27}$, with solid arrows indicating the central major shear bands and open arrows pointing to the side major shear bands.

At 1200 nm indentation depth, the nanocomposite coating showed much enhanced plastic deformation especially near the interlayer, with several highly localized major shear bands distributed symmetrically on both sides of the indent. The deformation morphology is shown in Figure 4.9, while a schematic illustration representing the

microscale deformation features as well as the nanoscale deformation processes, visualized subsequently with high resolution XTEM investigations, is displayed in Figure 4.10. In addition to the two central primary shear bands, several new (secondary) shear bands formed. The two central bands initiated from the two sharp wedges at the top side of the interlayer, which arise most likely from the lattice dislocation sliding along the $\{10\bar{1}0\}<1\bar{2}10>$ slip system in the interlayer.

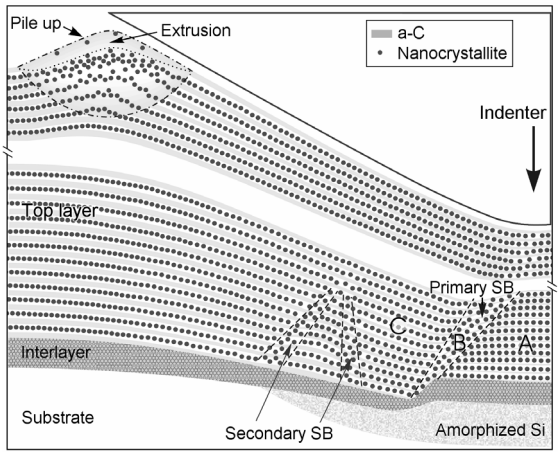

Figure 4.10 Schematic illustration of submicroscale deformation morphologies and nanoscale deformation mechanism of indented multilayered nanocomposite coatings: The microscale features, like multilayer densification at the center, primary and secondary shear bands (SBs) at either side of the indent, pile up (unique for $C_{85}Ti_{15}$) at the edge, are linked to nanoscale interparticle processes, including reordering of nanocrystallites and extensive relative sliding in the nanocomposite, which are visualized by high resolution XTEM observation with the help of well aligned nanocrystallites. The multiple short-range shear bands shown in Figure 4.8 are excluded for better view.

Interestingly, the abrupt shear deformation was gradually weakened by the nanocomposite multilayers after it transferred through the interlayer/toplayer interface. The two central shear bands in the top layer carry the highest shear strain $\gamma = s/w$ at the interface, where they have the highest shear displacement s (height of the wedge), and the minimum width w. After crossing the interface, the abrupt shear band expanded gradually to a certain width (up to ~50 nm), and the shear displacement s faded off gradually after propagating not more than 150 nm into the top layer, clearly demonstrating a shear delocalization effect of the multilayered nanocomposite (see the schematic in Figure 4.10). According to the local deformation morphologies and shear/normal strain, resolved with the help of the layered nanomarkers, an impression of the multilayered nanocomposite can be roughly divided into several regions as illustrated in Figure 4.7b, 4.9 and 4.10. The regions A, C and C' are dominated by normal strain and primarily characterized by layer densification, while regions B and B' are featured by intense shear strain.

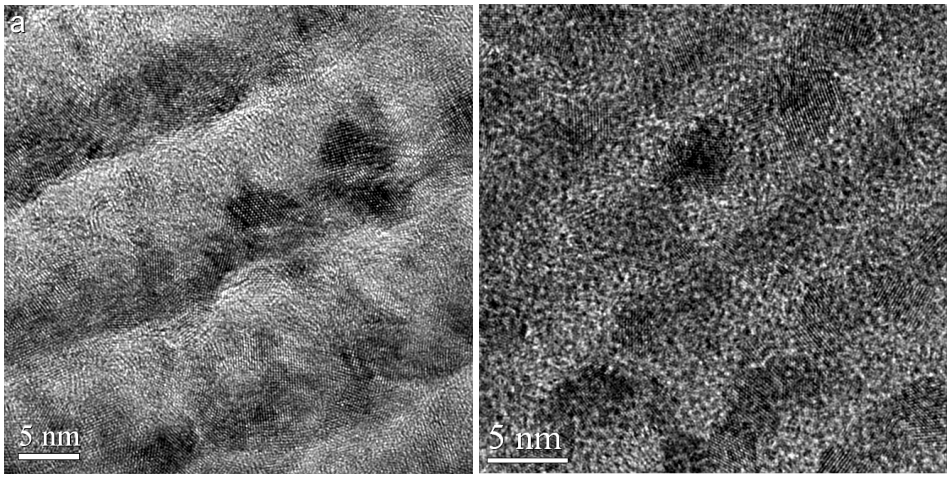

Figure 4.11 Comparison of the nanostructure of the coating $C_{73}Ti_{27}$ (a) before and (b) after indentation showing densified wavelength of the multilayers in the region "A" and rearrangement of the nanocrystallites in individual Ti-rich sublayers from more than 1 monolayer into a monolayer.

Figure 4.11 is a comparison between the undeformed and deformed nanostructures taken from the region A. In the original (undeformed) multilayered nanocomposite (Figure 4.11a), each Ti-rich sublayer contained more than one monolayer of TiC nanocrystallites such that the TiC nanocrystallites near the Ti-on-C interface almost touched each other, but those near the C-on-Ti interface were more loosely distributed in a-C phase. In correspondence with the compressed wavelength of the multilayers after indentation, the particles spacing between two adjacent Ti-rich sublayers in the region A (see Figure 4.6b and 4.9b) was decreased noticeably (Figure 4.11b and the schematic in Figure 4.10). That is to say, the in-plane extrusion and densification of the a-C sublayers were mainly the result of the severe indentation. In addition, the configuration of the nanoparticles in the Ti-rich sublayers also changed by means of remarkable displacements and rearrangements. Each Ti-rich sublayer after indentation was composed of a monolayer of TiC nanocrystallites well separated by the a-C phase (Figure 4.11b). The separation was about 1-2 nm thickness, noticeably larger than that before indentation (less than 1 nm). This kind of reconfiguration of the nanoparticles can happen only when a remarkable sliding between TiC nanocrystallites is accompanied with significantly plastic flow of the a-C matrix under the strain gradient inside the indent. The flow of the a-C matrix occurs not only in the a-C sublayers but also in the very thin intralayer regions separating the nanoparticles in the Ti-rich sublayers, resulting in an interparticle process of plastic deformation.

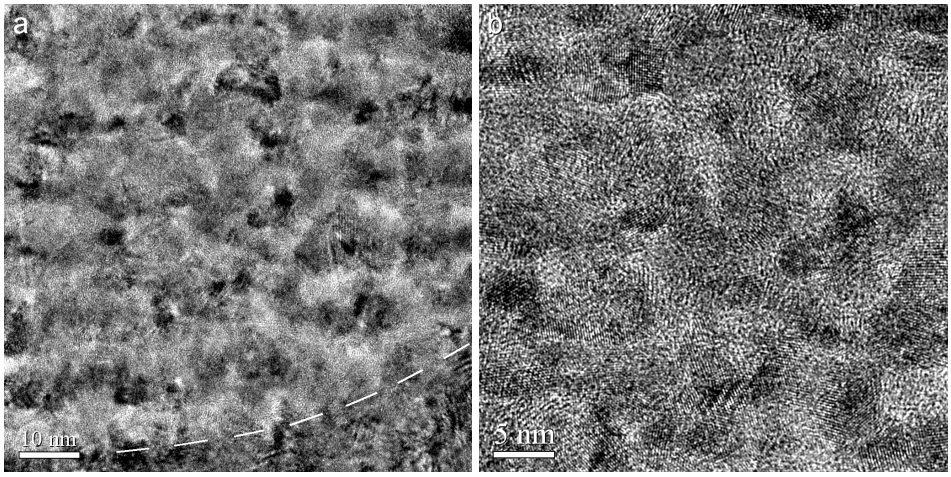

Figure 4.12 (a) Diffused multilayered structure in the region B/B' with intense shear deformation adjacent to the interlayer (note the interface bent by the intensive shear bands marked with a dashed white line); (b) completely random distribution of TiC nanocrystallites as a result of particle sliding and rearrangement

Within the regions B and B' that bear intense shear strain, as marked in Figures 4.7b, 4.9 and 4.10, the well-defined nanolayers became diffuse after the intensive shear deformation (Figure 4.12a and schematically shown in Figure 4.10). Under high magnification, these regions showed a homogeneous structure characterized by random and homogeneous distribution of the nanoparticles, with the particle size unchanged (Figure 4.12b). This indicates a relative movement of the nanoparticles following the shear deformation and mixing of the nanoparticles from adjacent Ti-rich sublayers. The random and homogeneous distribution of TiC nanocrystallites was a result of the intersection between in-plane deformation and shear banding inclined to the sublayers, as indicated in Figures 4.3b and 4.4. Plastic deformation was not observed in the individual TiC nanocrystallites due to their intrinsic high strength and suppressed dislocation activity resulting from the nanometer sizes. The deformation was mainly accommodated by an interparticle-mediated process, namely nanoparticle sliding mediated by displacement of the a-C matrix under the high strain gradient.

Coating $C_{85}Ti_{15}$: long range displacement of a-C and TiC nanoparticles:

According to the above observations, it seems reasonable to expect a considerable plastic flow of the a-C matrix surrounding the TiC particle. Consequently, such a-C mediated process may be more significant in a thin coating with a higher fraction of a-C matrix, e.g. the thin coating $C_{85}Ti_{15}$. Figure 4.13a shows the cross-sectional morphology of a 1200 nm deep indent in the thin coating $C_{85}Ti_{15}$. A clear pile up was observed at the edge of the indent. Under high resolution observation, the outmost part (about 50 nm thickness) of the pile-up region showed a very bright contrast.

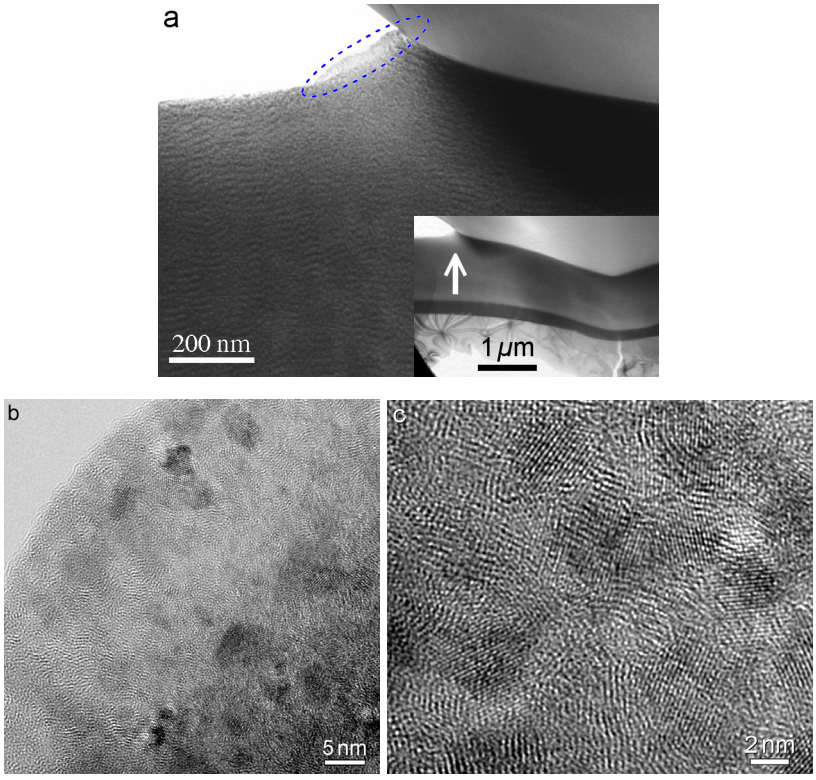

Figure 4.13 Pileup at the edge of a 1200 nm deep indent in the coating $C_{85}Ti_{15}$: (a) overview, (b) the pileup front composed mainly of a-C embedded with a very few TiC nanocrystallite and (c) densely packed nanocrystallites behind the pileup front due to the outflow of the a-C matrix.

The HRTEM micrograph revealed that this region was composed mainly of a-C embedded with very few randomly distributed TiC nanocrystallites (Figure 4.13b), indicating a preferential squeezing of the a-C matrix to the front of the pile up, as schematically shown in Figure 4.10. Consequently, the very pile up front may be better understood as an outward "extrusion" of the a-C matrix under high strain gradient underneath the indenter tip. Behind the pile up front was a region composed of dense nanoparticles, due to the flow of a-C matrix (Figure 4.13c). This process was accompanied, at the same time, by a rearrangement of the nanoparticles, as illustrated in Figure 4.10 As a result, the original multilayered structure fades off. Compared with the above observed rearrangement of the nanoparticles in the thin coating $C_{73}Ti_{27}$, the relative motion of TiC nanocrystallites and a-C matrix in the thin coating $C_{85}Ti_{15}$ occurred at much larger length scales (> 20 nm), which was attributed to the increased volumetric fraction of the moving a-C matrix. Importantly, the extensive displacement and rearrangement of TiC nanocrystallites along with the a-C matrix did not lead to distinguishable cracks or nanocavities in any way.

No cracks or voids were observed in the matrix or at the interfaces of a-C/TiC nanocrystallites in this thin coating, with close examination confirmed atomic scale

integrity at the interface. Nevertheless, within the region of dense nanoparticles experiencing extensive deformation with the outflow of a-C matrix (as shown in Figure 4.13c), direct contact between the hard particles may occur, as illustrated in Figure 4.10. In this case, very high local contact stress may be generated and as a result, local deformation of individual particles may be possible. Deformation-induced defects, if any, could possibly be retained within the individual nanoparticles after indentation.

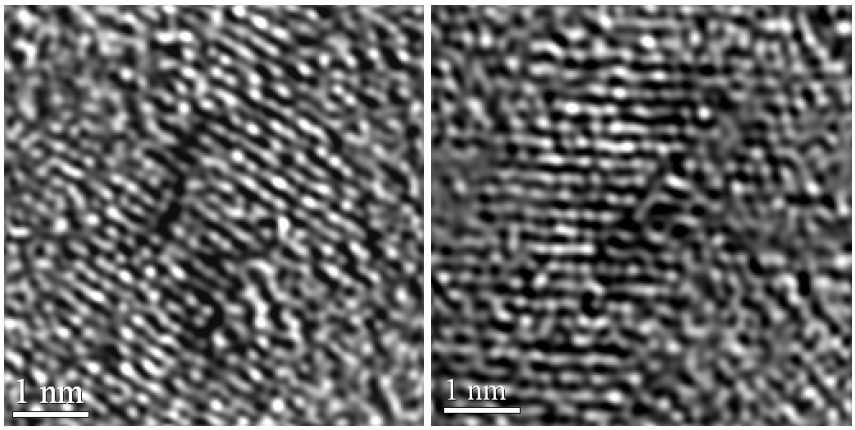

Figure 4.14 HRTEM micrographs showing lattice distortion or nanocrack-type defects within individual TiC nanocrystallites.

Figure 4.14 shows the HR-TEM micrograph of two individual nanoparticles taken from the same region as that of Figure 4.13c. Some kind of lattice voids or crack-like defects inside these nanoparticles were observed. Nevertheless, these kinds of defects were restricted within the nanocrystallites and without propagating to the phase interface or into the surrounding matrix, and thus had a limited contribution to the deformation or fracture process.

Coating $C_{65}Ti_{35}$: Advancing crack dissipated by TiC nanoparticles:

In the thin coating$C_{65}Ti_{35,}$ the whole system is composed of homogeneously distributed TiC nanoparticles instead of multilayers with thicker Ti-rich sublayers and thinner a-C layers. For such a homogeneously nanostructured system, it is hard to distinguish any deformation path/morphology regarding the interparticle deformation process due to the lack of intrinsic markers as already stressed in the introduction section. In this case, the possible cracks and their propagation behavior under indentation were studied, keeping in mind the interparticle processes revealed in the multilayered nanocomposite.

As shown in Figure 4.15a, the small surface side cracks of the indent previously revealed by SEM top view (Figure 4.6b) were observed to propagate only a very short distance (hundreds of nanometer) underneath the surface.

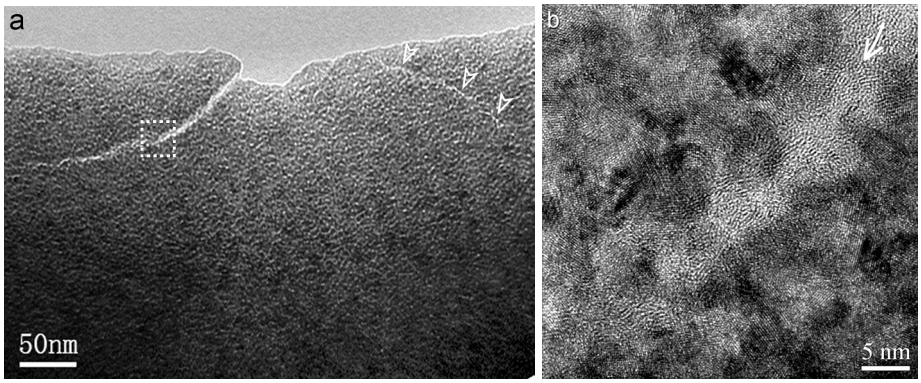

Figure 4.15 XTEM micrographs showing restrained micro-/nano-cracks in an indent in the coating $C_{65}Ti_{35}$: (a) overview and (b) magnified HR-XTEM micrograph taken from the area marked with a square box in (a).

The propagating cracks followed the a-C tissue phase in-between the TiC nanocrystallites (Figure 4.15b), and finally were halted at the nanoparticles. In addition, deflection of propagating cracks was obvious in the nanocomposite. It is very interesting that, instead of propagating continuously, the crack was halted at the TiC nanocrystallites but restarted at a region a few nanometers away from the crack tip. From the HRTEM image presented in Figure 4.15b, it seems that the crack was arrested at the left bottom by the nanoparticles and starts in a distance tens of nanometers ahead.

Under indentations up to a depth of 1200 nm that was close to penetrating the entire thin coating thickness, all three thin coatings showed excellent structural cohesion at various interfaces, without cracks, micro-voids, or delamination detected. The interlayer was found to perform very well in accommodating the plastic deformation and to keep the interface adhesion. Another factor contributing to the perfect adhesion at the substrate-thin coating interface is dislocation slip and phase transformation plasticity of the Si substrate[22,23], which was clearly observed under the applied large indentation depth even penetrating into the Si substrate. The slight pop-in and distinct pop-out appeared to be due to the slip and transformation in the silicon[22], as they were observed even for thin coatings without any cracking or delamination.

Mechanism of interparticle process and flaw tolerance at nanoscale:

One of the major phenomena observed in this work was the extensive interparticle process characterized by rearrangement of TiC nanocrystalites and remarkable a-C displacement at nanometer scale, as schematically illustrated in Figure 4.10. This a-C matrix assisted process became increasingly significant in the thin coatings of higher volumetric fraction of a-C matrix, provided that the distance between the nanocrystallites is comparable with their size[2]. Within individual TiC nanoparticles, general plastic deformation was not observed due to the intrinsic high strength of TiC and suppressed dislocation activities at nanometer size. To accommodate the interparticle process,

besides particle translation, grain (particle) rotation is considered as another favorable mechanism involved in the rearrangement of nanoparticles. Although it has not been directly distinguished with XTEM on individual nanocrystallites, due to the amorphous nature of the a-C matrix, this grain rotation mechanism has been proven to be one of the major deformation mechanisms in nanocrystalline materials[24]. Extensive displacement of a-C was observed either in the a-C sublayer separating the Ti-rich layers or the a-C tissue phase within individual Ti-rich layers. The most interesting observation was that even with extensive displacement and relative sliding under large deformation, observable cracks and cavities were successfully avoided either at the boundaries between the various layers in the multilayered structure or at the phase boundaries between TiC and a-C.

HRTEM confirmed the atomic scale integrity at the phases boundary, i.e., the interface between a-C matrix and TiC nanocrystallites, without detectable nucleation and coalescence of void-like defects (Figure 4.11b and 4.12b) even in the area experienced significant out flow of the a-C matrix (Figure 4.13c). Considering the extensive relative sliding, it seems reasonable to assume that the bonding either at the interface or within the a-C has the capability to re-establish the bond after it was broken. Recently MD simulations[12] on a-C embedded with diamond crystallites suggested the possibility of bond breaking and reattaching at the interface of a-C and hard particles during the process of relative sliding at the interface, which seems in a good agreement with our HRTEM experimental observation.

Apart from the behavior at the phases interface, atomic sliding in the a-C itself is necessary to achieve the interparticle process and large displacement of a-C (e.g. that shown in Figure 4.13b) while keeping the bonds undestroyed. The amorphous structure of DLC containing mainly sp^2 bonded carbon seems to favor the interparticle sliding and a-C displacement, which could be further improved by doping of Ti[25]. However, the atomic scale deformation process in a-C matrix related to the sp^2/sp^3 ratio has not been well understood up to now [11,12]. Microscopic quantification of the effects of sp^2 fraction in the a-C on the interparticle process is still a challenge but in the present case the sp^2 dominates over sp^3.

In a recent MD simulation[14], the amorphous based nanocomposites have been reported to exhibit a certain flaw tolerance. That is to say, fracture is a gradual process accompanied by gradual nucleation and coalescence of void-like defects, and especially, crack-like defects smaller than 40 Å have almost no effect on the fracture strength. This flaw tolerance for fracture in amorphous carbon appears to be due to its intrinsic structure disorder. Therefore, flaw tolerance may be a characteristic of disordered atomic structures at the nanoscale.

Mechanism of toughening regarding the nanoscale interparticle process:

The collective behavior of the interparticle process operating at nanometer scale has significant effect on the structural response at modest (medium) length scales, and prompts shear delocalization in nanocomposite thin coatings. The nanocomposites are composed of two kinds of phases, i.e., TiC nanocrystallites and highly disordered/amorphous a-C. The deformation behaviors of the nanocomposites are found being distinct from that of either nanocrystalline[26] or bulk amorphous materials[27], and the latter suffer highly localized shear banding often resulting in catastrophic failure.

In the nanocomposites, shear deformation occurred in the amorphous matrix can be tuned by the existence of the nanocrystallites, evolving interparticle process and assisted by the flow of a-C matrix. As a result, a large number of short-range multiple shear bands nucleate homogeneously throughout the specimen and carry uniform shear deformation. The three dimensional a-C matrix seeds the initiation of organized shear bands and confines them to small domains, i.e, the a-C sublayers and interparticle boundary regions. The nanoparticles and TiC-containing sublayers act as obstacles to restrict excessive deformation in these domains. In this way, shear deformation becomes effectively delocalized. The flaw tolerance enables the a-C matrix to sustain reasonable shear deformation without causing catastrophic failure. Even when shear bands carrying extremely high shear strains occurred in the interlayer, they were delocalized in the top layer by flowable a-C carrying TiC nanoparticles and consequently the shear strain faded away after the shear bands travel a small distance.

The toughening mechanism for the nanocomposite thin coatings is consistent with the previously proposed ideas of composite microstructure for bulk amorphous alloys[28] and recently for nanocrystalline metals[29]. Another toughening mechanism in the nanocomposite thin coating is to dissipate propagating cracks via confinement in the a-C tissue phase. Micro-openings are surfaced by nanocrystallites (Figure 4.15b) that substantially increase surface area and surface energy that has to be overcome for the crack to propagate. This was confirmed by the fact that the crack does not continuously propagate, but was repeatedly halted and restarted at an area ahead of the crack tip, as clearly indicated by the indicated individual cracks. This crack re-initiation together with the deflection effect essentially causes a reduction in the crack-driving force or stress intensity factor and consequently increases the fracture toughness. A detailed analysis on these effects based on fracture mechanic analysis can be found in refs[30,31].

4.4 Conclusion

The nanostructure of self-assembled nanocomposite multilayers that are induced by surface ion-impingement can be tailored by p-DC sputtering. The nanoscale structures together with chemical composition, especially at the growing front, have been investigated with high-resolution transmission electron microscopy. Concurrent ion impingement of growing coatings produces an amorphous capping layer 3 nm in thickness where spatially modulated phase separation is initiated. It is shown that the modulation of multilayers as controlled by the self-organization of TiC nanocrystallites below the capping layer, can be tuned through the entire coating. Well aligned nanocrystallites that form multilayers served as extremely fine intrinsic markers in XTEM to reveal the deformation process in TiC/a-C nanocomposite thin coatings subjected to nanoindentation. It is shown that by controlling the distribution of nanocrystallites forming nanoscale multilayers, the system becomes a "microstructural ruler" that is able to distinguish various deformation patterns which otherwise can be hardly detected in a homogenous structure. Interparticle processes, including rearrangement and sliding of TiC nanocrystallites with respect to the a-C matrix, were found to occur at various length scales (from 1 nm to tens of nm), assisted by the flow of the a-C matrix. Because of the nano-scaled geometric constraint, shear deformation was brought under control by multiple shear bands, with each band contributing to plastic deformation but propagating only in nanometer scales and conveying a shear strain not large enough to cause local damage. At large indentation depths, the multilayered nanocomposites delocalized abrupt shear deformation arising from the interlayer significantly. Consequently, the multilayered nanocomposite thin coatings exhibited a prominent plasticity while maintaining high hardness. In the nanocomposite thin coating without multilayer structure, the cooperative deformation of nanocrystallites was found to dissipate and deflect propagating cracks effectively. The observed interparticle deformation mechanism facilitated by the separating a-C phase and the crack dissipation effect provide useful clues for the design of nanocomposites composed of hard nanocrystallites and a compliant amorphous matrix.

References

1. A. Cavaleiro, J.Th. M. De Hosson. Nanostructured Coatings. Springer Verlag, New York, 2006.
2. A.A. Voevodin, J.S. Zabinski. Thin Solid Films 370 (2000) 223.
3 Y.T. Pei, D. Galvan, J.Th.M. De Hosson. Acta. Mater. 53 (2005) 4505.
4. I. Daruka and J. Tersoff, Phys. Rev. Lett. 95 (2005) 076102.
5. J. H. He, C. A. Carosella, G. K. Hubler, S.B. Qadri, and J. A. Sprague, Phys. Rev. Lett. 96 (2006) 056105.
6. W. Y. Wu and Y. M. Ting, Chem. Phys. Lett. 388 (2004) 312.
7. I. Gerhards, H. Stillrich, C. Ronning, H. Hofsäss, and M. Seibt, Phys. Rev. B. 70 (2004) 245418.

8. C. Corbella, B. Echebarria, L. Ramírez-Piscina, E. Pascual, J. L. Andújar, and E. Bertran, Appl. Phys. Lett. 87 (2005) 213117.
9. P. E. Hovsepian, Y. N. Kok, A. P. Ehiasarian, R. Haasch, J. G. Wen, and I. Petrov, Surf. Coat. Tech. 200 (2005) 1572.
10. G. Abrasonis, G. J. Kovács, L. Ryves, M. Krause, A. Mücklich, F. Munnik, T. W. H. Oates, M. M. M. Bilek, and W. Möller, J. Appl. Phys. 105 (2009) 083518.
11 M.G. Fyta, I.N. Remediakis, P.C. Kelires, and D.A. Papaconstantopoulos. Phys. Rev. Lett. 96, 185503 (2006).
12 S. Namilae, B. Radhakrishnan, and G.B. Sarma, Comp. Sci. Tech. 67,1302 (2007).
13 I.N. Remediakis, M.G. Fyta, C. Mathioudakis, G. Kopidakis, and P.C. Kelires. Diamond Relat. Mater. 16,1835 (2007).
14 Q. Lu, N. Marks, G.C. Schatz, and T. Belytschkol Phys. Rev. B 77, 014109 (2008).
15 R. Saha and W.D. Nix. Acta Mater. 50, 23 (2002).
16. M. Moseler , P. Gumbsch, C. Casiraghi , A. C. Ferrari, and J. Robertson, Science 309 (2005) 1545
17. C. A. Davis, G. A. J. Amaratunga, and K.M. Knowles, Phys. Rev. Lett. 80 (1998) 3280.
18. R. L. Minear, D. G. Nelson, and J. F. Gibbons, J. Appl. Phys. 43 (1972) 3468.
19. A. H. Eltoukhy and J. E. Greene. Appl. Phys. Lett. 33 (1978) 343.
20 Y.T. Pei, P. Huizenga, D. Galvan, and J.T.M. De Hosson. J. Appl. Phys. 100, 114309 (2006).
21 S. Zhang, D. Sun, Y.Q. Fu and H.J. Du. Surf. Coat. Technol. 198, 74 (2005).
22 A.J. Haq, P.R. Munroe, M. Hoffman, P.J. Martin, and A. Bendavid. Thin Solid Films 516, 267 (2007)
23 J. Neidhardt, C. Walter, J.M. Molina-Aldareguia, M. Herrmann, W.J. Clegg, and L. Hultman. J. Appl. Phys. 103, 123515 (2008).
24 Z.W. Shan, E.A. Stach, J.M.K. Wiezorek, J.A. Knapp, D.M. Follstaedt, and S.X. Mao. Science 305, 654 (2004).
25 S. Zhang, X.L. Bui, X.T. Zeng, and X.M. Li. Thin Solid Films 482, 138 (2005).
26 F. Spaepen. Acta Metall. 25, 407 (1977).
27 E. Ma, Scripta Mater. 49, 663, (2003)
28 C.C. Hays, C.P. Kim, and W.L. Johnson. Phys. Rev. Lett. 84, 2901 (2000).
29 G. He, J. Eckert, W. Loeser, and L. Schultz, Nature Mater. 2, 33 (2003)
30 K.T. Faber and A.G. Evans. Acta Metall. 31, 565 (1983).
31 J.W. Hutchinson. Acta Metall. 35, 1605 (1987).

Chapter 5
TRIBOLOGICAL BEHAVIOR OF NANOCOMPOSITE COATINGS*

In this chapter, the first section concentrates on the effect of roughness of TiC/a-C coatings on tribological behavior while sliding against different counterface materials. It was observed that the ratio of hardness of the counterpart material and of the coating is crucial in determining the influence of roughness on the tribological properties of these coatings. Detailed analyses of the transfer film, sliding surfaces of the ball counterparts, and wear surfaces of the coatings are presented. The roughness evolution and the wear rates of the coatings are discussed. Furthermore, in order to obtain ultra-low friction, in the second section, mechanical, structural, chemical bonding- (sp^3/sp^2) and tribological properties of TiC/a-C:H coatings are presented as a function of substrate bias voltage, Ti-target current, C_2H_2 flow rate and pulse frequency. The change in chemical and phase composition influences the tribological performance where the TiC/a-C:H coatings perform better than the pure a-C:H coatings. Dense, column-free, smooth and ultra-low friction TiC/a-C:H coatings were obtained.

---

* This chapter is published in the following papers:

1. K.P. Shaha, Y.T. Pei, D. Martinez-Martinez, J.Th.M. De Hosson. Influence of surface roughness on the transfer film formation and frictional behavior of TiC/a-C nanocomposite coatings. *Tribol. Lett.*, 40 (2010), in press, doi:10.1007/s11249-010-9691-4
2. K.P. Shaha, Y.T. Pei, D. Martinez-Martinez, J.Th.M. De Hosson. Influence of hardness and roughness on the tribological performance of TiC/a-C nanocomposite coatings. *Surf. Coat. Technol.,* (2010), in press, doi: 10.1016/j.surfcoat.2010.10.021
3. K.P. Shaha, Y.T. Pei, D. Martinez-Martinez , J.C. Sanchez-Lopez, J.Th.M. De Hosson. Effect of process parameters on mechanical and tribological performance of pulsed-DC sputtered TiC/a-C: H nanocomposite films. *Surf. Coat. Technol.,* (2010), in press, doi: 10.1016/j.surfcoat.2010.10.020

5.1 Effect of surface roughness on tribological properties

5.1.1 Introduction:

For metals, in most cases, initial surface textures are rapidly destroyed as soon as wear starts. However, under low loading conditions and/or for materials with a high hardness, wear rate is low and thus the initial surface roughness may play an important role in tribology. This is usually the case of hard protective coatings like Diamond like carbon (DLC)[1]. It is known that the frictional behavior of DLC based coatings is affected by their chemical structure (sp^2/sp^3 content), the content of other alloying elements and the extent of chemical and physical interactions with the surrounding environment.[2] The low friction of these coatings has been mainly attributed to the formation of a transfer film on the sliding surface of the counterface materials. The transfer film is believed to be formed by a friction-induced phase transformation of surface layer of DLC [3], and is mainly composed of amorphous graphite-like carbon that isolates the counterface material. As a result, sliding occurs mainly between the transfer film and the DLC coating, yielding low friction.[4] The presence of small amount of metal from the coating and its oxides in the transfer film in the case of the metal containing DLC are reported.[5,6,7] The presence of metal carbide (TiC) nanocrystallites, at the sliding surfaces enhances the surface graphitization of the DLC matrix and promotes formation of transfer film. The density and chemical nature of the transfer film largely influence the CoF. The transfer film formation is affected by the environment, contact pressure and sliding velocity.[8,,10] Literature mainly focuses on its correlations with coating properties (composition, structure and mechanical) but ignores the possible effects of surface roughness on friction and wear. The substrate surface texture influences the frictional behavior of these coatings, where coatings deposited on polished substrates are usually better.[11] In general, it is believed that a high surface roughness yields major frictional and wear losses mainly during the running-in period.[2] However, the surface roughness may also influence the overall frictional behavior of these coatings. Moreover, the hardness of the mating materials also influences the tribological properties of DLC coatings.[12] As a consequence, it is important to understand the influence of roughness on the formation of the transfer film and CoF of these coatings sliding against different counterface materials in order to underpin their tribological properties.

This section focuses on the evaluation of influence of coating surface roughness on the friction and wear behavior of the TiC/a-C nanocomposite coatings sliding against steel and Si_3N_4 ball counterparts in humid air. The influence of the wear debris on the formation of the transfer film is also discussed. The effect of hardness ratio of the ball/coating tribo-pair on the transfer film formation and tribological behavior of TiC/a-C coatings exhibiting different surface roughness is described. It was observed that frictional behavior of these coatings sliding against steel was strongly influenced by the

surface roughness rather than the coating material itself and was mainly dependent on the transfer film formation. Also, in the case of rough coatings, the hardness of the counterface material plays an important role in governing their tribological performance.

5.1.2 Experimetal

TiC/a-C nanocomposite coatings were deposited on smooth Si-wafer by simultaneous DC sputtering of Ti and pulsed-DC sputtering of graphite targets at 100 kHz pulse frequency in an argon atmosphere. In chapter 3, it was shown that the surface roughness of these coatings increases with increase in deposition time. Thus, TiC/a-C nanocomposite coatings having similar chemical composition and chemical structure (since the sp^2/sp^3 content depends upon the intensity of ion impingement which is same for a given pulse frequency) but exhibiting various surface RMS roughness viz. 1.50 ± 0.03, 4.00 ± 0.09, 6.00 ± 0.1 nm were obtained by 100 kHz p-DC sputtering by keeping the deposition conditions the same, but varying the deposition time viz. 30, 60 and 90 min respectively. The coatings with rms roughness about 1.5 and 6 nm were designated as smooth and rough coatings, respectively. The cross sectional SEM micrographs of these coatings, as discussed in chapter 3, revealed that the smooth coating exhibits weak columnar structure (column diameter ~ 55 nm) whereas the rough coating exhibits strong columnar structure (column diameter ~ 170 nm). However, no cracks were observed on wear tracks, which suggested that no rupture was occurred at the column boundaries during sliding. Thus, the frictional behavior was not affected by the columnar features, as discussed later in detail. The hardness and modulus of these coatings was 17 and 175 GPa, respectively. The tribotests on these coatings were performed using a CSM tribometer, with a ball-on-disk configuration, against Φ6 mm 100Cr6 ball at a sliding speed of 10 cm/s and normal load of 5 N and at room temperature (20-23 °C) and constant relative humidity of 50%. The hardness of the steel and Si_3N_4 balls were 7.5 and 16 GPa, respectively. Optical and confocal microscopy was used to characterize the transfer film formed on the ball counterparts after the tribotest. The thickness of the transfer film was measured on three-dimensional images (512 × 512 pixels) of the wear scar on the steel ball, captured by a Nanofocus® confocal microscope after ultrasonically removing the wear debris. The WSxM® 4.0 Develop10.2 free software was used to select the pixels having transfer film on the confocal micrograph. The average and maximum thickness of the transfer film was then calculated by considering the z values all these pixels. The surface roughness of the coatings before and after the tribotests was measured by AFM. 3D confocal micrographs of the wear tracks on the coatings were captured to measure the wear volume for calculation of wear rates of the coatings.

5.1.3 Results and discussion

5.1.3.1 TiC/a-C coatings sliding against 100Cr6 Steel ball

Figure 5.1 shows the dependence of the CoF on the surface roughness of the TiC/a-C nanocomposite coatings sliding against different ball counterparts.

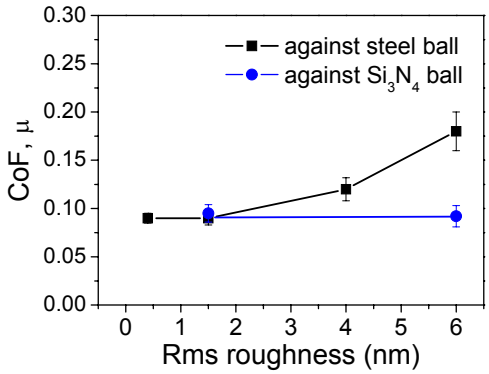

Figure 5.1. Variation of coefficient of friction (averaged over 10000 laps) as a function of roughness of TiC/a-C nanocomposite coatings against 100Cr6 steel and Si_3N_4 balls.

For the given range of roughness, the CoF increases with increasing surface roughness above 1.5 nm, and the rough coating yields a steady state CoF of 0.18, which is twice as much as that observed for the smooth coating (0.09). This clearly reveals that the roughness affects the overall frictional behavior of these coatings. However, below 1.5 nm, the CoF was not influenced by the surface roughness. The CoF of these coatings sliding against Si_3N_4 was independent of the roughness and will be discussed later. The tribological properties of the smooth and rough coatings sliding against different counterface materials have been summarized in Table 5.1.

Table 5.1. Initial roughness (RMS), hardness ratio (r), CoF, wear rate (w_r), maximum thickness (t) of transfer film, fraction of worn material converted to transfer film (f), and factor n for smooth and rough coatings sliding against different ball material

Coating	RMS (nm)	Ball	r	CoF	w_r ($\times 10^{-8}$ $mm^3/N \cdot m$)	t (μm)	f (%)	n (laps)
Smooth	1.5	steel	0.41	0.09	2.94	3.2	28.5	352
		Si3N4	0.94	0.10	3.89	7.3	49.9	213
Rough	6	steel	0.41	0.18	2.37	1.5	12.3	1066
		Si3N4	0.94	0.09	2.89	7.8	66.8	504

Figure 5.2a and b show the surface morphology of the as-deposited smooth and rough coatings, respectively. The rough coating exhibits thick and sharp surface protrusions surrounded by network of valleys and the peak to valley distance was larger than that for smooth coating.

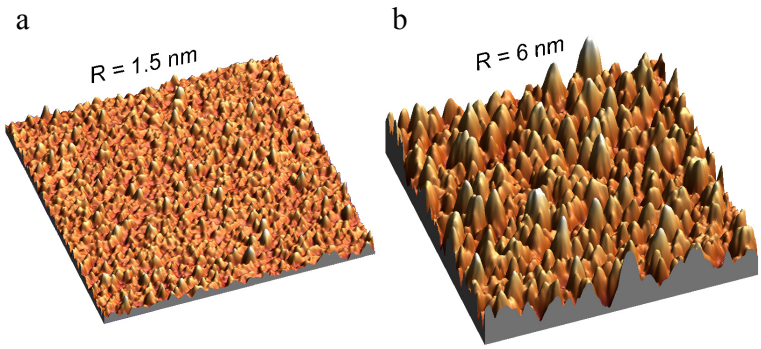

Figure 5.2 AFM micrographs (2×2 μm²) of as deposited TiC/a-C nanocomposite coatings: (a) smooth coating and (b) rough coating. The corresponding RMS roughness (R) is indicated.

The frictional characteristics of the smooth and rough coatings sliding against steel ball are shown in Figure 5.3a.

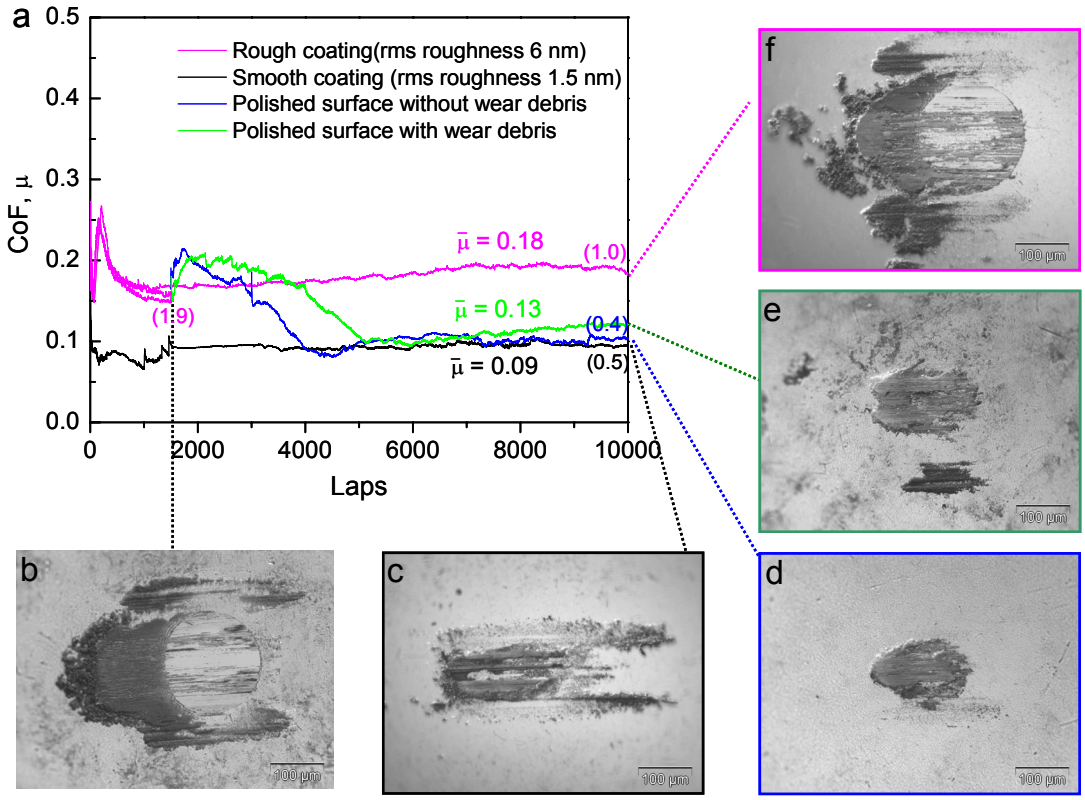

Figure 5.3 (a) Friction characteristics of bearing steel ball sliding against the TiC/a-C coatings having various surface roughness as indicated together with sliding against the polished surface (having rms roughness 1.9 nm) of the rough coating obtained after sliding 1500 laps. The rms roughness (in nm) of the wear tracks on the coatings at the corresponding laps is indicated in round brackets. Optical micrographs showing the wear scar of ø6mm 100Cr6 steel balls after the running-in period against the rough nanocomposite coating (b), after 10000 laps sliding against the smooth coating (c); against the polished surface with (d) and without wear debris (e); and against the rough coating (f). The sliding direction of the balls was from right to left.

In the case of the smooth coating, the CoF was low and remained stable at a value of 0.09. Optical micrograph of the wear scar on the steel ball after sliding against the smooth coating, in Figure 5.3c, revealed that significant amount of material transferred from the coating to the ball surface and a transfer film formed. The diameter of the wear scar was about 95 μm, indicating that the sliding surface of the steel ball remained almost unworn. The 3D confocal micrograph of the wear scar, in Figure 5.4a, shows that a thick transfer film formed on the steel ball. The average thickness of transfer film was 2.2 μm with a maximum of 3.5 μm. The volume of the transfer film was equal to ~ 30% of the volume of the worn material from the coating. The transfer film was evenly distributed and covered almost 90% of the contact area on the steel ball. Thus, the transfer film almost completely isolated the steel ball and facilitated interfacial sliding between the transfer film and the surface of the coating, rather than between the surfaces of the steel ball and the coating, yielding low CoF. Also, simultaneous wear of the coating decreased the surface roughness of the wear track mainly during the initial stages of the sliding. Under these conditions, the formation of a "stable" transfer film, which is always present during entire course of sliding and effectively isolated the ball counterpart, yielding a low steady state CoF.

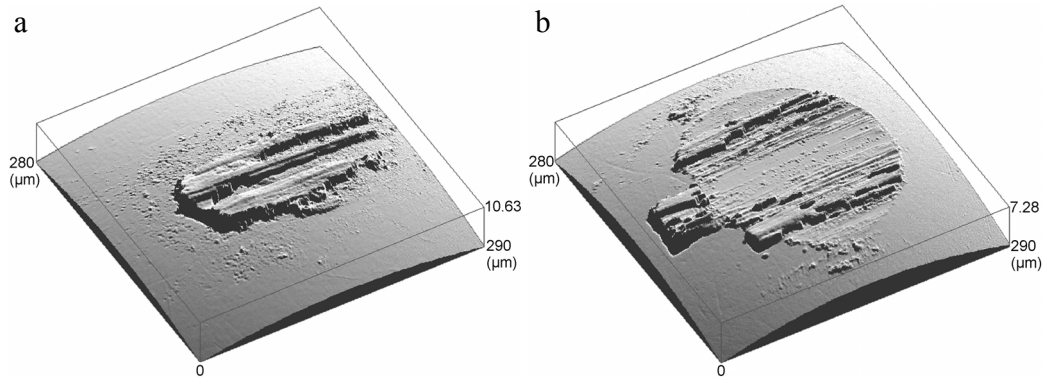

Figure 5.4 Confocal micrographs showing three-dimensional view of wear scar and transfer film formed on steel ball (after ultrasonic cleaning to remove the wear debris) after sliding against TiC/a-C nanocomposite: (a) smooth coating; (b) rough coating.

In the case of the rough coating, a considerable increase in CoF to 0.27 was observed during the running-in period which gradually decreased thereafter and reached to a steady state value, as seen in Figure 5.3a. It is important to note that after the running in period, the CoF did not show a decreasing trend but remained stable at a high value of 0.18. This clearly shows that while sliding against steel, the high surface roughness not only gives a high CoF during the running-in period but also governs the overall frictional behavior of these coatings, with a high steady-state CoF. Optical micrograph of the wear scar on the steel ball after sliding against rough coating for 10000 laps is shown in Figure 5.3f. The wear scar diameter was ~230 μm. Dense and long scratches, parallel to sliding direction, were observed on the wear scar. This wear of the ball was mainly occurred

during the running-in period since the diameter of the wear scar after the running in period (after first 1500 laps), as seen in Figure 5.3b, was ~ 200 μm. The maximum contact pressures are significantly higher for rough surfaces and are present at the surface asperities.[13,14] During initial stages of sliding, due to high contact pressures, the sharp and hard protruding surface asperities of the rough coating causes considerable abrasive wear of the soft steel ball mainly by ploughing mechanism leading to high frictional and wear losses. During subsequent sliding after the running-in period, the removal of surface asperities of the rough coating, as discussed later, reduces the maximum contact pressure and resulted in less wear of the ball. The removal of surface asperities of the rough coating reduces the maximum contact pressure and resulted in less wear of the ball after the running-in period. The wear of the steel ball occurred mainly during the running in period since its wear rate at 1500 laps was equal to 6.94×10^{-8} $mm^3/N\cdot m$ which further reduced to 6.2×10^{-12} $mm^3/N\cdot m$ measured at the end of 10000 laps. This is consistent with the observation made by Harries et. al.[15] where they have shown that abrasiveness of the coating decreases with increasing number of the laps and hence the wear rate of the steel ball decrease. The worn material from the steel ball was mainly accumulated at the front and on the sides of the wear scar as seen in Figure 5.3b and f. However, the wear debris from steel ball may oxidize to form metal oxides and incorporate into the transfer film and contribute to increase in CoF.[5] At the beginning, the wear material transferred from the coating was mainly accumulated in front of the sliding ball and later the transfer film covered the main part of the load bearing contact area. The 3D confocal micrograph of the wear scar on the steel ball after removing the wear debris by ultrasonic cleaning is shown in Figure 5.4b. The transfer film was rather thin and unevenly distributed and covered only about 30% of the contact area on the steel ball. The average thickness of was 0.8 μm with a maximum up to 1.5 μm which was less than that observed for the smooth coating. The volume of the transfer film was only ~ 13 % of the volume of the worn material from the coating which indicates that most of the worn material was transformed into wear debris. The transfer film failed to isolate the sliding surface of the steel ball completely. Also, after 10000 laps, a relatively rougher wear track compared to that on the smooth coating was observed and will be discussed later. While sliding under these conditions, the transfer film becomes "unstable" due to repeated break-down and formation and it fails to cover the majority of the contact area leading to high CoF. It is known that the size of wear debris increases with increasing surface roughness.[16] The comparatively larger wear debris which form during initial stages of sliding against rough coating may further impede the formation of transfer film and leads to increase in CoF as discussed later.

To comprehend the effect of surface roughness, an initial tribotest for 1500 laps was performed to polish out the surface asperities on the rough TiC/a-C coating. It was

observed that the depth of the wear track on the coating was less than 20 nm as measured by confocal microscopy. Thus, the thickness of the coating and hence the columnar structure remained almost the same, but rather a significant decrease in the surface roughness of the coating from an initial value of 6 nm to 1.9 ± 0.1 nm. This polished surface exhibited plateaux and sharp grooves. After removing the wear debris from the wear track by ultrasonic cleaning, a tribotest was performed with a new steel ball on this polished surface. This yielded a steady-state CoF of 0.10. For the same coating exhibiting strong columnar features, as the surface roughness decreased from 6 to 1.9 nm, the steady state CoF was reduced from 0.18 to 0.1. Also, the values of steady-state CoF, as seen in Figure 5.3a, for the polished surface exhibiting strong columnar structure and the smooth coating exhibiting comparatively weaker columnar structure are comparable. This further demonstrates that the CoF was largely affected by the surface roughness of the TiC/a-C coatings and independent of the columnar microstructure provided that no cracks formed along the column boundaries. The thickness of the transfer film was also comparable to that observed against the smooth coating. However, in the case of polished surface the formation of transfer film was a rather sluggish process since the steady-state CoF was reached only after 2500 laps, in comparison to the smooth coating where a transfer film formed within less than 30 laps. This indicates that the wear of initial small surface asperities of the smooth coating facilitate the transfer film formation. The wear scar on the steel ball shown in Figure 5.3d revealed that the transfer film completely covered the contact area. No noticeable wear of the ball was observed. On the other hand, the surface roughness of the wear track was further reduced from 1.9 to 0.4 ±0.1 nm. Furthermore, while sliding against this 0.4 nm smooth polished surface of the rough coating with a new steel ball the steady-state CoF (not shown) was equal to 0.1. This suggests that below a certain roughness, 1.5 nm in case of these coatings, the friction was not influenced by the surface roughness.

To understand the role of wear debris, another tribotest was performed with a new steel ball on a polished surface (rms roughness 1.9 nm) of the rough coating but without removing the wear debris. The average CoF was 0.13 in this case, as shown in Figure 5.3a. It is noteworthy that more laps were needed to reach the steady-state CoF as compared to those required in the absence of wear debris on the wear track. This indicates that the presence of hard wear debris retards the formation of the transfer film, likely serving as three body abrasive to break down the tender transfer film, as indicated by the dense fluctuations in the CoF curve at the beginning of test. The wear debris may re-circulate in and out of the contact during the running-in period as observed by Scharf et al..[17] The wear debris were collected by the steel ball as shown in Figure 5.3e and also were accumulated on both sides of the wear track, indicating that they were eventually removed from the sliding contact.

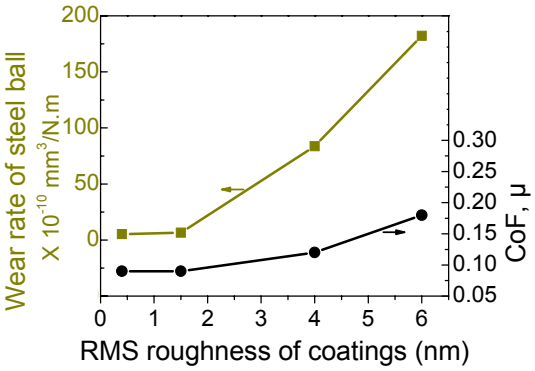

Figure 5.5 Wear rate of steel ball and CoF as a function of surface roughness of TiC/a-C nanocomposite coatings. The CoF and wear of the steel ball increased with increasing surface roughness above 1.5 nm.

Figure 5.5 shows the wear rate of the steel ball as a function of roughness of the TiC/a-C coatings. The wear volume of the steel balls was calculated according to the size of wear scars. The wear rate of the steel ball increased significantly with increasing surface roughness of the coatings and follows similar trend as that of CoF. Thus, the increase in CoF with increasing roughness can be correlated to the wear of the steel ball; as the contact area on the steel ball increases, its effective coverage by the transfer film is increasingly difficult.

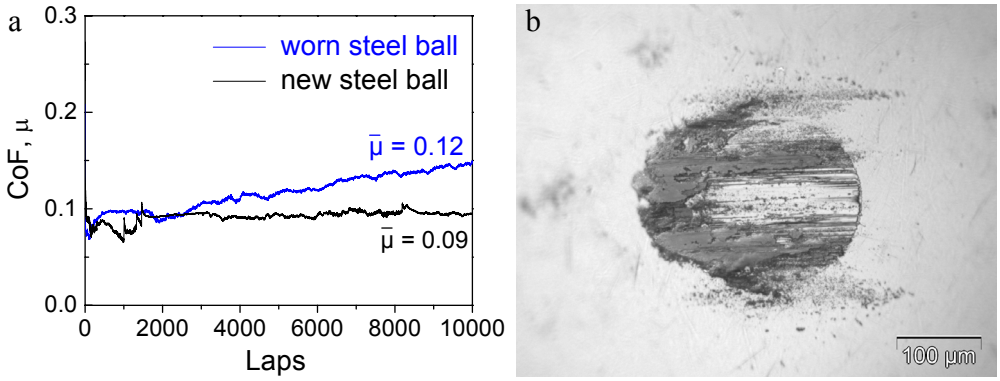

Figure 5.6 (a) Friction characteristics of the smooth TiC/a-C coating against steel ball having rough sliding surface (obtained after sliding against rough coating and ultrasonically cleaned as shown in Figure 5.4b). The tribotest result on the same coating against new steel ball, same as in Figure 5.3a, is included for comparison. (b) Optical micrographs of the wear scar on the worn steel ball after 10000 laps.

Furthermore, to understand the effect of the contact area on the steel ball on the CoF, a worn steel ball with a wear scar of 230 μm in diameter shown in Figure 5.4 (which was obtained after removing the wear debris by ultrasonic cleaning of the steel ball in Figure 5.3f) was slid against the smooth coating. It is important to note that there was a pre-existing transfer film on this worn steel ball. Figure 5.6a shows the friction characteristic of this worn steel ball against the smooth coating. During the initial stages

of sliding the CoF was low (~ 0.09). This is due to the pre-existing transfer film on the worn steel ball since the protrusions of the pre-existing transfer film first comes into contact with the smooth coating. Also, the mean contact pressure was lower as it was distributed over a large contact area. During subsequent sliding, CoF gradually increased to 0.15 at the end of 10000 laps. This was due to simultaneous wear of the existing transfer film and of the smooth coating. As the contact between the two counterfaces was conformal, a concentrated wear of the coating was observed at the regions corresponding to the protrusions of the pre-existing transfer film. As the contact area on the steel ball increases during the sliding, the transfer film fails to cover it effectively leading to gradual increase in CoF. After 10000 laps, the transfer film shown in Figure 5.6b only partially covered the contact area on the worn steel ball. The mean CoF was 0.12 which was higher than that observed for the same coating against a new steel ball, as seen in Figure 5.6a. The small contact area on the new steel ball, in Figure 5.3c, was effectively covered by the transfer film and yielded a lower CoF. In contrast, the relatively larger contact area on the worn steel ball against the same coating was not covered effectively by the transfer film, leading to higher CoF. This clearly indicates that a large contact area on the counterpart ball hinders itself from effective coverage by the transfer film.

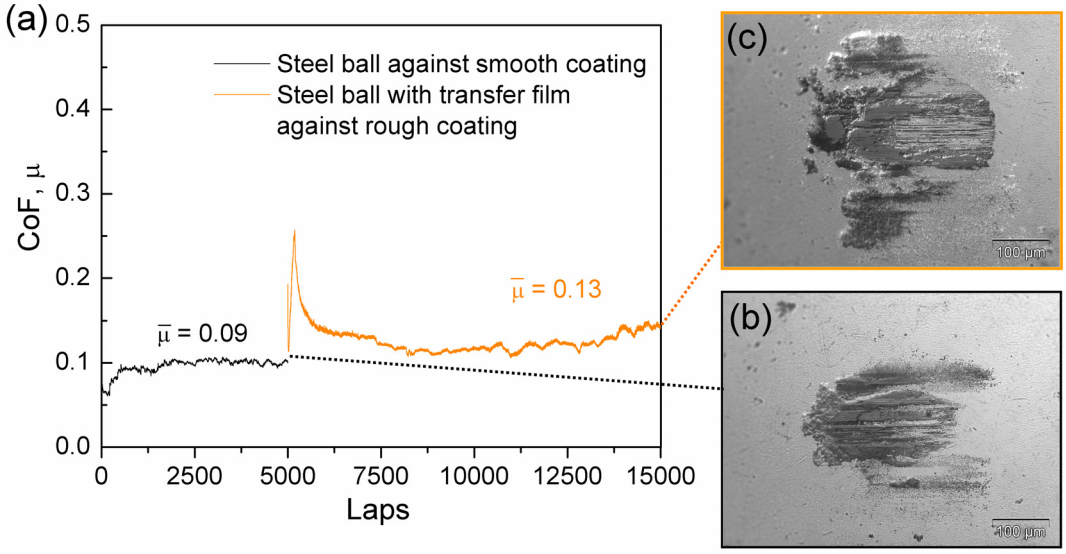

Figure 5.7 (a) Friction characteristics of steel ball having initial transfer film (created by sliding against smooth coating indicated by black color), sliding against the rough TiC/a-C nanocomposite coating indicated by orange color; Optical micrographs of the steel ball having initial transfer film (b) before and (c) after sliding against the rough coating, respectively.

To reveal the effect of surface roughness on an existing transfer film, a transfer film was initially created on a steel ball by sliding it against the smooth coating for 5000 laps, and then this ball with transfer film was further slid for 10000 laps against the rough coating as shown in Figure 5.7a. After a significant increase during the running-in period,

similar to that observed in Figure 5.3a for rough coating, the CoF gradually reduced to about 0.13. Abrasive wear during the running in period yielded an increase in the size of wear scar from ~ 100 µm to ~ 175 µm as shown in Figure 5.7b and c, respectively. The mean CoF (0.13) was lower than that observed for a steel ball without having initial (existing) transfer film (0.18). It indicates that the existing transfer film was not completely removed from the steel ball during the running-in period. Also, the wear scar on the ball having existing transfer film was smaller (~ 175 µm) than that observed on steel ball (~230 µm) without having existing transfer film. This observation revealed that the existing transfer film protected the steel ball to some extent during the running-in period. It was noted that the CoF was not reaching to a steady state but rather was fluctuating and exhibited increasing trend at the end of the test as seen in Figure 5.7a. This shows that the large sliding surface of the steel ball, caused during running-in period, destabilizes the transfer film formation and eventually the transfer film fails to cover the entire contact area leading to increase in CoF.

5.1.3.2 TiC/a-C coatings sliding against Si_3N_4 ball

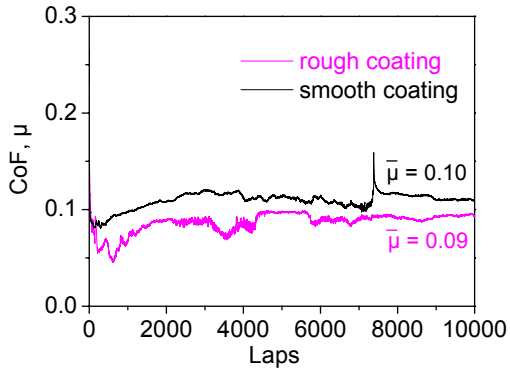

Figure 5.8 Friction characteristics of smooth and rough TiC/a-C coatings sliding against Si_3N_4 ball at 5 N normal load, sliding velocity 10 cm/s and relative humidity of 50% at 23 °C. The CoF was independent of the roughness of these coatings.

Figure 5.1 shows that the CoF of TiC/a-C coatings sliding against Si_3N_4 ball was independent of the surface roughness. The frictional characteristics of the smooth and rough coating sliding against Si_3N_4 ball are shown in Figure 5.8. For both the coatings, the CoF was low and remained stable at ~ 0.1, similar to that observed in the case of the smooth coating sliding against steel ball, as shown in Figure 5.3a. It is important to note that there was hardly a running-in period of high CoF observed even for the rough coating. Optical micrographs of the wear scar on the Si_3N_4 balls after the tribotest against smooth and rough coatings are displayed in Figure 5.9a and b, respectively.

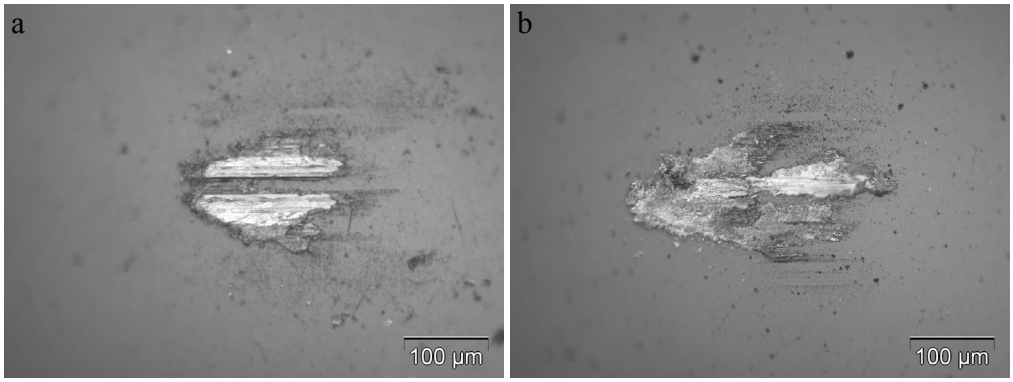

Figure 5.9 Optical micrographs of the wear scar on Si_3N_4 ball, after 10000 laps, sliding against TiC/a-C nanocomposite: (a) smooth coating; (b) rough coating.

Significant amount of material was transferred from the coating to the ball surface and the transfer film was formed. No wear of the Si_3N_4 ball was observed while sliding against both the coatings and the surface of the Si_3N_4 ball remained smooth.

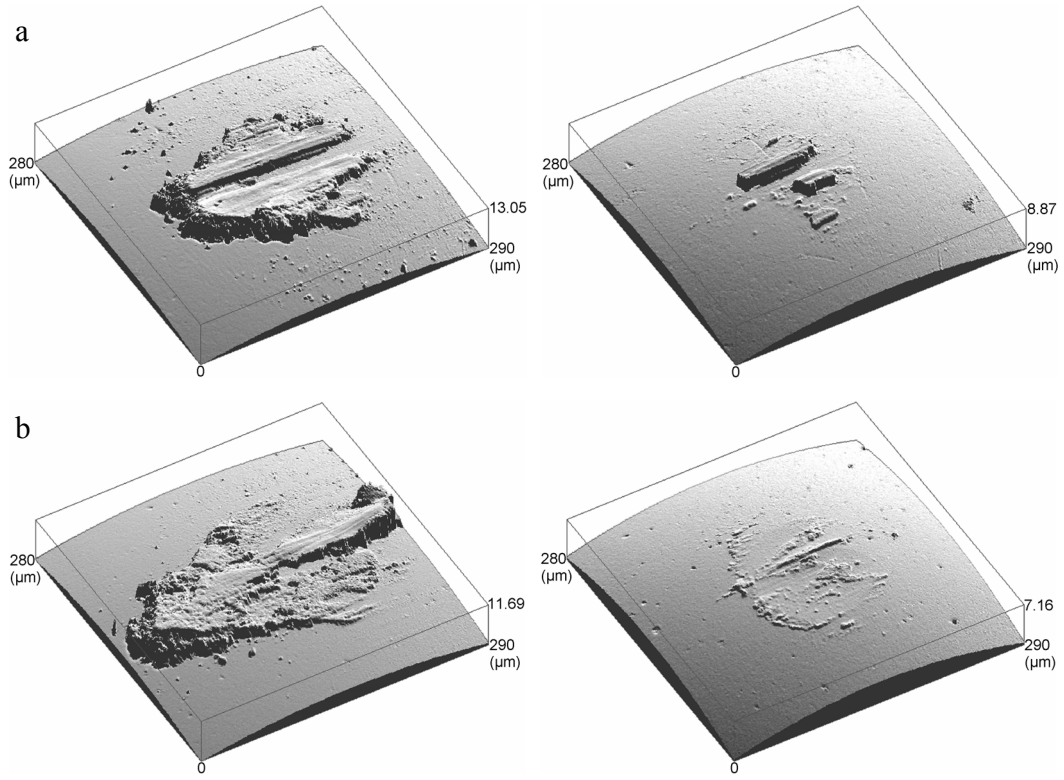

Figure 5.10 Confocal micrographs showing three-dimensional view of wear scar and transfer film formed on Si_3N_4 ball after sliding against TiC/a-C nanocomposite: (a) smooth coating and (b) rough coating. The corresponding confocal micrographs of the wear scar after removing the wear debris by ultrasonic cleaning are shown on right side. No wear of the Si_3N_4 ball was observed in both cases.

The 3D confocal micrographs of the Si_3N_4 ball after the tribotests, in Figure 5.10a and b, show that thick transfer film formed in both cases. In the case of smooth coating,

the average thickness of transfer film was 3.25 μm with a maximum of 7.32 μm. A 50% volume of the worn coating material was transformed on the ball indicating efficient transfer film formation. The transfer film was evenly distributed and covered almost all the contact area. Similarly, in the case of rough coating, the average thickness of transfer film was 2.86 μm with a maximum up to 7.83 μm. A most efficient transfer film was formed with the transfer film volume ~ 65 % of the total worn volume of the coating. In both the cases, the transfer film completely isolated the Si_3N_4 ball and facilitated interfacial sliding between the transfer film and the surface of the coating, rather than between the surfaces of the Si_3N_4 ball and the coating yielding low CoF. It was noted that the thickness of the transfer film formed on Si_3N_4 ball was more than that observed for steel ball. The right sides of Figure 5.10a and b show the Si_3N_4 ball after ultrasonic cleaning. In the case of smooth coating, no wear of the Si_3N_4 ball was observed and only portions of a thick well adhered transfer film were seen. In the case of rough coating, the transfer film was almost completely removed after the cleaning, and few wear scratches were observed on the Si_3N_4 ball. The wear of Si_3N_4 ball was negligible and hence is not reported. Also, the wear of the coatings decreases the surface roughness of wear tracks on both the coatings during the initial stages of the sliding, as discussed later. Since no wear of the ball was occurred, the contact area on the Si_3N_4 ball was small. Under these conditions, a stable transfer film form which covered almost all the contact area on the Si_3N_4 ball leading to a low steady state CoF.

5.1.3.3 Hardness ratio and sliding surfaces

In order to understand the different wear behavior of the steel ball and Si_3N_4 ball against the rough coating, mechanical properties of these materials were considered. The hardness of the steel ball, Si_3N_4 ball and the TiC/a-C nanocomposite coatings were 7, 16.5 and 17 GPa, respectively. Thus, the hardness ratio of the ball and the coating material for steel was 0.41, whereas it was 0.97 for Si_3N_4.

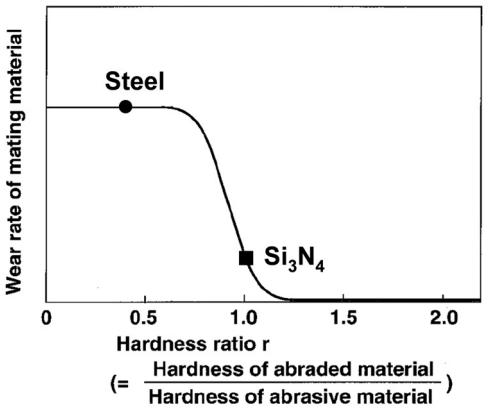

Figure 5.11 Schematic diagram of effect of hardness ratio on wear of abraded material against abrasive. [18].

During the initial stage of sliding the protruding surface asperities of the coating causes abrasive wear of the ball counterpart mainly by ploughing mechanism. Thus, the hardness of the abrasive asperity becomes important in abrasive wear. Figure 5.11 shows that when the hardness ratio r (the hardness of abraded material/the hardness of abrasive material) stays below a certain critical value r_{c1} (0.5 to 0.8), abrasive wear clearly takes place.[18] However, with the increase in hardness ratio above the critical value r_{c1}, wear volume of mating material decreases, and finally almost no wear is observed when r is close to a critical value r_{c2} (1 to 1.4).[18] In the case of steel ball, the hardness ratio is less than the critical value r_{c1} and hence considerable wear occurs while sliding against rough coatings. However, the hardness ratio for Si_3N_4 ball approaches to the critical value r_{c2} and almost no wear occurs. Thus, our results are consistent with the correlations of hardness ratio and abrasive wear, as described above.

The coatings experience wear during sliding. Since the CoF for steel and Si_3N_4 ball against the rough coating showed remarkable difference, the evolution of roughness of the wear track on the rough coating was considered. The evolution of surface roughness of wear track on the rough coating with increasing the number of laps against steel and Si_3N_4 ball was shown in Figure 5.12 and Figure 5.13, respectively. During the initial stages of sliding, the peaks of the surface asperities on the rough coating were truncated, resulting in a polished surface consisting of a plateaux and sharp grooves as seen clearly in the surface profiles in Figure 5.14. This leads to a decrease in the surface rms roughness of the coating from an initial value of 6 nm to ~ 1.9 nm against steel after 1500 laps and against Si_3N_4 ball after 500 laps. Truncation of surface asperities occurred mainly during the running-in process.

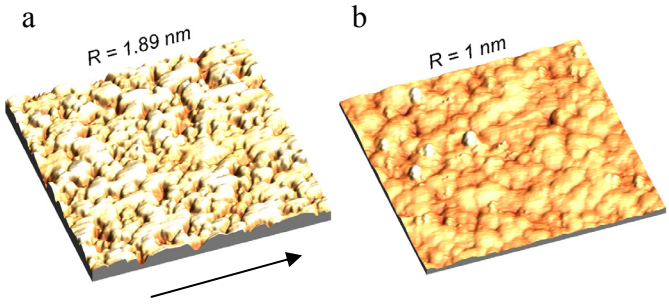

Figure 5.12 AFM micrographs (2×2 μm²) showing surface morphology of the wear track on rough TiC/a-C nanocomposite coating after sliding against steel ball for (a) 1500 and (b) 10000 laps. The corresponding RMS roughness (R) is indicated. The arrow indicates sliding direction of the coating. The surface of the wear tracks was cleaned to remove the loose wear debris before AFM measurements.

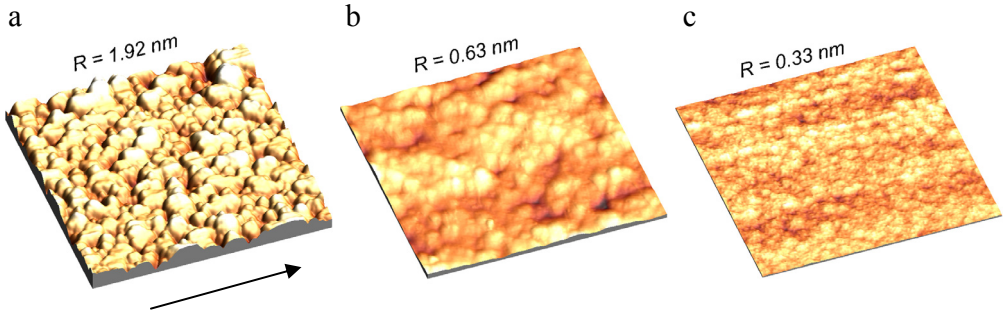

Figure 5.13 AFM micrographs (2×2 μm²) showing surface morphology of the wear track on rough TiC/a-C nanocomposite coating after sliding against Si_3N_4 ball for (a) 500; (b) 1500 and (c) 10000 laps. The corresponding RMS roughness (R) is indicated. The arrow indicates sliding direction of the coating. The surface of the wear tracks was cleaned to remove the loose wear debris before AFM measurements.

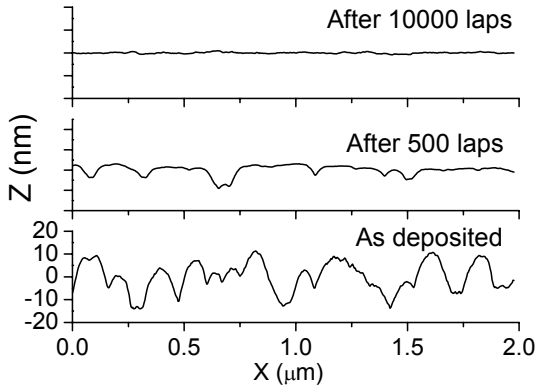

Figure 5.14 Surface profiles of rough TiC/a-C coating sliding against Si_3N_4 ball for the number of laps as indicated.

It is noted that the comparatively harder Si_3N_4 ball quickly removed the top of the surface asperities and reduced the roughness to ~ 1.9 nm in 500 laps which in the case of the soft steel ball required 1500 laps. During the subsequent sliding, the roughness of the wear track further reduced, yielding a surface having roughness of 1 nm against steel and 0.33 nm against Si_3N_4 ball at the end of 10000 laps as seen in Figure 5.12b and Figure 5.13c, respectively. Thus, during the entire course of sliding, the sliding surface of the rough coating against steel ball was relatively rougher that that against Si_3N_4 ball.

The plots of surface roughness as a function of number of laps for both the coatings against both ball counterparts were shown in Figure 5.15. The surface roughness shows a transition from an initial high rate of decrease during the running-in period to a steady decrease at low rate thereafter. This behavior was well fitted to an exponential decaying function.

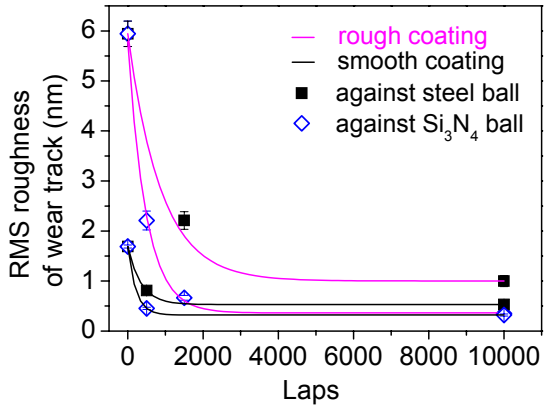

Figure 5.15 Surface roughness evolution of the wear tracks on the smooth and rough TiC/a-C coatings sliding against steel and Si3N4 ball counterparts.

Although the decrease of roughness in the smooth coating was modest in comparison with the rough coating, it was fitted also to the same decaying function as follows:

$$\frac{R - R_f}{R_i - R_f} = \exp\left(\frac{-x}{n}\right)$$

where R is the roughness of the wear track after x laps, R_i and R_f are the initial and final roughness of the wear track and n (in number of laps) can be interpreted as the difficulty to decrease the roughness (a larger value of n indicates that more laps are needed to decrease it).

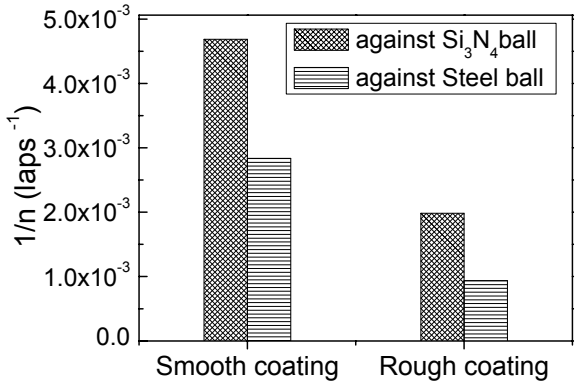

Figure 5.16 Plot of factor 1/n for smooth and rough TiC/a-C coatings sliding against steel and Si3N4 ball counterparts.

The values of n are listed in Table 5.1. Figure 5.16 shows the values of the factor 1/n for smooth and rough coating against steel and Si_3N_4 balls, which can be interpreted in terms of rate of decrease of the roughness of the coatings. This factor mainly depends upon the hardness ratio of the ball/coating tribo pair but also can be influenced by

transfer film formation. Thus, the lower hardness ratios in the case of steel ball (responsible also for its abrasive wear against the rough coating) are reflected in lower values of 1/n (cf. Table 5.1). Besides, having the same hardness ratio, the value of 1/n for a Si_3N_4 ball against the smooth coating was larger than sliding against the rough coating. This was caused by a comparatively faster and more efficient formation of the transfer coating on the Si_3N_4 against rough coating since the higher surface roughness promotes the formation of transfer film.

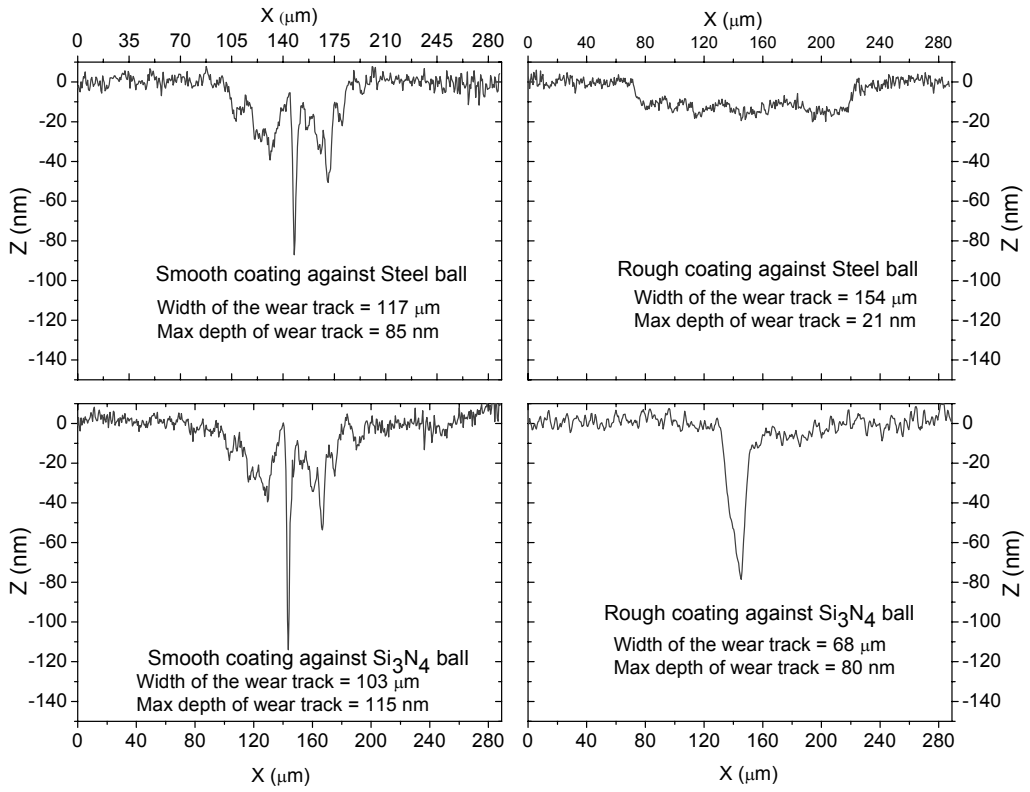

Figure 5.17 Cross sectional profiles of the wear tracks on the smooth (left) and rough (right) TiC/a-C nanocomposite coatings against different ball counterparts as indicated. The corresponding values of width and maximum depth of the wear tracks are indicated.

The wear surfaces of the coatings were studied by confocal microscopy in order to evaluate the wear volume which then converted to wear rates of the coatings. Figure 5.17 shows the cross sectional profile of the wear tracks on the smooth and rough coating against steel and Si_3N_4 ball. It clearly revealed that the width of the wear track on the rough coating against steel ball (~ 150 μm) was larger than that observed against Si_3N_4 ball (~ 70 μm). Since a little wear of Si_3N_4 ball was occurred, the width of the wear track on the rough coating was smaller. However, wear of the steel ball during the running-in period increases contact area on the steel ball which leads to a corresponding increase in the width of the wear track on the rough coating. This also explains the surface roughness evolution since sliding on a narrow and concentrated wear track facilitates quick removal

of surface asperities due to high contact pressure in the case of Si_3N_4 whereas sliding against a wide wear track reduces the contact pressure and hence a lower rate of decay and absolute value of surface roughness during running-in period and at the end of 10000 laps for steel. The widths of the wear racks on the smooth coating (~100 μm) were similar against both the ball counterparts. It was noted that the width of the wear track on the rough coating against Si_3N_4 ball was smaller than that observed on the smooth coating. It can be explained by the quick formation of transfer film on the Si_3N_4 ball since the initial roughness of the rough coating promotes the transfer film formation in the absence of the wearing of the ball. This is also reflected in the maximum thickness of transfer film which is larger in this case. As the sliding progresses, a slight increase in the width occurs with a faster deepening of the wear track. The much faster deepening of the wear track near the centre was a result of the unevenly distributed contact pressures over the contact interface, the pressure being the highest at the centre of the track.

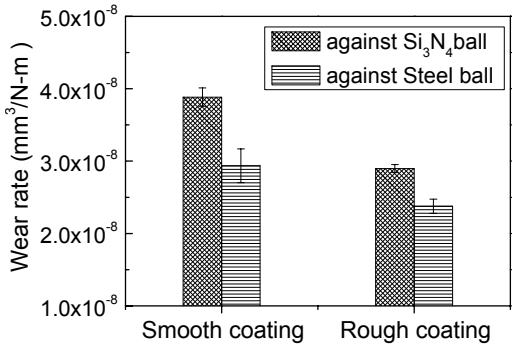

Figure 5.18 Wear rates of the smooth and rough TiC/a-C nanocomposite coatings sliding against steel and Si_3N_4 ball counterparts.

The wear rates of the smooth and rough coatings against steel and Si_3N_4 were shown in Figure 5.18. It was noted that the wear rates of the rough coating were always lower than the smooth coating against the respective ball counterparts under the same loading conditions. It is important to note that in the case of rough coating, the high contact pressure during the initial stage of sliding causes considerable wear of the steel ball and a little wear of the coating. During subsequent sliding, since the contact area increases, the mean contact pressure decreases and hence a little wear of both the ball and the coating occurs. Thus, the wear rate of the rough coating was less mainly due to wearing of the steel ball. In the case of smooth coating, a little wear of the steel ball leads to a contact pressure distribution concentrated over a comparatively narrow wear track yielding increased wear rate of the coating. Similarly, a very little wear of the Si_3N_4 balls causes contact pressure distribution concentrated over a narrow wear tracks and yields relatively higher wear rates of the coatings. The quick formation of the transfer film on the Si_3N_4 ball against rough coating yields a lower wear rate of the rough coating than compared to

a smooth coating. The wear rates of the smooth coating against Si_3N_4 ball was little higher than that observed against steel ball. It can be explained because of higher maximum and mean contact pressure against Si_3N_4 due to its higher modulus of elasticity compared to that of steel.

The rate of reduction in roughness of the wear tracks and the wear rates of the coatings were found to be correlated since the variation of the factor 1/n, in Figure 5.16, and the wear rates, in Figure 5.18, for different tribo-pairs follow similar trend. The parameter 1/n accounts for the rate of decrease of the roughness, while the wear rate accounts for the rate of removal of material of the coating. Considering that the coatings are tough (no cracks on the wear tracks), such a correlation seems logical, since the wearing takes place by gradual removal the surface asperities during sliding. Such a removal of material from top of asperities causes formation of plateaux and grooves, as seen in Figure 5.14, resulting in decrease in RMS roughness of the coating. Thus, the rate of removal of material (wear rate) and rate of decrease of RMS roughness are correlated in case of tough coating where the wear takes place by gradual polishing of the surface asperities of the coating. Thus, a low wear rate reflects in a low rate of decrease in surface roughness of the wear track. For example, the rate of decrease in roughness of the rough coating against steel was lower than that against Si_3N_4, since the wear rate of the coating against steel was lower than that observed against Si_3N_4.

5.2 Tribological performance of TiC/a-C:H coatings

In order to achieve ultra-low friction ($\mu < 0.1$) in DLC coatings, one has to reduce or eliminate the main causes of friction. One of the requirements, as discussed in the previous section, is to produce smooth coatings. However, it was observed that, below a certain roughness (1.5 nm for the TiC/a-C coatings) the friction was not influenced by the surface roughness and the atomically smooth TiC/a-C coatings gives a CoF ~ 0.1. To further reduce the CoF below 0.1, the surface of the coatings must have the highest degree of chemical passivity or inertness so as to reduce the adhesive interactions during sliding which may also strongly influence the friction. In these coatings, the adhesive interactions can primarily result from several types of bonding. Among others, covalent bond interactions between unoccupied or dangling σ-bonds of sliding interfaces of DLC coatings can account for a significant source of adhesion and contribute to high friction.[2] It is known that hydrogen has a strong chemical affinity towards carbon, it bonds strongly to some of the carbon atoms and thus effectively passivates their unoccupied or free σ-bonds. Once passivated, such carbon atoms become chemically inert and cause very little adhesive interactions during sliding and lead to low friction.[2] So efforts were made to obtain ultra low friction ($\mu < 0.1$) TiC/a-C:H nanocomposite coatings. Moreover, the effect of process parameters viz. substrate bias voltage, Ti-target current, C_2H_2 flow rate

and pulse frequency on the mechanical, structural and tribological performance of TiC/a-C:H coatings deposited by pulsed-DC magnetron sputtering of Ti-targets in Ar/C_2H_2 plasma was studied in detail It was observed that the TiC/a-C:H coatings perform better than the pure a-C:H coatings. The structural and mechanical properties of these coatings are correlated to the deposition conditions. Dense, tough and ultra-low friction TiC/a-C:H nanocomposite coatings were obtained under optimized conditions.

5.2.1 Experimental

TiC/a-C:H nanocomposite coatings were deposited on Si (100) wafers by simultaneous p-DC sputtering of two Ti targets, opposite to each other, in an Ar/C_2H_2 atmosphere. The substrates, located at 80 mm distant from the targets, were pulsed biased at 250 kHz pulse frequency (50 % duty cycle). The base pressure of the chamber before deposition was $3\text{-}4\times10^{-6}$ mbar. The substrates were first ultrasonically cleaned in acetone followed by Ar plasma etching for 15 minutes at p-DC -400 V bias voltage at 250 kHz and 87.5 % duty cycle. A CrTi interlayer, having a thickness of approximately 150 nm, was deposited to improve the interfacial adhesion. Finally, two Ti targets were sputtered in p-DC reactive mode in an Ar/C_2H_2 atmosphere to deposit the coatings. The substrate holder was rotated by 3 rpm. No external heating was applied to the substrates. The maximum temperature was measured at 120°C during deposition of these coatings. To study the microstructure and deposition rate as a function of pulse frequency, the coatings were deposited at 0 (DC), 200 and 350 kHz pulse frequency (70% duty cycle). In order to investigate the effect of various process parameters on the mechanical and tribological properties of 200 kHz p-DC sputtered coatings, the negative substrate bias voltage, Ti-target current, and the acetylene flow rate were varied in the range from 40 to 150 V, 0.6 to 1 A, and 8 to 12 sccm, respectively. The flow rate of Ar gas was kept constant at 12 sccm for all the depositions. Furthermore, the properties of optimized (in terms of microstructure and composition) 200 kHz and 350 kHz p-DC sputtered TiC/a-C:H coatings were compared.

5.2.2 Results and discussion

The results are presented as follows. Firstly, the microstructural and surface morphological evolutions of the TiC/a-C:H nanocomposite coatings deposited by p-DC sputtering at different pulse frequencies are presented with particular emphasis on inhibiting the column formation. Then, the effect of substrate bias voltage, phase and chemical composition on the mechanical and tribological properties of the a-C:H and TiC/a-C:H is discussed in detail. The synthesis conditions and properties of the coatings are summarized in Table 5.2. Finally, the effect of pulse frequency applied to the Ti-target on the mechanical and tribological properties of the optimized TiC/a-C:H coatings (in terms of microstructure and composition) is evaluated and compared.

5.2.2.1 *Microstructural evolution*

Figure 5.19 shows the cross sectional SEM micrographs of TiC/a-C:H nanocomposite coatings deposited for 120 min by DC and pulsed-DC sputtering at 200 and 350 kHz pulse frequency by keeping the current applied to Ti-targets and C_2H_2 flow rate and substrate bias voltage fixed at 1 A and 8 sccm and 40 V , respectively.

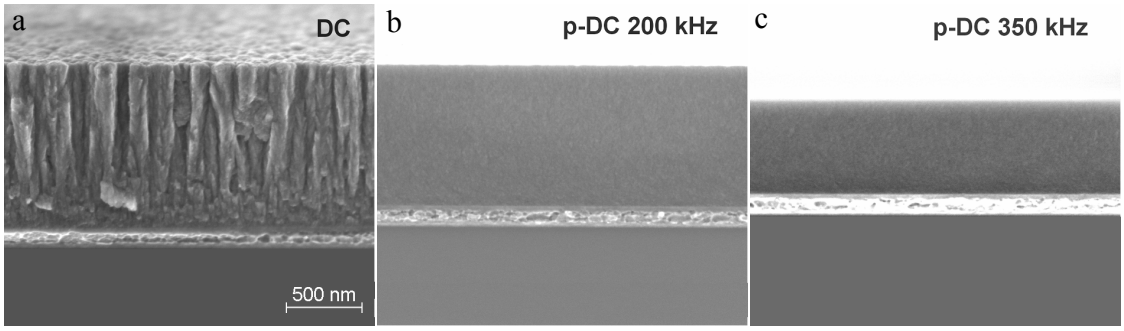

Figure 5.19. Cross sectional SEM of TiC/a-C:H nanocomposite coatings deposited by (a) DC sputtering; and p-DC sputtering at (b) 200 kHz and (c) 350 kHz pulse frequency. (See text for detailed deposition conditions).

The coating deposited by DC sputtering, as seen in Figure 5.19a, exhibited strong columnar features. However, switching from DC to pulsed-DC sputtering at 200 and 350 kHz pulse frequency the microstructure evolved from columnar to column-free, as seen in Figure 5.19b and c, respectively. Since the column boundaries are potential source of failure since they facilitate the crack initiation and propagation, a column-free microstructure is necessary for improved toughness under loading and contact sliding.[8] The dense, column-free coatings deposited by p-DC sputtering coatings are expected to be tougher than compared to the DC sputtered coatings.

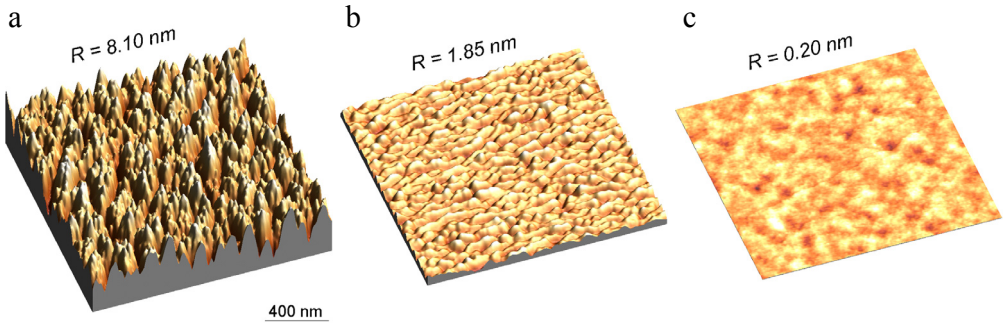

Figure 5.20. AFM topography images of TiC/a-C:H nanocomposite coatings deposited by (a) DC sputtering; and p-DC sputtering at (b) 200 kHz and (c) 350 kHz pulse frequency. The corresponding RMS roughness (R) is indicated. (See text for detailed deposition conditions).

Table 5.2: Synthesis conditions (substrate bias voltage, Ti Target current – I_{Ti}, C_2H_2 flow rate, pulse frequency - f), chemical composition, surface rms roughness –R, Raman analysis (I(D)/I(G) ratio, Position of G peak), Mechanical properties (Hardness - H, Young's modulus - E^*, H/E^* ratio), Residual stress - σ and tribological properties (coefficient of friction CoF and wear rate – Wr × 10^{-7} $mm^3/N.m$) of p-DC sputtered coatings.

	Bias (-V)	ITi (A)	C2H2 (sccm)	f (kHz)	Composition (at.%)			R (nm)	$\frac{I(D)}{I(G)}$	G-peak position	H (GPa)	E* (GPa)	H/E*	σ (-MPa)	CoF	Wr
					Ti	C	O									
	40	1.0	8	200	17.31	79.80	1.37	1.85	0.91	1563.4	14.1	128.6	0.11	-	0.08	1.92
*	80				17.64	79.03	1.32	0.36	0.90	1562.6	15.8	142.6	0.11	-	0.09	1.60
	100				-	-	-	0.31	-	-	16.1	143.8	0.11	-	0.10	2.43
	150				17.82	78.98	1.21	0.23	0.74	1558.8	16.4	144.3	0.11	-	0.11	3.0
	80	0.6	8	200	0.28	96.16	0.69	-	-	-	24.5	178.1	0.14	-	0.15	-
**		0.75			12.47	84.09	1.07	0.61	0.73	1558.2	16.1	136.3	0.12	2158	0.05	0.66
*		1.0			17.64	79.03	1.32	0.36	0.90	1562.6	15.8	142.6	0.11	-	0.09	1.60
**	80	0.75	8	200	12.47	84.09	1.07	0.61	0.73	1558.2	16.1	136.3	0.12	2158	0.05	0.66
			10		0	96.31	0.20	0.69	0.25	1536.6	22.9	165.2	0.13	2418	0.10	1.14
			12		0	97.06	0.34	3.15	0.23	1534.8	23.8	168.1	0.14	2566	0.14	1.26
**	80	0.75	8	200	12.47	84.09	1.07	0.61	0.73	1558.2	16.1	136.3	0.12	2158	0.05	0.66
				350	12.19	84.30	1.08	0.52	0.49	1552.0	17.2	139.7	0.12	2808	0.07	0.82

*Coatings marked with * and ** are repeated for clarity.*

The surface morphologies of these coatings are shown in Figure 5.20. In the case of DC sputtering, as seen in Figure 5.20a, the surface showed cauliflower morphology with peaks surrounded by a network of valleys and the peak-to-valley distance was large. However, in the case of p-DC sputtering, the peak-to-valley distance considerably decreased and the surface exhibited small ripples at 200 kHz (Figure 5.20b) and nanosized bumps at 350 kHz (Figure 5.20c). Consequently, a drastic decrease in surface rms roughness, from about 8 nm for DC sputtered coatings to ~ 1.8 and 0.2 nm in the case of 200 and 350 kHz p-DC sputtered coatings, respectively, was observed. It must be noted that these coatings were deposited at 40 V. Thus, ultra-smooth coatings can be obtained by 350 kHz p-DC sputtering at low substrate bias voltage. The Ar^+ ions energy and flux delivered to the growing coating increases with increasing pulse frequency, as discussed in chapter 3, and the enhanced surface diffusion driven growth ascertains a smooth growth front and hence a column-free microstructure, as explained in chapter 4. The microstructural and surface morphological evolutions of these coatings deposited by p-DC reactive sputtering as a function of pulse frequency are similar to those observed for coatings deposited by p-DC non-reactive sputtering, as discussed in chapter 3 and 4.

It is important to note that the deposition rate of the p-DC sputtered coatings was lower than that observed for DC sputtering and depended on the pulse frequency. As compared to DC sputtering, approximately, 15 and 40% reduction in deposition rate (see Figure 5.19) was observed for p-DC sputtered TiC/a-C:H nanocomposite coatings at 200 and 350 kHz, respectively. The reduction in deposition rate was due to a combination of several factors. The average power dissipated at the target decreases with increasing pulse frequency and at the start of each pulse there is a dead time during which negligible sputtering occurs and the proportion of this dead time increases with increasing pulse frequency and so the deposition rate is lower at higher frequency.[19] The rate of voltage change at the target during the initial stages of the pulse-on period and the maximum negative voltage attained during the pulse-on period is significantly lower at higher frequencies[19]. Since sputtering rate is proportional to power and sputtering yield is proportional to target voltage, both these factors tend to lower deposition rate at higher frequency. The Ar^+ ion and energy flux delivered to the substrate increases with pulse frequency. The higher ion to atom ratio at higher pulse frequencies may reduce the deposition rate by enhanced re-sputtering from the coating. Since the reduction in deposition rate at 200 kHz was low, this was an optimal choice for further studying the influence of process parameters on the mechanical and tribological properties of these coatings.

5.2.2.2 *Effect of substrate bias voltage*

In this section, the effect of negative substrate bias voltage in the range from 40 to 150 V on the tribological, mechanical and structural properties of 200 kHz p-DC sputtered TiC/a-C:H nanocomposite coatings is discussed. The Ti-target current and C_2H_2 flow rate were kept constant at 1 A and 8 sccm, respectively. All these coatings exhibited glassy microstructure (not shown) and hence any possible effects of the columnar features on the properties of the coatings, particularly on friction and wear, were excluded. The Ti-content in these coatings was ~ 17.5 at.% and was not affected by changing the substrate bias voltage (See Table 5.2). The grazing incidence XRD analysis (not shown) confirmed formation of TiC nanocrystallites in these coatings. The average size of the TiC nanocrystallites for the coatings deposited at 40 and 150 V was 2.2 and 2.3 nm, respectively which indicates that the size of TiC nanocrystallites was not affected by the changing substrate bias voltage.

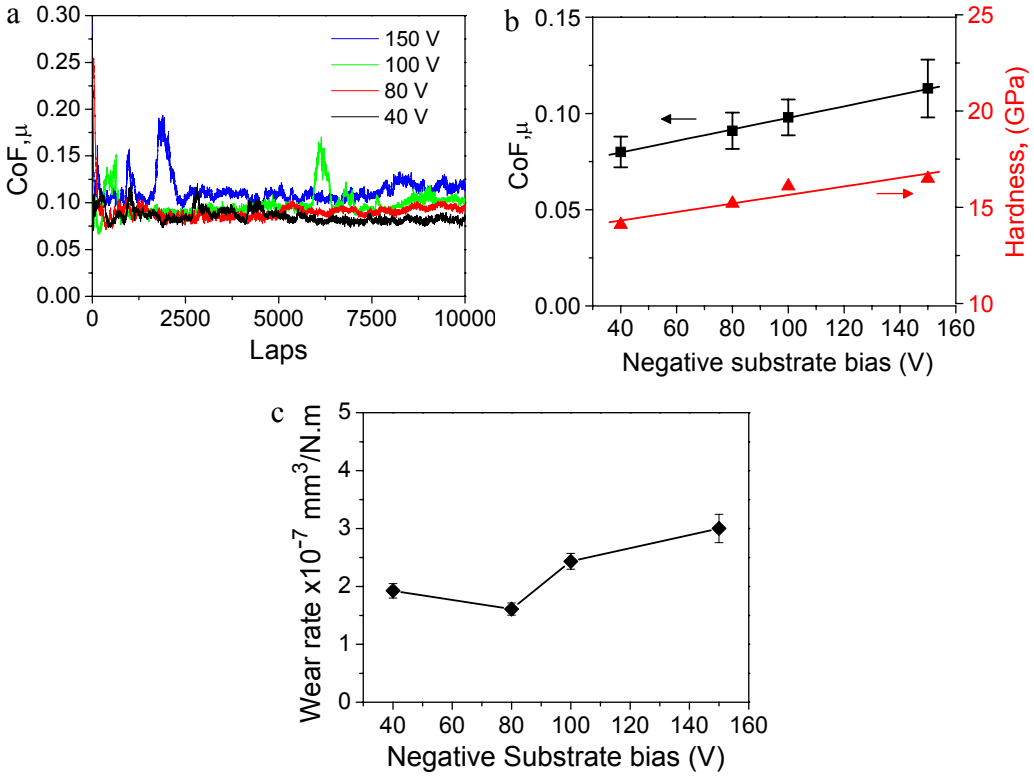

Figure 5.21 (a) Friction characteristics of 200 kHz p-DC sputtered TiC/a-C:H coatings deposited at various negative substrate bias voltage, as indicated, sliding against steel ball at 5 N normal load, sliding velocity 10 cm/s and relative humidity of 50% at 23 °C; (b) CoF (■) and Hardness (▲) and (c) Wear rate of these coatings as a function of negative substrate bias voltage.

Figure 5.21a demonstrates the tribotest results of the four coatings deposited at different bias voltages. All the coatings show a quick drop in the coefficient of friction (CoF) during the initial stages of sliding, which was mainly attributed to the quick

formation of a transfer film on the steel ball which facilitates easy sliding at the interface between the transfer film and the TiC/a-C:H coating. A transfer film was observed on the steel balls after sliding against all these coatings (for e.g. as shown in Figure 5.25c after sliding against the coating deposited at 80 V). The transfer film is mainly composed of amorphous graphite-like carbon. The friction graphs of the coatings deposited at lower bias voltages (40 and 80 V) were steady whereas jumps in CoF values were observed for the coatings deposited at higher bias voltages (100 and 150 V). Figure 5.21b shows the CoF and hardness dependence of TiC/a-C:H nanocomposite coatings as a function of substrate bias voltage. A moderate increase in CoF from 0.08 at 40 V to 0.11 at 150 V was observed. The hardness also showed a moderate increase from 14 GPa at 40 V to 16.5 GPa at 150 V. The wear rates of the coatings as a function of substrate bias voltage are shown in Figure 5.21c. Although the difference in the values was small, the wear rate was higher for coatings deposited at higher substrate bias voltage. Despite the increase in hardness, the wear resistance of the coatings at higher bias values was reduced. Considerable wear debris were observed in and around the wear track after the tribotest on the coatings deposited at higher bias voltages (100 and 150 V). This also reflected in the higher wear rates, in Figure 5.21c, observed for these coatings. Since the presence of wear debris retards the transfer film formation, as discussed in section 6.1, it can be expected that the harder wear debris formed during the sliding against the coatings deposited at higher bias voltages hinder the formation of the transfer film by means of three body abrasion. This also explains the fluctuations in CoF, as seen in Figure 5.21a, observed for these coatings.

Raman analysis was carried out to understand the effect of substrate bias voltage on the chemical structure (sp^3/sp^2) of these coatings. Figure 5.22a and b shows the Raman spectra for the coatings deposited at 80 and 150 V substrate bias voltages. The Raman spectra showed two distinct peaks; the so-called D peak at ~1350 cm^{-1} and the G peak at ~ 1580 cm^{-1}, which correspond to the so called "disordered" and "graphitic" structures respectively. Ferrari and Robertson[20] showed the possibility of acquiring information of the hybridization states of C-C bonding from the analyses of the I(D)/I(G) ratio and the position of the G peak. Provided that the I(D)/I(G) ratio is in the range from 0.2 to 2 and the G peak position ranges from 1510 to 1600, a decrease in I(D)/I(G) ratio and a shift of G peak to lower values indicate a progressive disordering of the sp^2-bonded rings and increase of sp^3 sites in the range from 0 – approximately 20%.[20]

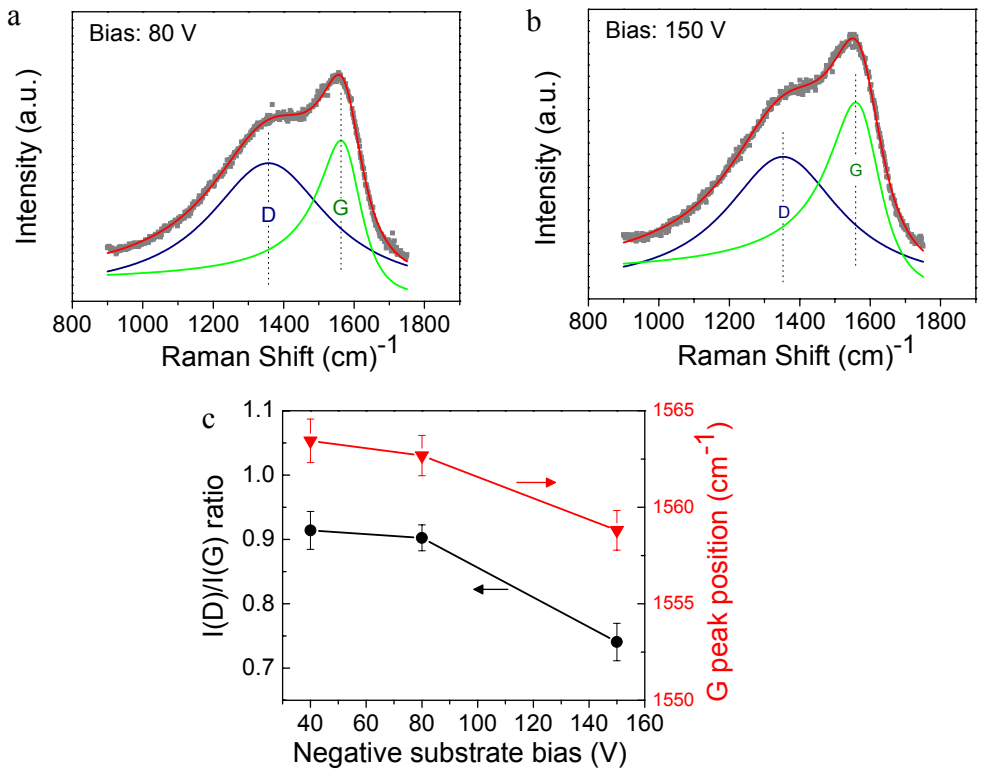

Figure 5.22 BWF-Lorentzian fitted Raman spectra for TiC/a-C:H nanocomposite coatings deposited by 200 kHz p-DC sputtering at negative substrate bias voltage of (a) 80 V and (b) 150V; and (c) I(D)/I(G) ratio (●) and G peak position (▼) as a function of negative substrate bias voltage for these coatings.

Figure 5.22c shows the variation of I(D)/I(G) ratio and G peak position as a function of bias voltage. There was very little difference between the Raman spectra acquired from coatings deposited at 40 and 80 V. However, the I(D)/I(G) ratio decreased and the G peak shifted to the lower wavenumber for the coating deposited at 150 V, indicating an increase in sp^3 content in the coating. The higher sp^3 content leaded to an increase in the hardness at higher substrate bias voltage similar to that observed by Martinez-Martinez et. al.[21] in case of pure amorphous carbon coatings. Also, it is relatively difficult to form a graphite-like transfer film due to relatively lower sp^2 content in the coating and hence yields higher CoF. The increased ion energy delivered to the coating at higher substrate bias voltage may increase the compressive stress in the coatings[22,23] which facilitates the wear debris formation during sliding, as discussed later. Although the hydrogen content in the coatings was not measured, it may decrease with increasing substrate bias voltage[24], and thus contribute to higher CoF.

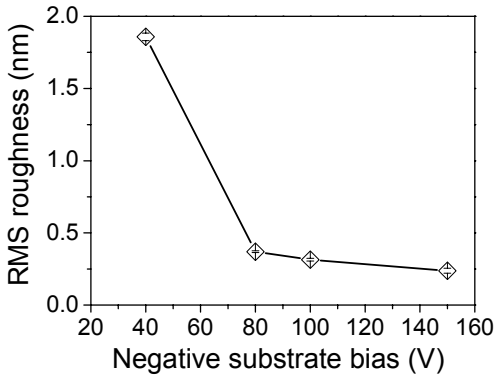

Figure 5.23 Surface roughness of 200 kHz p-DC sputtered TiC/a-C:H coatings as a function of negative substrate bias voltage.

Moreover, a direct correlation between high friction and high roughness was not observed since the surface roughness of the coatings was not high enough. The influence of substrate bias voltage on the surface roughness of these coatings is shown in Figure 5.23. The surface rms roughness rapidly decreased from ~ 1.85 nm at 40 V to about 0.36 nm at 80 V and further reduced to about 0.23 nm at 150 V. The substrate bias voltage of 80 V was considered as optimum which yields smooth surface and also avoids the higher stress in the coating which otherwise deteriorates the tribological performance as that observed for coatings deposited at higher (100 and 150 V) substrate bias voltages.

5.2.2.3 Effect of phase and chemical composition

The composition of these coatings was varied by changing the Ti-target current, and the acetylene flow rate, independently, but keeping the substrate bias voltage and pulse frequency applied to the targets fixed at 80V and 200 kHz, respectively. It was found that at lower target current and higher acetylene flow rate, a complete poisoning of the Ti targets by the carbonous species (formed by decomposition of acetylene gas) occurred. This obstructed the sputtering of Ti from the targets. Since no Ti was detected by EPMA, these coatings were pure a-C:H coatings instead of TiC/a-C:H nanocomposite coatings (c.f. Table 5.2). This gave an opportunity to compare the properties of pure a-C:H (single phase) and TiC/a-C:H (two phases) nanocomposite coatings deposited by 200 kHz p-DC sputtering. Coatings were deposited by varying the Ti target current from 0.6 to 1 A while keeping the substrate bias voltage and C_2H_2 flow rate constant at 80 V and 8 sccm, respectively.

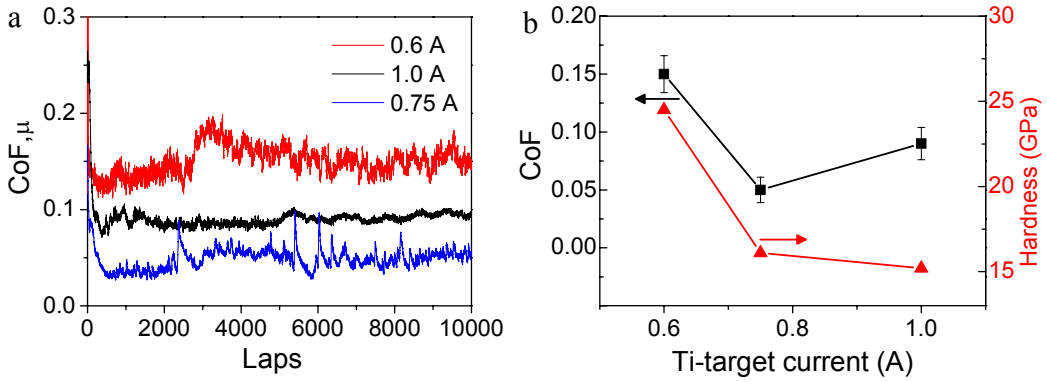

Figure 5.24 (a) Friction characteristics of 200 kHz p-DC sputtered a-C:H (deposited at 0.6 A) and TiC/a-C:H coatings (deposited at 0.75 and 1 A), sliding against steel ball at 5 N normal load, sliding velocity 10 cm/s and relative humidity of 50% at 23 °C; (b) Plot of CoF (■) and Hardness (▲) versus current applied to Ti-target for these coatings.

Figure 5.24a and b shows the frictional characteristics and average CoF, and hardness of the coatings as a function of the current applied to the Ti-targets. The CoF decreases from 0.15 to 0.05 with increasing Ti-target current from 0.6 to 0.75 A and then increases to 0.09 at 1A, as seen in Figure 5.24b. The coating deposited at 0.6 A was a pure a-C:H and the Ti content in the TiC/a-C:H coatings deposited at 0.75 and 1 A was approximately 12.5 and 17.5 at.%, respectively. This indicates that for the given range of Ti content, the TiC/a-C:H nanocomposite coatings exhibit lower CoF than the pure a-C:H coatings for the same load and environment conditions. This was mainly due to reduction in the stress in the coating with addition of Ti and toughening of the coating due to TiC nanocrystallites which reduces its brittleness and hence the wear debris formation. Considerable wear debris was found on and around the wear track of the pure a-C:H coating due to excessive stress in the coating. These hard wear debris cause abrasive wear of the steel ball, which results in a large wear scar of 362 μm in diameter as shown in Figure 5.25a.

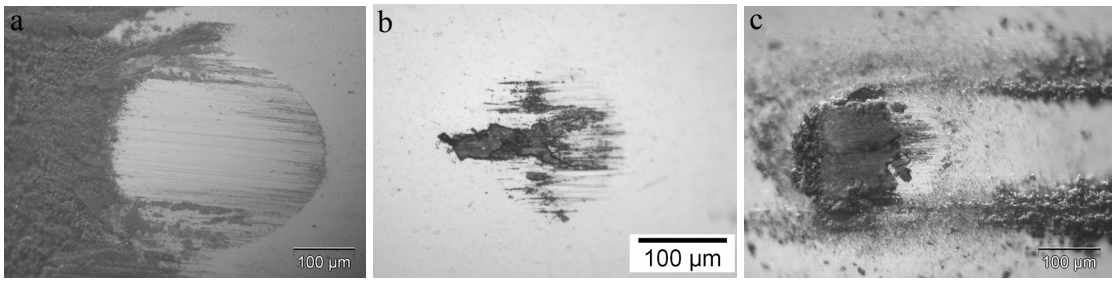

Figure 5.25 Optical micrographs of the wear scar on steel balls sliding against the coatings deposited by 200 kHz p-DC sputtering at a Ti-target current of (a) 0.6A ; (b) 0.75 A and (c) 1 A, respectively. Sliding direction, of the coatings in contact, from left to right. (The area of transfer film is larger in (c) than in (b)).

As discussed in section 5.1, if the contact area on ball counterpart is large then the transfer film can not cover the entire contact area and fails to isolate the steel ball completely and leads to higher CoF. Furthermore, the wear debris hinders the formation of a transfer film. Thus, the transfer film failed to cover the large contact area on the steel ball and yields higher CoF. A relatively little wear of the steel ball occurred against the TiC/a-C:H nanocomposite coatings deposited at a Ti-target current of 0.75 and 1 A. As seen in Figure 5.25b and c, the wear scar diameters on the steel balls were 145 and 175 μm, respectively. The transfer film effectively covered the contact area on the steel balls leading to a lower CoF. The TiC nanocrystallites present at the sliding surface enhance the surface graphitization[8] and promote the formation of transfer film. Since the concentration of the amorphous lubricant phase determines the frictional behavior, with increasing Ti content from 12.1 to 17.5 at.%, the friction increases from 0.05 to 0.08. A 12 at.% content of Ti was considered as the optimum that gives the lowest CoF of 0.05. Many small yet asymmetric peaks were observed in the plot of CoF versus laps for the coating deposited at 0.75 A target current. It was associated with sudden rupture followed by gradual re-formation of the transfer film during sliding. Once the transfer film forms on the steel ball, the CoF can not decrease further and therefore starts to fluctuate. It can be inferred that since the transfer film covered the sliding surface of the ball, the wear rate of the coating diminished. As a result, during further sliding the transfer film is assumed to get thinner until it breaks down, leading to a sudden rise of the CoF. Sliding at a higher CoF leads to wear of the coating which generates the necessary material for the growth of a new transfer film. Thereafter, a new cycle of the dynamic friction process is repeated. A similar frictional behavior of TiC/a-C:H nanocomposite coatings was observed in the previous work in our group.[8] Such a behavior was not seen in the other TiC/a-C:H coating, since a partial break down of the transfer film has a little influence when its area is larger (see Figure 5.25c). The hardness of these TiC/a-C:H coatings was decreased with increasing Ti-target current. This was mainly attributed to decrease in sp^3 content in the coatings, as evidenced by the increase in I(D)/I(G) ratio and shift of the G peak position to higher wave number (see Table 5.2) with increasing Ti-target current.

The effect of changing the C_2H_2 flow rates from 8 to 12 sccm, by keeping all other parameters (Ti-target current at 0.75 A, and substrate bias at 80 V) constant, on the tribological properties of 200 kHz p-DC sputtered coatings was also investigated. The EPMA analysis indicated that the coating deposited at a flow rate of 8 sccm has 12.1 at.% of Ti whereas the coatings deposited at a flow rate of 10 and 12 sccm were pure a-C:H coatings due to complete poisoning of the race tracks on the Ti-targets, as explained earlier. The surface roughness of the coating increased with increasing C_2H_2 flow rate (See Table 5.2). Figure 5.26a shows the frictional characteristics of these coatings.

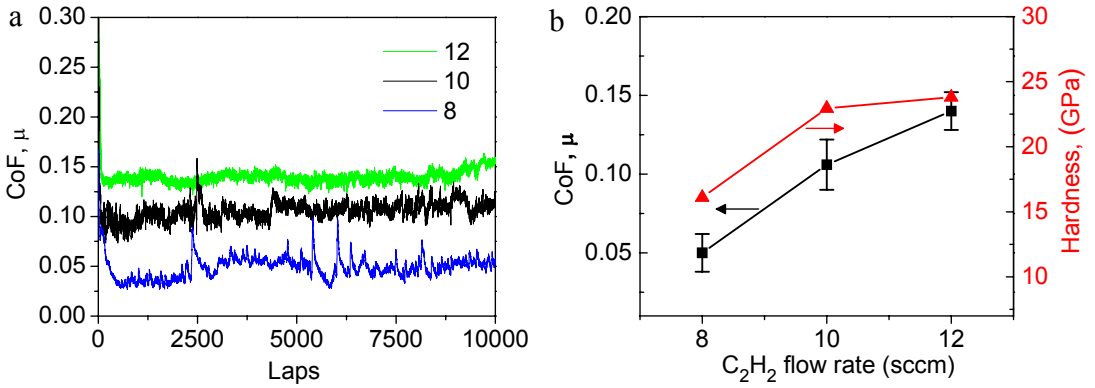

Figure 5.26 (a) Friction characteristics of 200 kHz p-DC sputtered coatings deposited at various flow rates of C_2H_2 in sccm, as indicated, sliding against steel ball at 5 N normal load, sliding velocity 10 cm/s and relative humidity of 50% at 23 °C; (b) CoF (■) and hardness (▲) of these coatings as a function of C_2H_2 flow rate. Note that the coating deposited at 8 sccm was TiC/a-C:H nanocomposite whereas coatings deposited at 10 and 12 sccm were pure a-C:H coatings.

It must be noted that this TiC/a-C:H nanocomposite coating deposited at 8 sccm flow rate was the same coating that gives CoF of 0.05 discussed above. Figure 5.25b and Figure 5.27 show the optical micrographs of the steel balls after sliding against the TiC/a-C:H nanocomposite coating and the pure a-C:H coatings, respectively.

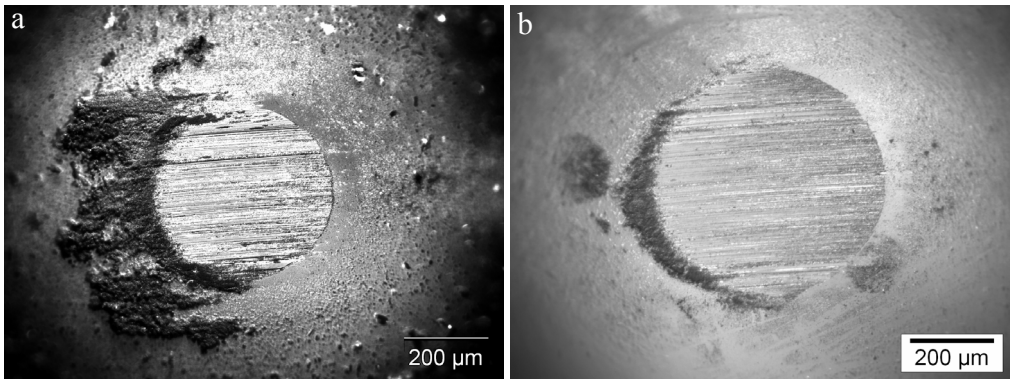

Figure 5.27 Optical micrographs of the wear scar on steel balls sliding against the pure a-C:H coatings deposited by 200 kHz p-DC sputtering at a C_2H_2 flow rate of (a) 10 and (b) 12 sccm, respectively. Sliding direction, of the coatings in contact, from left to right.

A considerable abrasive wear while sliding against the pure a-C:H coatings increased the contact area on the steel ball, which obstructed effective isolation of the steel ball by the transfer film and hence led to higher CoF, as explained before. These observations were consistent with the observations in the previous section where TiC/a-C:H nanocomposite gives lower CoF than the pure a-C:H coatings and can be explained likewise. In the case of the pure a-C:H coatings, a higher CoF was observed at 12 sccm than that compared to 10 sccm. The wear scar diameter in the former case was ~ 558 μm, whereas it was ~ 427 μm in the latter case. The relatively larger contact area on the steel ball was increasingly difficult to be covered by the transfer film in case of the coating

deposited at 12 sccm and hence leads to higher CoF. A large amount of wear debris was observed on and around the wear track on both these coatings after the tribotest. The wear debris also contribute to higher CoF, as discussed earlier. Figure 5.26b shows the CoF and hardness dependence of these coatings as a function of C_2H_2 flow rate. The CoF increases from 0.05 at 8 sccm to 0.14 at 12 sccm. The hardness increased from 16 GPa for the TiC/a-C:H coating deposited at 8 sccm to approximately 23 GPa and remained almost the same for the pure a-C:H coatings deposited at 10 and 12 sccm. Figure 5.28a-c show the Raman spectra of these coatings. There was very little difference between the Raman spectra acquired from the coatings deposited at 10 and 12 sccm. The TiC/a-C:H nanocomposite coating, in Figure 5.28a, showed a pronounced D peak compared to the pure a-C:H coatings, as seen in Figure 5.28b and c. These observations indicate that incorporation of Ti into a-C:H matrix increases the sp^2 content in the coatings.

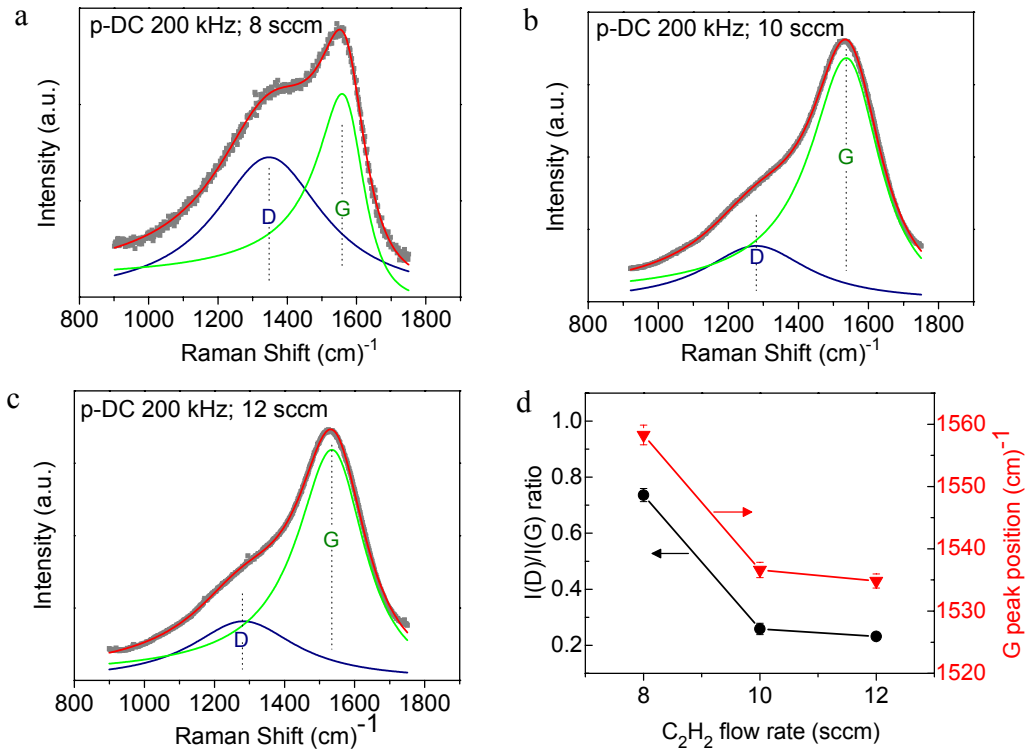

Figure 5.28 BWF-Lorentzian fitted Raman spectra of 200 kHz p-DC sputtered coatings deposited at C_2H_2 flow rate of (a) 8 sccm; (b) 10 sccm and (c) 12 sccm; and (d) I(D)/I(G) ratio (●) and G peak position (▼) as a function of C_2H_2 flow rate for these coatings.

Figure 5.28d shows the variation of I(D)/I(G) ratio and G peak position as a function of C_2H_2 flow rate. The I(D)/I(G) ratio decreased and the G peak shifted to lower wavenumber at higher C_2H_2 flow rate. Both parameters indicate a progressive amorphisation of the sixfold sp^2–bonded rings and increased presence of sp^3 sites in the coatings. The higher hardness of these coatings was correlated to a higher sp^3 content in the coating. The wear rates of the TiC/a-C:H nanocomposite coating and pure a-C:H

coating deposited at 12 sccm were 6.6×10^{-8} and 1.07×10^{-7} mm^3/N m, respectively. The harder (Hardness=23 GPa) a-C:H coatings exhibited poor wear resistance than compared to the softer (Hardness = 16 GPa) TiC/a-C:H nanocomposite coatings.

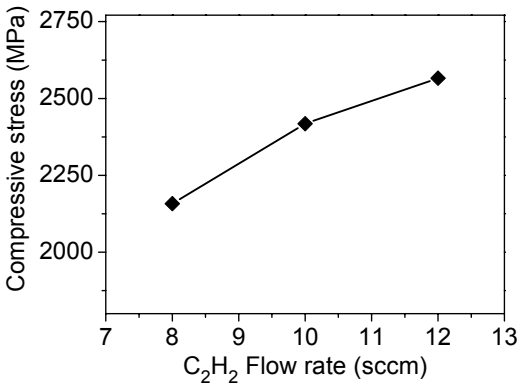

Figure 5.29 Compressive stress as a function of C_2H_2 flow rate for 200 kHz p-DC sputtered coatings. The coating deposited at 8 sccm was TiC/a-C:H nanocomposite whereas coatings deposited at 10 and 12 sccm were pure a-C:H coatings.

In order to understand this phenomenon, the compressive stress in these coatings was measured. Figure 5.29 shows that the compressive stress in these coatings increases with increase in C_2H_2 flow rate. The compressive stress in the TiC/a-C:H nanocomposite coating was less compared to that of pure a-C:H coatings. This was mainly associated with the higher sp^2 content in the TiC/a-C:H nanocomposite coatings since only a small increase in the sp^2 content is needed to account for stress release in these coatings.[25] The increase in the stress in the pure a-C:H coatings with increasing C_2H_2 flow rate was most likely due to increase in thickness[26] from ~ 1.2 μm at 8 sccm to ~ 1.37 μm at 12 sccm. During sliding, the formation of wear debris was promoted due to the presence of high stress in the coating. This also reflects in the high wear rates observed for the a-C:H coatings (see Table 5.2). The hard wear debris are detrimental to the tribological properties of these coatings, as discussed earlier.

5.2.2.4 Effect of pulse frequency

In this section, the effect of pulse frequency (200 and 350 kHz) applied to the Ti-targets on the mechanical, structural and tribological properties of the TiC/a-C:H nanocomposite coatings is discussed. The 200 kHz p-DC sputtered TiC/a-C:H nanocomposite coating deposited at 0.75 A Ti-target current, 80 V substrate bias and 8 sccm of C_2H_2 flow rate was considered optimum since it yielded an ultra-low CoF of 0.05 and a low wear rate of 6.6×10^{-8} $mm^3/N.m$. To understand the effect of pulse frequency, a TiC/a-C:H nanocomposite coating was deposited by p-DC sputtering at 350 kHz pulse frequency and by keeping all the other parameters unchanged. The properties of these two p-DC sputtered coatings at 200 and 350 kHz were compared.

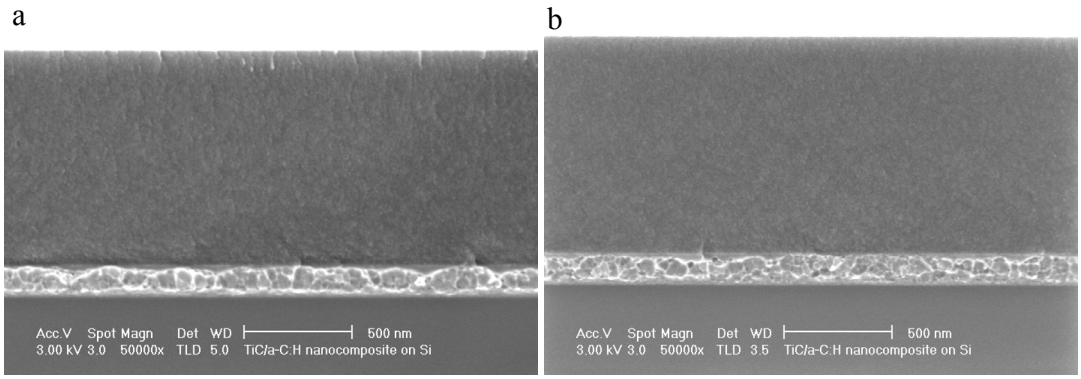

Figure 5.30 Cross sectional SEM of TiC/a-C:H nanocomposite coatings deposited by p-DC sputtering at (a) 200 kHz and (b) 350 kHz pulse frequency.

The cross sectional SEM micrographs shown in Figure 5.30 revealed that both these coatings exhibited dense and column-free microstructure. The EPMA analysis measured a Ti content of 12.5 and 12.2 at.% in the coatings deposited at 200 and 350 kHz, respectively. Although the sputtering of Ti target is less at 350 kHz than at 200 kHz, the chemical composition of these coatings was comparable within the error limits of the measurements. The energy and flux of Ar^+ ions was much higher at 350 kHz than at 200 kHz p-DC sputtering. The intensive Ar^+ ion impingement at the growing coating causes considerable re-sputtering of ad-atoms during deposition. The C atoms were preferentially re-sputtered since they are lighter than the incident Ar ions, whereas Ti atoms being heavier were less likely re-sputtered. During deposition of the 350 kHz p-DC sputtered coating, the sputtering from Ti targets was relatively lower but the re-sputtering of C atom was relatively higher and hence a similar Ti content as that observed for 200 p-DC sputtered coating was observed.

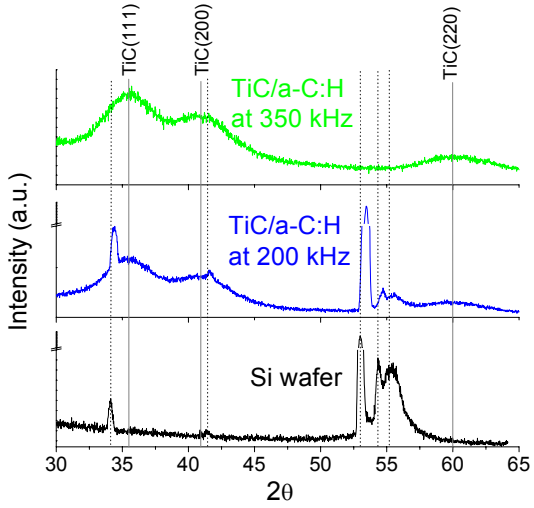

Figure 5.31 Grazing incidence XRD spectra for Si substrate and the TiC/a-C:H nanocomposite coatings deposited at the indicated pulse frequency. Dashed lines indicate the peaks from the Si substrate.

Figure 5.31 shows the grazing incidence XRD spectra which confirmed the presence of TiC nanocrystallites in these coatings. The average size of the TiC nanocrystallites was 1.9 and 1.8 nm for the coatings deposited at 200 and 350 kHz respectively. Several peaks from the Si substrates (dashed lines) were observed in the case of the coating deposited at 200 kHz. Moreover these peaks from the Si substrates were shifted to higher 2θ values due to stress in the coating and is consistent with the observations made by Zhang et al.[23] during deposition of DLC on Si.

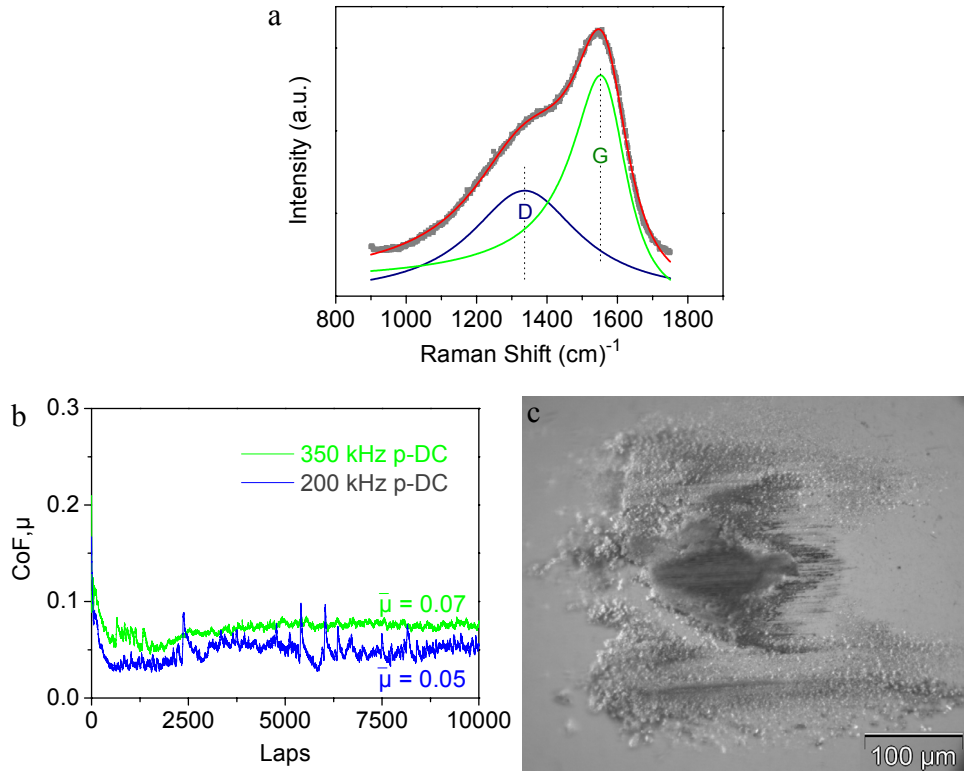

Figure 5.32 (a) Raman spectra; and (b) Frictional characteristics of the 350 kHz p-DC sputtered TiC/a-C:H nanocomposite coating sliding against steel ball (friction graph of 200 kHz p-DC sputtered TiC/a-C:H coating in blue color from Fig 5.24a was included for comparison); (c) Optical micrograph of the steel ball after the tribotest.

Figure 5.32a shows the Raman spectra acquired from the 350 kHz p-DC sputtered TiC/a-C:H nanocomposite coating. This spectra was compared with that of the 200 kHz p-DC sputtered TiC/a-C:H nanocomposite coating which is the same as shown in Figure 5.28a. The I(D)/I(G) ratio decreased from 0.74 to 0.49 and the G peak shifted from 1558.2 to a lower wave number of 1552.0 with increasing pulse frequency from 200 to 350 kHz. Both these observations indicated that the sp^3 content in 350 kHz p-DC sputtered coating was relatively higher than the coating deposited at 200 kHz. The mechanism of the formation of sp^3-C is modeled as "subplantation", where energetic C ions are able to penetrate the surface layer and subsequently bond in a highly stressed tetrahedral (sp^3) configuration[27]. For penetration to occur, the ions should overcome the

C displacement energy (25-35 eV).[27] When the majority of C atoms are not ionized, as is the present case of p-DC magnetron sputtering, it can be inferred that more intensive Ar^+ ion impingement to the growing coating would promote the formation of sp^3-C. During the deposition, some of the individual C atoms in the surface layer would be knocked-down as a consequence of the energy transfer between the incident Ar^+ ions and C atoms. Since the flux and energy of Ar^+ ions in the case of 350 kHz p-DC sputtering is much higher than that at 200 kHz, a higher sp^3 content can be expected. The hardness of the TiC/a-C:H nanocomposite coating deposited at 350 kHz was 17.2 GPa which was higher than that observed for coating deposited at 200 kHz (16.1GPa). It was mainly due to higher sp^3 content in the 350 kHz p-DC sputtered coating. The compressive stress in the coatings was 2.15 and 2.85 GPa at 200 and 350 kHz pulse frequency, respectively.

Figure 5.32b shows the frictional behavior of both the coatings deposited at 200 and 350 kHz. A higher mean CoF of 0.07 was observed for 350 kHz p-DC sputtered coating than that of 0.05 for 200 kHz sputtered coating. Figure 5.32c and Figure 5.25b shows the optical micrographs of the wear scar on the steel balls after sliding against 350 and 200 kHz p-DC sputtered TiC/a-C:H coatings, respectively. In both the cases, a transfer film was formed on the steel ball. The higher CoF for the 350 kHz sputtered coatings can be attributed to relatively lower amount of sp^2 content in the coating. Moreover, considerable wear debris were formed on and around the wear track on this coating and also was collected by the steel ball as seen in Figure 5.32c. Due to high hardness of this coating, comparatively harder wear debris were formed. The hard wear debris retard the formation of the transfer film and contribute to high friction. The higher stress in the coating deposited at 350 kHz promoted the formation of wear debris during sliding. It also reflected in the higher wear rate of 8.2×10^{-8} $mm^3/N.m$ observed for this coating compared to that of 6.6×10^{-8} $mm^3/N.m$ observed for 200 kHz p-DC sputtered TiC/a-C:H coating.

It was noted that despite exhibiting higher residual stress compared to that of the pure a-C:H coatings, the 350 kHz p-DC sputtered TiC/a-C:H nanocomposite coating shows lower CoF and better wear resistance (see Table 5.2). This clearly indicates that incorporation of TiC nanocrystallites into the a-C:H matrix toughens (reduces its brittleness) the coating which reduces the formation of wear debris during sliding and yields lower friction by promoting surface graphitization.

5.3 Conclusion

In conclusion, it was shown that smooth coatings always yield low CoF *independent* of the hardness of counterface materials. However, in the case of rough coatings, the hardness ratio of the ball/coating tribo-pair essentially determines the contact area on the ball counterpart which further influences the transfer film formation and hence CoF. The wear debris also retarded the formation of transfer film. Tribological behavior of TiC/a-C coatings was independent of the columnar microstructure due to excellent toughness of these coatings. The frictional characteristics were controlled to a large extent by the formation of transfer film and its coverage of the contact area. In the case of steel, the hardness ratio was 0.41 and considerable abrasive wear was occurred. The worn ball obstructs the effective transfer film formation and hence yields high CoF. However, for Si_3N_4 ball, the hardness ratio was 0.97 and a little wear of the ball occurred and a "stable" transfer film forms, which yields a low CoF. The rough coating shows better wear resistance than the smooth coating, though of the same hardness. It was shown that the surface roughness evolution of the wear tracks can be correlated to the wear rates of these coatings. Smooth surfaces of the TiC/a-C coatings are favored for obtaining a low CoF independent of the hardness of the counterface materials. Also, hydrogen effectively reduces the adhesive reactions during sliding and hence the smooth TiC/a-C:H coatings exhibit lower friction ($\mu \sim 0.05$) than that of TiC/a-C coatings. Dense, tough, ultra-smooth TiC/a-C:H films exhibiting ultra-low friction and excellent wear resistance can be obtained by pulsed DC sputtering at higher frequencies and at low substrate bias voltage. The tribological properties of TiC/a-C:H nanocomposite films were moderately affected by the change in substrate bias voltage. The change in phase composition strongly influences the tribological performance where the TiC/a-C:H films perform better than the pure a-C:H films. In the case of TiC/a-C:H nanocomposite films, a higher sp^2 content and presence of TiC nanocrystallites at the sliding surface promotes formation of transfer film and yields lower CoF. The Ti content in the film also influences the tribological performance. The optimal Ti content was determined to be ~ 12 at.%. In the case of a-C:H films, a relatively higher sp^3 content and residual stress promote the formation of hard wear debris during sliding, which cause abrasive wear and increases the contact area on the ball counterpart. This makes the formation of transfer film relatively difficult and leads to higher CoF. With increasing pulse frequency, the sp^3 content, hardness and the residual stress in the TiC/a-C:H nanocomposite films increases due to increased intensity of ion impingement to the film. The relatively lower sp^2 content and higher stress in the film deposited at 350 kHz pulse frequency yields inferior tribological properties.

References

1. J. Jiang, R.D. Arnell, Wear 239 (2000) 1.
2. A. Erdemir, C. Donnet, J. Phys. D: Appl. Phys. 39, (2006) R311.
3. A.A. Voevodin, A.W. Phelps, J.S. Zabinski, M.S. Donley, Diamond Relat. Mater. 5, (1996) 1264.
4. A.Erdemir, C. Bindal, G.R. Fenske, C. Zuiker, P. Wilbur, Surf. Coat. Tech. 86, (1996) 692.
5 Voevodin, A. A., O'Neill, J. P., Zabinski, J. S.: Tribological performance and tribochemistry of nanocrystalline WC/amorphous diamond-like carbon composites. Thin Solid Films 342, 194-200 (1999)
6 Nilsson, D., Svahn, F., Wiklund, U., Hogmark, S.: Low-friction carbon-rich carbide coatings deposited by co-sputtering, Wear 254, 1084-1091 (2003)
7. J.C. Sánchez-Lopez, D. Martinez-Martinez , C. Lopez-Cartes, A. Fernandez, Surf. Coat. Technol 202 (2008) 4011.
8. Y.T. Pei, D. Galvan, J.Th.M. De Hosson, Acta Mater., 53 (2005) 4505
9. Y.T. Pei, P. Huizenga, D. Galvan, J.Th.M. De Hosson, J. Appl. Phys. 100 (2006) 114309
10. A. Grill, Surf. Coat. Tech. 94 (1997) 507.
11. F. Svahn, A.K. Rudolphi, E. Wallen, Wear 254 (2003) 1092.
12. H. Liu, A. Tanaka and T. Kumagai, Thin Solid Films 352 (1999) 145.
13. R.S. Sayles, Tribol. Int. 29 (1996) 639.
14. G. W. Stachowiak and A.W. Batchelor, Engineering Tribology, Elsevier science publishers (1993).
15. S. J. Harris, A.M. Weiner Wear 223 (1998) 31.
16. T. Hisakado, Wear 4 (1976) 179.
17. T.W. Scharf and I. L. Singer, Tribol. Lett. 36 (2009) 43.
18. K. Kato, K. Adachi, Modern Tribology Handbook –Vol. 1, Ed.: B. Bhushan (2001).
19. P.J. Kelly, A.A. Onifade, Y. Zhou, G.C.B. Clarke, M. Audronis, J.W. Bradley, Plasma Process. Polym. 4, (2007) 246.
20. A. C. Ferrari and J. Robertson: Phys. Rev. B. 61 (2000) 14095.
21. D. Martínez-Martínez, C. Lopez-Cartes, A. Fernandez, J.C. Sanchez-Lopez, Thin Solid Films 517 (2009) 1662.
22. V. Kulikovsky, P. Bohac, F. Franc, A. Deineka, V. Vorlicek, L. Jastrabik, Diamond and Rel. Mater. 10 (2001) 1076.
23. S Zhang, H. Xie, X. Zeng, P. Hing, Surf. Coat. Technol. 122 (1999) 219.
24. M. A. Tamor, W. C. Vassell, and K. R. Carduner, Appl. Phys. Lett. 58 (1991) 592.
25. A. C. Ferrari, B. Kleinsorge, and N. A. Morrison, J. Appl. Phys. 85 (1999) 7191.
26. D. Sheeja, B.K. Tay, K.W. Leong, C.H. Lee, Diamond Relat. Mater. 11 (2002) 1643.
27. Y. Lifshitz, S.R. Kasi, and J.W. Rabalais, Phys. Rev. Lett. 62 (1989) 1290.

SUMMARY AND OUTLOOK

SUMMARY

Nanocomposite coatings have recently attracted increasing interest due to the possibility of the synthesis of materials with unique properties. Diamond like carbon (DLC) films are of significant interest because of their unique combination of chemical-physical properties, high wear resistance and low friction. Nanocomposite coatings based on dispersion of TiC nanocrystalline phases in solid lubricant phases like amorphous DLC have been shown to enhance the hardness and toughness while maintaining low coefficient of friction. Such films show great potential for exploitation as a protective and lubricant layer to enhance the wear resistance of many tribological applications. For a review reference is made to [1].

In this thesis, the work is focused on utilization of the fact that pulse frequency has prominent effect on the energy distribution and flux of impinging ions at the substrate during p-DC magnetron sputtering. Ion mass/energy spectrometry measurements revealed that the Ar^+ ion and energy fluxes delivered to the coating increased with increasing pulse frequency. The growth dynamics of TiC/DLC nanocomposite coatings were studied with particular emphasis on suppressing the columnar microstructure. Also, evolution in nanostructure from homogeneous to multilayered structure was observed where the modulation of multilayer was controlled by the self-organization of TiC nanocrystallites due to ion impingement for coating deposited at higher pulse frequency. It was shown that by controlling the distribution of TiC nanocrystallites forming nanoscale multilayers, the system can be used as a "microstructural ruler" that was able to distinguish various deformation patterns which can be hardly detected otherwise in a homogenous structure. The influence of the hardness of counterface materials on the tribological performance of TiC/a-C nanocomposite coatings exhibiting various surface roughness was examined. It was observed that hardness ratio of the ball/coating tribo-pair was crucial in determining the influence of roughness on the tribological performance of these coatings. Mechanical, structural, chemical bonding- (sp^3/sp^2) and tribological properties of TiC/a-C:H coatings deposited by pulsed-DC sputtering of Ti-targets in Ar/C_2H_2 plasma were studied as a function of substrate bias voltage, Ti-target current, C_2H_2 flow rate and pulse frequency. Dense, column-free, ultra-smooth and ultra-low

friction TiC/a-C:H films were obtained at lower substrate bias voltage by pulsed-DC sputtering at higher pulse frequency.

Growth dynamics and microstructure of TiC/a-C nanocomposite coatings

Many growth effects are operating during the growth of a coating and contribute to the surface roughness evolution. During sputtering deposition there is an interplay between interface roughening generated by noise, smoothing driven by surface diffusion due to concurrent ion impingement and nonlocal effects generated by shadowing. Dynamic roughening is commonly observed during film deposition where surface roughness increases with deposition time. Breakdown of dynamic roughening during the growth of TiC/a-C nanocomposite coatings was observed. With increasing energy flux of concurrent ion impingement during pulsed DC sputtering, a transition from dynamic roughening to dynamic smoothing was observed in the growth behavior of TiC/a-C nanocomposite coatings. During 350 kHz p-DC sputtering, a negative growth exponent and ultra-smoothness (RMS roughness ~0.2 nm at film thickness of 1.5 μm) was observed. From detailed analyses of surface morphology and growth conditions it is concluded that a transition in growth mechanisms occurs, i.e. a mechanism dominated by geometric shadowing at lower (100 kHz) pulse frequency evolving to a surface diffusion mechanism driven by ion impact-induced atomistic downhill flow process at higher (350 kHz) pulse frequency, which leads to the transition from a strong columnar to a columnar-free microstructure. The growth mechanisms essentially determine the growth front roughness evolution and hence the microstructure of the coatings. Moreover, it is shown that rapid smoothing of initially rough surfaces with RMS roughness ~ 6 nm to < 1 nm can be effectively achieved with p-DC sputtering at 350 kHz pulse frequency. In order to analyze the smoothing mechanism the roughness evolution is described by a model; a linear stochastic differential equation with the second- and fourth-order gradient relaxation terms, which account for diffusion along the coating surface. Furthermore, the nonlocal shadowing effects in three spatial dimensions along with the angular distribution of depositing particles were included to explain the steep increase of roughness in DC or low frequency p-DC sputtering. The model is in good agreement with atomic force microscopy measurements of roughness evolutions.

Nanostructure and deformation behavior of TiC/a-C nanocomposite coatings

Controlled growth of self-assembled nanocomposite multilayers has been achieved via turning the intensity of concurrent ion impingement by changing the frequency of p-DC sputtering. Nanoscale structural and chemical information, especially at the growing front, have been obtained with high spatial resolution structure investigations. It was found that concurrent ion impingement of growing films produces an amorphous capping

layer of ~3 nm thicknesses where spatially modulated phase separation is initiated. The modulation of multilayers, controlled by the self-organization of nanocrystallites below the capping layer, was maintained through the entire film. As a result, the fluctuation of the multilayered structures was stable and occurred at a length scale smaller than one bilayer thickness. Combined nanoindentation and ex situ cross-sectional transmission electron microscopy (XTEM) investigations were carried out on TiC/a-C nanocomposite coatings, with and without multilayered structures, deposited by pulsed DC magnetron sputtering. By controlling the distribution of TiC nanocrystallites forming nanoscale multilayers, the system can be used as a "microstructural ruler" that was able to distinguish various deformation patterns which can be hardly detected otherwise in a homogenous structure. The results confirm supertough properties while maintaining high hardness. Extensive interparticle deformation processes involving rearrangement of nanocrystallites and displacement of a-C matrix occurring at length scales from tens of nanometer down to 1 nm were clearly revealed with XTEM. At submicrometer scale this interparticle process prompts multiple shear bands nucleating homogeneously within the nanocomposites and contributes to toughening effects. At large indentation depths, the multilayered nanocomposite top layer significantly delocalizes abrupt shear deformation arising from the interlayer. In the thin film without a multilayered structure nanocrystallites were found to deflect cracks effectively.

Effect of surface roughness on tribological behavior of TiC/a-C nanocomposite coatings

In general, it is believed that a high surface roughness yields major frictional and wear losses mainly during the running-in period. However, it may also influence the overall frictional behavior of DLC based coatings. Moreover, the hardness of the mating materials also influences their tribological properties. The low friction of DLC based coatings has been mainly attributed to the formation of a transfer film on the sliding surface of the counterface materials. It is important to understand the influence of roughness on the formation of the transfer film and CoF of these coatings sliding against different counterface materials in order to underpin their tribological properties. Effect of hardness and surface roughness on the frictional and wear behavior of TiC/a-C nanocomposite coatings sliding against steel and Si_3N_4 ball counterparts was studied. The smooth coatings always yield a low CoF (~ 0.09) *independent* of the hardness of the counterface materials. However, in the case of rough coatings, the hardness ratio of the ball/coating tribo-pair essentially determines the contact area which further influences the formation of the transfer film and hence CoF. The friction characteristics were controlled to a large extent by the transfer film and its coverage on the wear scar. In the case of steel, the hardness ratio was 0.4, and considerable abrasive wear occurred. The worn ball

obstructed the effective transfer film formation and hence yielded a high CoF. However, for Si_3N_4 ball, the hardness ratio was 0.94, and a little wear of the ball occurred and a "stable" transfer film formed, yielding a low CoF. It was shown that the surface roughness evolution of the wear tracks can be correlated to the wear rates of these coatings. Smooth TiC/a-C coatings are favored for obtaining a low CoF independent of the hardness of the counterface materials.

Effect of process parameters on tribological and mechanical properties of TiC/a-C:H nanocomposite coatings

Apart from the adverse effect of surface roughness, one has to reduce the covalent bond interactions between unoccupied or dangling σ-bonds of sliding interfaces of DLC based coatings, which lead to significant source of adhesion and contribute to high friction. It is known that hydrogen effectively passivates these unoccupied bonds and lead to low friction. So efforts were made to obtain ultra low friction ($\mu < 0.1$) TiC/a-C:H nanocomposite coatings. Mechanical, structural, chemical bonding- (sp^3/sp^2) and tribological properties of reactively sputtered TiC/a-C:H nanocomposite coatings were studied as a function of substrate bias voltage, Ti-target current, C_2H_2 flow rate and pulse frequency by nanoindentation, Raman spectroscopy and ball-on-disc tribometry. Dense, column-free and smooth TiC/a-C:H films can be obtained at substrate bias voltage of 40 V by p-DC sputtering at 200 and 350 kHz frequency. The tribological properties of TiC/a-C:H nanocomposite films were moderately affected by the change in substrate bias voltage. The change in phase composition strongly influences the tribological performance where the TiC/a-C:H films perform better than the pure a-C:H films. In the case of TiC/a-C:H nanocomposite films, a higher sp^2 content and presence of TiC nanocrystallites at the sliding surface promotes the formation of transfer layer and yields lower CoF (~ 0.05). The optimal Ti content was determined to be ~ 12 at.%. In the case of a-C:H films, a relatively higher sp^3 content and residual stress promote the formation of hard wear debris during sliding, which cause abrasive wear and increases the contact area on the ball counterpart. This makes the formation of transfer layer relatively difficult and leads to higher CoF. With increasing pulse frequency, the sp^3 content, hardness and the residual stress in the TiC/a-C:H nanocomposite films increases due to increased intensity of ion impingement to the film.

OUTLOOK

For achieving a high degree of chemical inertness on sliding DLC surfaces, in order to obtain ultra-low friction, a hydrogen-rich gas discharge plasma during coating deposition is used during coating deposition. The main purpose is to eliminate those dangling σ-bonds by reaction with hydrogen. Indeed dangling bonds can cause very

strong covalent bond interactions and, hence, high friction during sliding. Because of its small size in the atomic and protonic forms, large amounts of hydrogen (up to 50 at. %) can be incorporated into DLC films. For the production of hydrogen-rich DLC films, H_2 gas is blended with hydrocarbons as CH_4 and C_2H_2 and released into the deposition chamber. A high degree of hydrogenation of DLC films appears to play a pivotal role in friction and wear. In general, the higher the H/C ratio in the gas discharge plasma, the lower the friction coefficients.[2] The H/C ratio is 4 for pure methane source gas which yields a DLC film exhibiting lower CoF than the film derived from C_2H_2 (whose H/C ratio is 1) under the same sliding conditions, whereas the CoF for ethylene with an H/C = 2 is between that of methane and acetylene. The lowest friction is achieved in the plasma that contains H/C = 10 (obtained by a gas composition of 75% H_2 and 25% CH_4). An extra hydrogen during DLC deposition lead to increased hydrogen concentration within the bulk, as well as on the surface. Most of these hydrogen atoms are paired with σ-bonds, but some unbonded free hydrogen may also exist as interstitials. In addition to bonded hydrogen, considerable amounts of unbonded or free hydrogens may exist in atomic and molecular forms. High hydrogen concentration within the DLC films and on the surface should effectively diminish or even eliminate the possibility of unoccupied σ-bonds remaining and participating in any strong adhesive interactions during sliding. Free hydrogen within the films may serve as a reservoir and can replenish or replace those hydrogen atoms that may have been lost due to thermal heating and/or mechanical action during sliding.[2] Thus, to obtain ultra-low friction, it will be interesting to use hydrocarbon gases of different H/C ratios and/or mixed with hydrogen gas so as to obtain different content of total hydrogen and unbonded hydrogen in TiC/a-C:H nanocomposite coatings.

The CoF of a-C:H based coatings increases rapidly with increasing humidity.[3] Adsorbed gases, especially water vapor, increases the rate of densification of the particulate materials and therefore denser transfer films are formed at higher humidity which in turn increases CoF.[3] Also, their strong dependence of CoF on humidity has been attributed to viscous and capillary forces induced by adsorbed water.[4] Tagawa et al. observed a direct link between water coverage on a hydrogenated carbon surface and friction coefficient. The friction coefficient increased markedly when the surface water coverage exceeded about one monolayer.[5] Therefore, reduction in the surface water coverage under humid conditions may allow these films to retain their low friction properties as that in dry air. Freyman et al. has reported synthesis and tribological performance of sulfur doped hydrogenated carbon films.[6] They have shown that 5 at.% sulfur incorporation in the hydrogenated carbon increases hydrophobicity of these films and hence reduces humidity sensitivity of the friction. Reduction of adsorbed water molecules by sulfur doping may be the primary cause of the improved friction performance at higher humidity. Thus, it is interesting to synthesize sulfur doped TiC/a-

C:H nanocomposite films in order to suppress the effect of humidity on their tribological properties.

For high temperature applications (e.g. in high speed machining) thermal stability and oxidation resistance of DLC is a concern. It has been reported that DLC is structurally stable up to 300 °C.[7] Beyond that temperature, graphitization occurs leading to drastic reduction in hardness. Above 500 °C, DLC is oxidized and loss of coating thickness occurs.[8] However Zheng et.al. reported that Al addition to TiC/a-C increases the oxidation resistance, and the coating thickness remains unchanged up to 600°C. However tribological properties of these coatings have not been studied. Recently Nilsson et. al. reported that incorporating 6 at% Al to TaC/a-C (where Ta is 15 at%) reduces the friction coefficient (Load=5N,against 100Cr6 ball and at room temp) to 0.05[9] but the mechanism has not been completely understood yet. With Al addition, the residual compressive stress in the coatings is also reduced.[8,9] The elevated temperature tribotests of Me-DLC with Al addition has not been reported so far. Thus, Al addition to the TiC/a-C and TiC/a-C:H coatings can yield improved oxidation resistance and better high temperature performance and it is interesting to understand the tribological performance of these coatings.

References

1 A. Cavaleiro and J.T.M De Hosson, Nanostructured Coatings. New York: Springer-Verlag; 2006.

2. A. Erdemir, C. Donnet, J. Phys. D: Appl. Phys. 39, (2006) R311.

3 J.T.M. De Hosson, Y. Pei, C.Q. Chen, JoM (2007) 45.

4 J. Andersson, R.A. Erck, A. Erdemir, Surf. Coat. Technol.,163 (2003) 535.

5 M. Tagawa, M. Ikemura, Y. Nakayama, N. Ohmae, Tribol. Lett. 17 (2004) 575.

6 C. A. Freyman, Y. Chen, Y. Chung, Surf. & Coat. Tech. 201 (2006) 164.

7 B.K. Tay, D. Sheeja, S.P. Lau, X. shi, B.C. Seet, Y.C. Yeo, Surf. Coat. Tech. 130 (2000) 248.

8 S. Zhang, X.L. Bui, X. Li, Diamond relat. mater. 15 (2006) 972.

9 D. Nilsson, N. Stavlid, M. Lindquist, U. Wiklund and S. Hogmark, Surf. Coat. Technol. 203 (2009) 2989.

LIST OF PUBLICATIONS

1. "Influence of surface roughness on the transfer film formation and frictional behavior of TiC/a-C nanocomposite coatings".
   K.P. Shaha, Y.T. Pei, D. Martinez-Martinez, J.Th.M. De Hosson. Tribol. Lett., 40 (2010), in press, doi:10.1007/s11249-010-9691-4.
2. "Influence of hardness and roughness on the tribological performance of TiC/a-C nanocomposite coatings".
   K.P. Shaha, Y.T. Pei, D. Martinez-Martinez, J.Th.M. De Hosson. Surf. Coat. Technol., (2010), in press, doi: 10.1016/j.surfcoat.2010.10.021.
3. "Effect of process parameters on mechanical and tribological performance of pulsed-DC sputtered TiC/a-C: H nanocomposite films".
   K.P. Shaha, Y.T. Pei, D. Martinez-Martinez , J.C. Sanchez-Lopez, J.Th.M. De Hosson. Surf. Coat. Technol., (2010), in press, doi: 10.1016/j.surfcoat.2010.10.020.
4. "Pulsed-DC sputtered DLC based nanocomposite films: Controlling growth dynamics, microstructure and frictional properties."
   K.P. Shaha, Y.T. Pei, C.Q. Chen, J.Th.M. De Hosson. Mater. Technol., (2010) accepted.
5. "Synthesis of ultra-smooth and ultra-low friction DLC based nanocomposite films on rough substrates".
   K.P. Shaha, Y.T. Pei, C.Q. Chen, J.Th.M. De Hosson Thin Solid Films, (2010), in press, doi:10.1016/j.tsf.2010.08.094.
6. "On the dynamic roughening transition in nanocomposite film growth".
   K.P. Shaha, Y.T. Pei, C.Q. Chen, A.A. Turkin, D.I. Vainshtein, J.Th.M. De Hosson. Appl. Phys. Lett. 95 (2009) 223102.
7. "Growth of nanocomposite films: From dynamic roughening to dynamic smoothening."
   Y.T. Pei, **K.P. Shaha**, C.Q. Chen, R. van der Hulst, A.A. Turkin, D.I. Vainshtein, J.Th.M. De Hosson. Acta Mater., 57 (2009) 5156.
8. "On the evolution of film roughness during magnetron sputtering deposition".
   A.A. Turkin, Y.T. Pei, **K.P. Shaha**, C.Q. Chen, D.I. Vainshtein, J.Th.M. De Hosson. J. Appl. Phys., 108 (2010) 1.
9. "Surface roughness evolution of nanocomposite thin films".
   A.A. Turkin, Y.T. Pei, **K.P. Shaha**, C.Q. Chen, D.I. Vainshtein, J.Th.M. De Hosson. J. Appl. Phys., 105 (2009) 013523.

10. “Tunable self-organization of nanocomposite multilayers”.
    C.Q. Chen, Y.T. Pei, **K.P. Shaha**, J.Th.M. De Hosson. Appl. Phys. Lett., 96 (2010) 073103.
11. “Nanoscale deformation mechanism of TiC/a-C nanocomposite coatings”.
    C.Q. Chen, Y.T. Pei, **K.P. Shaha**, J.Th.M. De Hosson. J. Appl. Phys., 105 (2009) 114314.
12. “Nanoscale deformation in TiC/a-C multilayered nanocomposite coatings”.
    C.Q. Chen, Y.T. Pei, **K.P. Shaha**, J.Th.M. De Hosson. Appl. Phys. Lett., 92 (2008) 241913.
13. “Microstructural control of TiC/a-C nanocomposite coatings with pulsed magnetron sputtering”
    Y.T. Pei, C.Q. Chen, **K.P. Shaha**, J.Th.M. De Hosson, J.W. Bradley, S.A. Voronin, M. Cada. Acta Mater. 56 (2008) 696.
14. “Dynamic smoothing of nanocomposite films”.
    Y.T. Pei, A.A. Turkin, C.Q. Chen, **K.P. Shaha**, D.I. Vainshtein, J.Th.M. De Hosson. Appl. Phys. Lett., 96 (2010) 151910.

Conference presentations

1. “Synthesis of ultra-smooth and ultra-low friction DLC based nanocomposite films on rough substrates”.
   K.P. Shaha, Y.T. Pei, C.Q. Chen, J.Th.M. De Hosson. 37th International Conference on Metallurgical Coatings and Thin Films, ICMCTF 2010, April 26-30, 2010, San Diego, CA, USA.
2. “Evolution of dynamic growth behavior and microstructure of pulsed-DC sputtered DLC based nanocomposite films”.
   K.P. Shaha, Y.T. Pei, C.Q. Chen, J.Th.M. De Hosson. International Symposium on Reactive Sputter Deposition RSD2009, 10-11 December 2009, Manchester, UK.
3. “Dynamic smoothening and tribological properties of pulsed-DC sputtered DLC based nanocomposite films”.
   K.P. Shaha, Y.T. Pei, C.Q. Chen, J.Th.M. De Hosson. (Invited talk) Ninth International Conference on Surface effects and Contact Mechanics Computational methods and Experiments, Contact and surface 2009, 9-11 June 2009, Algarve, Portugal.
4. “Effect of pulse frequency on dynamic growth behavior and properties of Ti-DLC nanocomposite films”.
   K.P. Shaha, Y.T. Pei, C.Q. Chen, J.Th.M. De Hosson. Annual conference of Materials innovation institute (M2i) on Materials to innovate the industry, Dec 8-9, 2008, Noordwijkerhout, The Netherlands.

5. “Optical emission spectrometry and characterization of pulsed-DC reactively sputtered TiC/a-C:H nanocomposite films”.
   K.P. Shaha, Y.T. Pei, C.Q. Chen, J.Th.M. De Hosson. 14th International Conference on Thin Films & Reactive Sputter Deposition 2008 (ICTF14 & RSD 2008), Nov. 17-20, 2008 Gent, Belgium.
6. “Growth Behavior of Magnetron Sputtered Nanocomposite Films: Experimental Observation and Simulation”.
   Y.T. Pei, **K.P. Shaha**, C.Q. Chen, A.A. Turkin, D.I. Vainshtein, J.Th.M. De Hosson. 37th International Conference on Metallurgical Coatings and Thin Films, ICMCTF 2010, April 26-30, 2010, San Diego, CA, USA.
7. “From dynamic roughening to dynamic smoothening: the growth behavior of nanocomposite films controlled by concurrent ion impingement”.
   Y.T. Pei, **K.P. Shaha**, C.Q. Chen, R. van der Hulst, A.A. Turkin, J.Th.M. De Hosson. 14th International Conference on Thin Films & Reactive Sputter Deposition 2008 (ICTF14 & RSD 2008), Nov. 17-20, 2008 Gent, Belgium.
8. “Microstructural evolution of TiC/a-C nanocomposite coatings with pulsed magnetron sputtering”.
   Y.T. Pei, **K.P. Shaha**, C.Q. Chen, J.Th.M. De Hosson, J. W. Bradley, S. Voronin, M. Cada. (Invited talk) Eighth International Conference on Computer Methods and Experimental Measurements for Surface and Contact Mechanics, Contact and Surface 2007, May 16-28, 2007, The New Forest, UK.
9. “Pulsed magnetron sputtering and microstructural evolution of TiC/a-C nanocomposite coatings”.
   Y.T. Pei, **K.P. Shaha**, R. van der Hulst, J.Th.M. De Hosson, S. Voronin, M. Cada, J. W. Bradley. Symposium on Reactive Sputter Deposition, Nov. 30- Dec. 1, 2006, Gent, Belgium.
10. “From Dynamic Roughening To Dynamic Smoothening: Controlled Growth And Properties Of Nanocomposite Films”.
    J.Th.M. De Hosson, Y.T. Pei, **K.P. Shaha**, C.Q. Chen, D. I. Vainshtein, A. A. Turkin. International Conference on Processing & Manufacturing of Advanced Materials: Processing, Fabrication, Properties, Applications, August 25-29, 2009, Berlin, Germany.
11. “An integrated XTEM and nanoindentation investigation on a nanocomposite coating with a designed multilayer substructure”.
    C. Q. Chen, Y. T. Pei, **K.P. Shaha**, J.Th. M. De Hosson. 8th European Symposium on Nanomechanical Testing, NanoMech 2007, Sept. 3-5, 2007, Hüchelhoven, Germany.

12. “Deformation mechanism in a multilayered TiC/a-C nanocomposite coatings”.
    C.Q. Chen, Y.T. Pei, **K.P. Shaha**, J.Th.M. De Hosson. 2nd International Conference on Heterogeneous Materials Mechanics, ICHMM 2008, June 3-8, 2008 Huangshan, China.
13. “DLC-based nanocomposite coatings: from design of nanostructure to advanced mechanical and tribological performances”.
    Y.T. Pei, C.Q. Chen, **K.P. Shaha**, J.Th.M. De Hosson. 2nd International Conference on Nanoscience and Technology, China, ChinaNano 2007, June 4-6, 2007, Beijing, China.
14. “Tunable self-organization of nanocomposite multilayers”.
    J.Th.M. De Hosson, Y.T. Pei, C.Q. Chen, **K.P. Shaha**, D.I. Vainshtein, X International Conference on “Nanostructured Materials”, NANO 2010, September 13-17, 2010, Rome, Italy.
15. “From dynamic roughening to dynamic smoothing: the growth behavior of nanocomposite films controlled by concurrent ion impingement”.
    Y. T. Pei, D. Vainshtein, C.Q. Chen, **K. P. Shaha**, A.A. Turkin, J.Th.M De Hosson, 18th international conference vacuum congress, IVC-18, August 23-27, 2010, Beijing, China.

ACKNOWLEDGEMENTS

The last lines of this text should be words of gratitude to all those kind people around me who helped me directly or indirectly to make this thesis possible.

Foremost, I would like to express my deep and sincere gratitude to my thesis supervisor Prof. Jeff De Hosson for giving me the opportunity to carry out this research. Your perpetual support, motivation, enthusiasm, and immense knowledge helped me all the time during this research. I am grateful to you for all the scientific discussions of the results and analysis, and also for supporting me to attend various international conferences for presenting the results. Thank you for everything Jeff, I really enjoyed a lot working with you and without your support this thesis would not have been possible. Also, many thanks are due to the M2i project leader and my co-promoter Dr. Pei for all your guidance and for explaining me to work with the deposition system, and for the training to get excellent microscopy images.

I sincerely thank Dr. Changqiang Chen for your excellent contribution in TEM results and analysis. I am thankful to Dr. Anatoly Turkin for your splendid contribution in simulation. I am thankful to you for all the enthusiastic discussions. My special thanks go to Dr. Diego Martinez-Martinez for supporting me in number of ways. I am grateful to you for the valuable discussions and suggestions. I was fascinated by your data analysis skills, problem solving approach and your willingness to share your knowledge without any expectations in return. I have learned a lot from you. Interacting with you has always been an inspiring and joyous time. I am thankful to you for always finding time for my random queries. I am really lucky to have worked with you.

Members of my reading committee, Prof. A. Cavaleiro, Prof. P. Rudolf, Prof. H. A. De Raedt – thank you all for your careful reading and for your valuable comments and suggestions.

I am thankful to my paranymphs, Enne Faber and Ismail Hemmati, for your great help and support. My roommates - Diego, Enne (who are my good friends now) thank you for the positive working environment, enjoyable discussions and pleasant time we spent together.

Prof. Albano Cavaleiro from the Mechanical Engineering department of the University of Coimbra (PT), is thanked for the EPMA measurements. Prof. Juan Carlos Sanchez-Lopez from Instituto de Ciencia de Materiales de Sevilla, Spain is thanked for the Raman measurements. I thank Prof. Petra Rudolf for giving access to the Picole AFM. I thank Dr. Christian Strondl, Dr. Roel Tietema from Hauzer Techno coating and Dr. XiaoBo Zhou from SKF - the contact persons of the industrial partners of my project.

Dr. David Vainchtein, thank you so much for the technical assistance during troubleshooting of deposition set-up and other equipment. Having you in our research group, we never worried about the problems related to equipment. Dr. Vasek Ocelik, special thanks for your assistance in microscopy related, computer related and other technical help. I had a great time with you during our visit to Portugal for a conference. I am also thankful to both David and Vasek for their support as our responsible curators of the impressive state-of-the-art MK facilities. I am thankful to Dr. Willem-Pier Vellinga, Dr. Ramanathaswamy Pandian for sharing your AFM experience with me and also for the friendly talks. I am thankful to Dr. Paul Bronsveld for always being enthusiastic about our results and for all the Dutch to English translations. I wish to thank Jacob Bass for his cooperation in XRD measurements. I thank Elly Eekhof for her support and handling the administrative burden.

I thank all the other colleagues with whom I spent time during the last four years, in particular Alexander Fedorov, Emiel Amsterdam, Dave Matthews, Damiano Galvan, Tony Kazantzis, Alexander Kilimovitskiy, Zhenguo Chen, Eric Detsi, Gopi Krishnan, Peter van Zwol, Alessio Morelli, Sriram Venkatesan, Bui Xuan Lam, Jasper Oosthoek, Alex Do Nascimento, Uazir de Oliveira, Mikhail Dutka, Oleksii Kuzmin, Sergey Punzhin, Willem van Dorp, Ivan Furár, Jozef Vincenc Obona, Jiancun Rao, Huajie Yang.

I would also like to thank Dr. Derk Bol, people from HR and financial departments of Materials innovation institute (M2i) for their support and making life easy here. I truly enjoyed the M2i sportsday events.

Last but not the least, I would like to thank Bha (my grandfather) for the inspiration to always excel in whatever I do and for your religious thoughts which are continuous source of peace and energy, which helped me dealing with tough situations during these years. I am grateful to Mamma and Pappa for your never ending love, encouragement and morale support. Thank you for your rock solid support during these years. I will treasure the gratifying and wonderful time that we spent together here in Groningen. The encouragement and support from my beloved wife Payal and my joyful son Arghya is a powerful source of inspiration and energy. Thanks a lot Payal for all your patience. I also thank my brother – Yateen, other family members, Prof. Tatyasaheb Ghatge (my school teacher) and my friends for their kind support.

There are some supporting people that I might have forgotten: exhaustion plays havoc on memory. My humblest apologies to those who consider themselves having earned for being cited amongst these lines.

Kalpak
Groningen
November 2010